

Persistent photo-induced effects in
high-temperature superconducting
 $R\text{Ba}_2\text{Cu}_3\text{O}_{7-\delta}$

vorgelegt von
Diplom-Physikerin
Sabine Bahrs
aus Berlin

von der Fakultät II – Mathematik und Naturwissenschaften
der Technischen Universität Berlin
zur Erlangung des akademischen Grades

Doktor der Naturwissenschaften
– Dr. rer. nat. –

genehmigte Dissertation

Promotionsausschuss:

Vorsitzender: Prof. Dr. Andreas Knorr
Berichter: Prof. Dr. Christian Thomsen
Berichter: Priv. Doz. Dr. Alejandro R. Goñi

Tag der wissenschaftlichen Aussprache: 25. November 2005

Berlin 2006
D83

Zusammenfassung

In dieser Arbeit werden beständige, photoinduzierte Effekte in den Hochtemperatursupraleitern der $R\text{Ba}_2\text{Cu}_3\text{O}_{7-\delta}$ Materialklasse untersucht (R : Y oder seltene Erde außer Pm, Ce, Tb). Die Effekte findet man ausschließlich in sauerstoffreduzierten Varianten dieser Verbindungen, mit den darin typischen, unvollständigen Cu-O Ketten. Eine der Beobachtungen ist ein langsamer, photoinduzierter Anstieg der Leitfähigkeit und der Sprungtemperatur auf einer Zeitskala von mehreren Stunden. Beleuchtet man bei Temperaturen unterhalb von ca. 250 K, bleibt der erreichte Zustand nach Ende der Beleuchtung stabil, während schon bei Zimmertemperatur thermisch angeregte Relaxation eintritt. Diese ungewöhnliche Eigenschaft bietet eine interessante Alternative zu den gängigen Methoden der Dotierungsmanipulation in den Kupraten, ist aber hinsichtlich ihres Mechanismus noch nicht vollständig verstanden. Ein Effekt mit ganz ähnlichen Eigenschaften ist aus der Ramanspektroskopie bekannt: Durch Sauerstoffdefekte aktivierte Moden verlieren unter Beleuchtung Intensität.

Die Auswirkungen der Beleuchtung erinnern stark an die bereits bekannte Sauerstoffumordnung, bei der die Fehlstellen in den Cu-O Ketten selbst regelmäßige Anordnungen bilden. Unter anderem setzt die Relaxation nach Beleuchtung im gleichen Temperaturbereich ein und beide beeinflussen die Sprungtemperatur, so dass eine Verwandtschaft der Effekte nahe liegt.

Auf dieser Grundlage untersuchen wir verschiedene experimentelle Aspekte des beständigen, photoinduzierten Effekts und diskutieren sie mit Hilfe einer numerischen Simulation zur Defektstellenverteilung. Die verwendeten Methoden umfassen Ramanspektroskopie bei ultravioletter und sichtbarer Anregungsenergie, elektrische Transportuntersuchungen, Reflexions-Anisotropie-Spektroskopie und diffuse Röntgenbeugung.

Eines der zentralen experimentellen Ergebnissen ist, dass die Zeitkonstante der Intensitätsabnahme der Ramanmoden die Abnahmegeschwindigkeit des elektrischen Widerstandes um zwei Größenordnungen übersteigt. Entgegen früherer Annahmen sind diese Effekte also nicht identisch, aber doch an einen gemeinsamen Ursprung gekoppelt. Im Modell der Sauerstoffumordnung kann der Unterschied der Reaktionszeit verschieden langen Kettenfragmenten zugeordnet und somit konsistent erklärt werden. Ein weiteres Ergebnis ist, dass die Resonanzen der Ramansignale sich mittels Reflexions-Anisotropie auf entsprechend polarisierte, ebenfalls photosensitive elektronische Anregungen zurückführen lassen. Diese Übergänge können wir konkreten Atomorten in der Einheitszelle zuordnen. Beobachtete Änderungen stimmen sehr gut mit der Ab- oder auch Zunahme von Atomen verschiedener Koordinierungszahl während eines Umordnungsprozesses überein. Motiviert durch die elektronische Anisotropie gelang es, die Existenz einer weiteren, starken Resonanz der Defektmoden in den Ramanspektren unter ultravioletter Anregung zu zeigen.

Unsere Ergebnisse schließen einen zusätzlichen Beitrag durch Ladungsträgerpaarerzeugung zwar nicht aus, können aber vollständig im Sinne reiner struktureller Umordnung erklärt werden und unterstützen somit das Modell der Sauerstoffumordnung unter Beleuchtung.

Abstract

In this work we present studies on the persistent, photo-induced effects in high-temperature superconductors of the $R\text{Ba}_2\text{Cu}_3\text{O}_{7-\delta}$ material family (R : Y or any rare earth atom except Pm, Ce, Tb). These effects are particular to the oxygen-reduced compounds, being closely connected to their typical, fragmented Cu-O chains. One aspect is the slow increase of the conductivity and the critical temperature under illumination, which occurs on a time scale of hours. Below approximately 250 K, the induced change persists after illumination ceases, while thermally activated relaxation is observed at room temperature. This finding opens up a different way of manipulating the doping in this cuprate family, involving solely reversible changes made to the same sample specimen, but its mechanism is not yet fully understood. An effect with similar properties is known from Raman spectroscopy: Oxygen-vacancy activated modes lose intensity under illumination.

The way illumination alters the material properties is in many aspects similar to that of thermally activated oxygen-atom reordering, during which vacancies in the Cu-O chains build regular patterns with periodicity larger than that of the unit cell. For example, thermal reordering occurs in the same temperature range as the relaxation from the photo-induced state, and both affect the conductivity as well as the critical temperature.

Based on this connection we study several physical aspects of the photo-induced effect and discuss the results with support from numerical simulations of the defect distribution. Our methods include Raman spectroscopy under visible and ultraviolet excitation energy, electrical transport experiments, reflectance anisotropy spectroscopy and X-ray scattering.

Among the central experimental results is the fact that the time constant of intensity loss of the Raman modes is about two orders of magnitude faster than the increase of electrical conductivity. In contrast to previous assumptions, the two observations are thus not identical, but still related to the same microscopic process. In the oxygen reordering model, optical and electrical response can be attributed to the dynamics of chains of different length and are thus consistently explained. As another result, we established a correlation between the resonances of the defect-induced Raman modes and anisotropic, photo-sensitive features in the reflectance. The corresponding electronic transitions were assigned to specific structural elements of the unit cell, thus explaining the observed strengthening or weakening of the resonances in terms of a change in coordination numbers of the chain Cu atoms. Motivated by the optical anisotropy we found another strong resonance of the oxygen-vacancy activated modes under UV excitation.

Our results support oxygen vacancy reordering as the underlying mechanism of the persistent photo-induced effects in oxygen-reduced $R\text{Ba}_2\text{Cu}_3\text{O}_{7-\delta}$, as it can consistently explain all findings. While the observations do not exclude the possibility of an additional contribution of electronic effects like carrier trapping, they are at variance with a purely electronic model.

List of publications

Teile dieser Arbeit wurden bereits veröffentlicht:

P. M. Rafailov, S. Bahrs, and C. Thomsen,
“The Raman spectra of MgB_2 and its potential impurity phases”,
phys. stat. sol. (b) **226**, R9 (2001).

S. Bahrs, A. R. Goñi, C. Thomsen, B. Maiorov, G. Nieva, and A. Fainstein,
“Rare-earth dependence of photoinduced chain-oxygen ordering in $\text{RBa}_2\text{Cu}_3\text{O}_{7-x}$ ($x \approx 0.3$)
investigated by Raman scattering”,
Phys. Rev. B **65**, 024 522 (2002).

S. Bahrs, A. R. Goñi, B. Maiorov, G. N. Nieva, A. Fainstein, and C. Thomsen,
“Raman-study of photoinduced chain-oxygen ordering in $\text{RBa}_2\text{Cu}_3\text{O}_{(7-\delta)}$ ”,
IEEE Trans. Appl. Supercond. **13**, 3192 (2003).

A. Bruchhausen, S. Bahrs, K. Fleischer, A. R. Goñi, A. Fainstein, G. Nieva, A. A. Aligia, W.
Richter, and C. Thomsen,
“Photoinduced chain-oxygen ordering in detwinned $\text{YBa}_2\text{Cu}_3\text{O}_{6.7}$ single crystals”,
Phys. Rev. B **69**, 224 508 (2004).

S. Bahrs, A. R. Goñi, C. Thomsen, B. Maiorov, G. Nieva, and A. Fainstein,
“Light-induced oxygen-ordering dynamics in $(\text{Y,Pr})\text{Ba}_2\text{Cu}_3\text{O}_{6.7}$: A Raman spectroscopy and
Monte Carlo study”,
Phys. Rev. B **70**, 014 512 (2004).

S. Bahrs, S. Reich, A. Zwick, A. R. Goñi, W. Bacsa, G. Nieva, and C. Thomsen,
“Raman spectroscopy with UV excitation on untwinned single crystals of $\text{YBa}_2\text{Cu}_3\text{O}_{7-\delta}$ ”,
phys. stat. sol. (b) **241**, R63 (2004).

S. Bahrs, J. Guimpel, A. R. Goñi, B. Maiorov, A. Fainstein, G. Nieva, and C. Thomsen,
“Persistent photo-excitation in $\text{GdBa}_2\text{Cu}_3\text{O}_{6.5}$ in a simultaneous Raman and electrical-transport
experiment”,
Phys. Rev. B **72**, 144 501 (2005).

S. Bahrs, A. Bruchhausen, A. R. Goñi, G. Nieva, A. Fainstein, K. Fleischer, W. Richter, and C. Thomsen,
“Effect of light on the reflectance anisotropy and chain-oxygen related Raman signal in untwinned, underdoped crystals of $\text{YBa}_2\text{Cu}_3\text{O}_{7-\delta}$ ”,
to be published in J. Phys. Chem. Sol. (2005).

Manuscript under review

S. Bahrs, S. Müller, M. Rübhausen, B. Schulz, A. R. Goñi, G. Nieva, and C. Thomsen,
“Anisotropic UV-Raman resonance in underdoped $\text{YBa}_2\text{Cu}_3\text{O}_{6.7}$ ”,
submitted to Phys. Rev. B (2005).

CONTENTS

1	Motivation and Scope	3
2	Properties of high-T_c cuprates and persistent photo-induced effects	6
2.1	Structural phase diagram of oxygen-deficient $\text{YBa}_2\text{Cu}_3\text{O}_{7-\delta}$	6
2.2	Persistent Photo-Conductivity	11
2.3	Raman bleaching	15
2.4	Summary	18
3	An ASYNNNI Monte Carlo simulation of oxygen vacancy reordering	19
4	Photo-induced effects on the dielectric function	24
4.1	The dielectric function of $\text{YBa}_2\text{Cu}_3\text{O}_{7-\delta}$	25
4.2	Reflectance anisotropy spectroscopy - principle and experimental setup	29
4.3	The <i>ab</i> in-plane reflectance anisotropy of $\text{YBa}_2\text{Cu}_3\text{O}_{7-\delta}$	31
4.4	Photo-induced effects in reflectance anisotropy	33
4.5	Summary	38
5	Raman spectroscopy on oxygen-deficient $\text{YBa}_2\text{Cu}_3\text{O}_{7-\delta}$	40
5.1	Raman scattering by phonons	40
5.2	Structure, symmetry and phonon eigenvectors in $\text{YBa}_2\text{Cu}_3\text{O}_{7-\delta}$	44
5.2.1	Parameters influencing the phonon frequencies	49
5.2.2	Phonon dispersion	49
5.3	Raman experimental details	51
5.3.1	Dilor XY 800, Berlin	51
5.3.2	Dilor spectrometer equipped for UV, Toulouse	52
5.3.3	UV-VUV Raman spectrometer UT-3, Hamburg	53
5.4	Oxygen-vacancy activated phonons	53
5.4.1	Systematic variation of the rare earth atom and the oxygen concentration	55
5.4.2	Resonant Raman scattering under visible and UV excitation	58
5.4.3	The temperature dependence of oxygen-vacancy activated modes	63
5.4.4	Origin and mechanism of activation	65
5.5	Photoinduced change in Raman and oxygen-vacancy reordering	69
5.5.1	The influence of polarization: Two-color Raman bleaching	70
5.5.2	The influence of the bond-length: Raman bleaching in compounds with different rare earth atoms	71

5.5.3	Oxygen reordering dynamics in temperature-dependent Raman bleaching	73
5.5.4	Photoinduced change under UV Raman excitation	81
5.6	Summary	83
6	Electrical transport and Raman bleaching	86
6.1	Combined Raman and electrical transport setup	87
6.2	Results on simultaneous bleaching	88
6.3	Discussion within oxygen reordering picture	91
6.4	Summary	94
7	X-ray data on oxygen superstructures under laser illumination	95
7.1	Surface sensitive X-ray diffraction on beam line ID32	95
7.2	X-ray scattering from oxygen vacancy superstructures in $\text{YBa}_2\text{Cu}_3\text{O}_{7-\delta}$	97
7.3	Superstructure peaks under additional illumination in the visible	99
8	Summary and outlook	101
A	Sample preparation	105

Motivation and Scope

Since its discovery in 1911 by H. Kammerling-Onnes, superconductivity has always exerted a special kind of fascination on students, researchers, and the public alike. The abrupt expulsion of magnetic fields and the vanishing of electrical resistivity at a critical low temperature defy our common sense. It soon became obvious that the microscopic understanding of superconductivity must rely on quantum mechanical concepts. The electrodynamic approach of the London equations (1935), and especially the extension to a description based on wavefunctions by Ginzburg and Landau (1950) succeeded in describing the phenomenon. But it was not until 1957 that J. Bardeen, L. N. Cooper and R. Schrieffer developed their BCS theory, based on phonon-mediated pairing of electrons into bosonic Cooper-pairs.

They received the Nobel-prize for the BCS theory in 1972. The interest in the field is reflected by two more prizes awarded for work in the field of superconductivity, most recently in 2003 for A. A. Abrikosov, V. L. Ginzburg and A. J. Leggett for their work on the magnetic phenomena. In 1986, J. G. Bednorz, K. A. Müller published their discovery of superconductivity in the Ba-La-Cu-O system with a critical temperature T_c around 30 K. [1] It was the first breakthrough after a rather stagnant search for critical temperatures above 23 K, which was deemed close to the possible maximum in the BCS picture. Brittle, polycrystalline, badly conducting cuprates were hardly a likely candidate for good superconductivity, and the result received attention only after it was confirmed in other groups. Its full potential became clear when, about a year later, superconductivity was discovered in the related $\text{YBa}_2\text{Cu}_3\text{O}_{7-\delta}$ with T_c at 93 K, [2] putting the effect within reach of liquid nitrogen cooling for study and for technical application. A huge research effort was then initiated, making $\text{YBa}_2\text{Cu}_3\text{O}_{7-\delta}$ the most thoroughly studied cuprate compound to date, but also yielding many other high-temperature superconducting cuprates with the current record at $T_c=138$ K in Tl-doped $\text{HgBa}_2\text{Ca}_2\text{Cu}_3\text{O}_{8+\delta}$. [3, 4] From the high value of the critical temperature and from other facts like the weakness of the isotope effect in the optimally doped samples it soon became clear that the new materials could not be understood within the BCS-picture of phonon-mediated Cooper pairing of the electrons. Despite all efforts, their pairing mechanism is still an open question today – but then, another 46 years have not yet passed.

In the search for a common denominator in the variety of materials showing high-temperature superconductivity, the Cu-O₂ plane layers were identified as a central structural element. Their carrier concentration, changed by doping of the parent compound by partial substitution of elements, takes many cuprate materials through a similar electronic phase diagram from insulators via superconductors to metals, with pseudo-gap and non-fermi-liquid phases in between. The

doping phase diagram thus became one (though not the only) central point in the discussion.

In the $RBa_2Cu_3O_{7-\delta}$ -family ($R = Y$ or rare earth atom, not Ce, Pm, Tb) investigated in this work, one way to change the doping is a variation of the oxygen content δ . Apart from the oxygen concentration value, the doping is also dependent on the spatial configuration of the oxygen vacancies, which tend to build ordered phases. Samples with the same composition can thus display differences in critical temperatures of up to 10 K, depending on their annealing history. [5]

In this work we focus on another way of tuning the doping level: the conductivity and the critical temperature can be enhanced by exposure to visible light. This persistent photoconductivity, or photo-superconductivity, develops on a time-scale of hours. It is persistent in the sense that the change remains stable after illumination at low temperatures (below ≈ 250 K), but reversible because it relaxes within hours in the dark at room temperature. [6, 7]

Persistent photo-induced effects are specific to the oxygen-reduced compounds of the $RBa_2Cu_3O_{7-\delta}$ -family. The mechanism for the effect is still under debate, though all explanations suggested acknowledge the central role of the oxygen vacancy sites and the connection to superconductivity via carrier doping. The main controversy is between a purely electronic model, [8] in which trapped carrier pairs enhance the carrier concentration, and a structural model, where the reordering of oxygen-vacancy sites changes the carrier doping analogous to the reordering during thermal annealing. [9] Some groups suggest a mixture of both mechanisms. [10]

Persistent photo-induced effects are also apparent in the optical properties of the material. Wake *et al.* have shown in 1991 that the Raman response of specific, oxygen-vacancy activated modes decreases under illumination. [11] The discussion on the microscopic mechanism of activation of the modes is not conclusive, but the phenomenon shares properties such as metastability and reversibility with the effect in electrical transport, and was also discussed within the oxygen reordering model. In the course of this work, it became clear that the dielectric function is also affected in the visible to the UV range, making optical experiments a versatile tool for the study of the effect. Another consequence is that photo-induced change should be taken into account in any optical study of the material, as it can interfere with the reproducibility of results.

The advantages of illumination-induced doping are thus its continuity, reversibility, easy and fine control, and that it can be performed on the same sample, excluding the possible errors that come with an entire set of differently treated samples. Disadvantageous, on the other hand, is the small scale of the change, the confinement to the surface penetrated by light - and last but not least, that the microscopic mechanism of photo-induced effects is not well understood.

The aim of this work therefore is a study of the optical persistent photo-induced effects in underdoped $YBa_2Cu_3O_{7-\delta}$, their relation to the effect in electrical transport, and their microscopic origin. Among the models proposed, we chose the oxygen-vacancy reordering picture of photo-induced change and explore the capability of this model to consistently explain the experimental findings.

In the following chapter, we give a very brief description of the properties of $YBa_2Cu_3O_{7-\delta}$

relevant in this context, in particular on the oxygen vacancy ordered phases, followed by a short review of the information on persistent photoconductivity and photo-induced change in Raman spectroscopy available in the literature. For the discussion of our experimental results within the framework of the vacancy reordering model, we set up a simulation based on the Asymmetric next-nearest neighbor Ising (ASYNNNI) model in Chap. 3. Experimental studies on the illumination-induced effects on the dielectric function using reflectance anisotropy spectroscopy are presented in Chap. 4. Chapter 5 contains Raman studies on known as well as newly discovered oxygen-vacancy activated modes under visible and UV excitation. The relation between the optical and the electrical transport effects within the vacancy reordering model is investigated in Chap. 6 using a simultaneous Raman-and-transport experiment. Chapter 7 is dedicated to the direct detection of structural change using x-ray diffraction, before we discuss all results in context in the final chapter.

CHAPTER 2

Properties of high- T_c cuprates and persistent photo-induced effects

High-temperature superconductivity in the cuprates is a vast field of research, and a full account of their properties, the methods of investigation and the theories discussed for the mechanism is clearly beyond our scope. Some orientation on recent development can be gained, for example, from the short review article by J. Orenstein *et al.* [12], from the recently revised edition of the introductory superconductivity course book by W. Buckel and R. Kleiner [13], or, with exclusive focus on the cuprates, from the conference summary made available by the group of I. Schuller in 2002. [14] Here we are restricted to the information which is an immediate prerequisite for the discussion of persistent photo-induced effects. We show the phase diagram of underdoped, oxygen deficient $\text{YBa}_2\text{Cu}_3\text{O}_{7-\delta}$ with oxygen superstructures, and the related increase in T_c during annealing. The latter is in many respects similar to the persistent photo-induced effects, motivating our model of vacancy reordering. We then review briefly the information available on persistent photoconductivity (ppc), and the corresponding photo-induced effects in Raman spectroscopy on $\text{YBa}_2\text{Cu}_3\text{O}_{7-\delta}$.

2.1 Structural phase diagram of oxygen-deficient $\text{YBa}_2\text{Cu}_3\text{O}_{7-\delta}$

Due to the complex material system, establishing the precise experimental phenomenology of the cuprates has been a challenging and sometimes controversial process. They show a variety of uncommon properties, all of which are dependent on composition, granularity of the sample, abundance of defects etc., and results can be very sensitive to sample preparation. However, in the process a phase diagram of carrier concentration versus temperature emerged, which is essentially similar for all hole-doped cuprates (only a few electron-doped high- T_c materials were found). A schematic diagram taken from a review by Orenstein *et al.* [12] is shown in

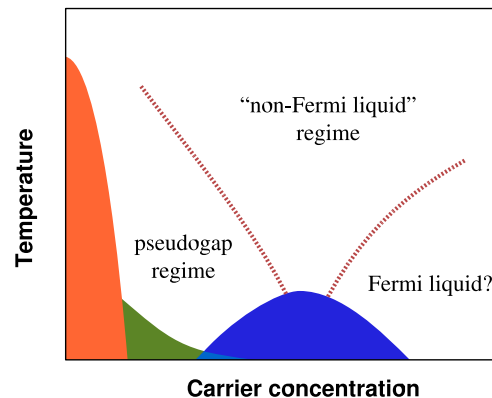


Figure 2.1: Schematic electronic phase diagram of high- T_c superconductors as shown in Ref. [12]. The blue dome is the superconducting phase. The orange area is a magnetically ordered, Mott insulating phase, and the green area an extension with more complicated magnetic order.

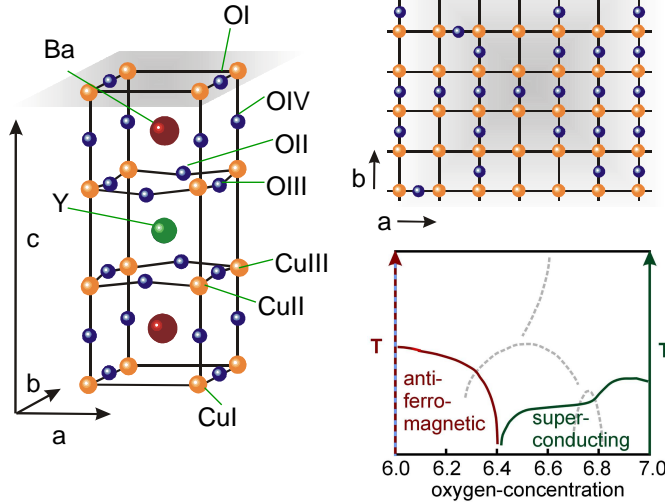


Figure 2.2: Unit cell of $\text{YBa}_2\text{Cu}_3\text{O}_{7-\delta}$. The inequivalent sites of elements in the cell are numbered. The top right panel shows a cut through the ab chain plane in the oxygen-deficient compound. The lower panel shows the schematic electronic phase diagram for this case: $\text{YBa}_2\text{Cu}_3\text{O}_6$ is insulating, antiferromagnetic, and has no oxygen atoms in the chain plane. $\text{YBa}_2\text{Cu}_3\text{O}_7$ is superconducting and has an oxygen between each pair of Cu in b -direction, but not in a .

Fig. 2.1. Though the cuprates are not good insulators nor good metals, the variation of doping can take them from a state similar to the former to one similar to the latter. The point of highest critical temperature is conventionally referred to as “optimal doping”. In the underdoped regime, the cuprates show signs of a gap opening in the electronic bands well before the onset of superconductivity. The nature of this so-called pseudo-gap is still under discussion.

In $\text{YBa}_2\text{Cu}_3\text{O}_{7-\delta}$, the change of oxygen content from $\delta = 1$ to $\delta = 0$ is one possibility to change the doping, covering the range from an antiferromagnetic insulator $\text{YBa}_2\text{Cu}_3\text{O}_6$ to the superconducting $\text{YBa}_2\text{Cu}_3\text{O}_7$. The optimum doping is at $\delta=0.07$ to 0.08 , with $T_c=93$ K, close to the fully oxygenated side. [15] Figure 2.2 shows a schematic phase diagram and a unit cell of $\text{YBa}_2\text{Cu}_3\text{O}_7$. The layered structure with superconducting planes of Cu and oxygen is typical for the cuprates. Two such planes, where an oxygen atom (OII, OIII) is situated between Cu atoms (CuII, CuIII) at the corners at slightly bend angles, can be seen above and below the central Y atom. Y can be replaced by any rare earth atom except Pr (does not become superconducting), Ce, Tb (do not build the structure), and Pm (radioactive, not tested), and still yield a superconductor with T_c above 90 K, defining the $\text{RBA}_2\text{Cu}_3\text{O}_{7-\delta}$ -material family (R rare earth, Y). [16] The a and b directions are almost identical, but an additional layer of Cu atoms (CuI) has oxygen neighbors (OI) in the b direction only. In the fully oxygenated compound, chains made up from these CuI and OI atoms run in the b direction in a cut through the ab -plane, as shown in the upper right panel in Fig. 2.2. Crystalline samples can be twinned, that is, they have domains with swapped a and b axis direction, ranging in size from a few 100 nm to macroscopic dimensions. [17]

When δ increases, oxygen vacancies occur in these OI sites, before any of the other sites in the cell are much affected. This results in broken Cu-O chain fragments, as drawn in the ab plane in Fig. 2.2. In $\text{YBa}_2\text{Cu}_3\text{O}_6$ the oxygen atoms in OI sites are completely absent and the structure is tetragonal. The extend of oxygen deficiency determines the orthorhombicity as well as the doping

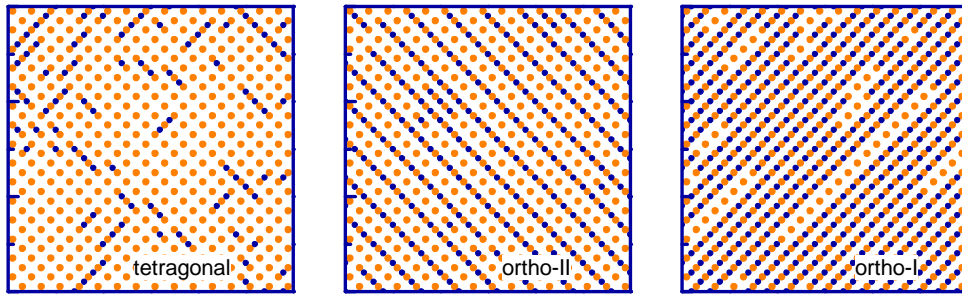


Figure 2.3: A basic picture of the structural phase diagram with examples of superstructure-ordered phases (orange symbols: Cu, blue symbols: oxygen. a and b run along the diagonals of the picture boundaries). The oxygen vacancies tend to order into full and empty Cu-O chains, which order with a periodicity larger than one unit cell in the perpendicular direction, like the full-empty-full ortho-II pattern in the middle panel.

of the superconducting planes. With increasing δ , T_c decreases, and at $\delta \approx 0.6$ a transition to the insulating, antiferromagnetic, and tetragonal phase occurs.

The critical temperature versus oxygen concentration displays a plateau roughly between 6.6 and 6.8, where $T_c \approx 60$ K is almost constant. [18, 19] Numerous experimental and theoretical studies have shown that this is connected to a structural ordering phenomenon. The oxygen vacancies in the chain plane order into patterns with a periodicity exceeding that of the unit cell, so-called superstructures. [17–25] Figure 2.3 displays examples of these phases. For very little oxygen in the chain plane, like in the leftmost panel, randomly distributed and oriented short fragments develop and the phase is tetragonal. In the rightmost panel with full oxygenation, one long and oriented chain per unit cell exists, defining its direction as b and the phase as ortho-I. At half oxygen content in the middle panel, instead of arranging in random short fragments, the oxygen vacancies order into alternating full and completely empty (only Cu) chains. The name ortho-II originates from the fact that their periodicity is doubling the original unit cell. Patterns with varying periodicity are thus found for different values of oxygen content, and constitute phases in the diagram. The vacancy ordering also causes a slight shift in all other atomic positions in the unit cell. [17, 25, 26] Recently, it has been discussed with renewed interest as a source for charge density fluctuations (“stripes”). [23, 25, 27]

The phase diagram was extensively studied using Monte-Carlo simulations based on a two-dimensional Ising model with anisotropic interaction parameters for neighboring oxygen atoms in the plane. [19, 23, 24, 28–30] With more experimental data available it became increasingly clear that the oxygen superstructures can have much more complex ordering patterns than just ortho-II, although this is the only superstructure found to develop true long-range ordering. [17] Figure 2.4 shows a recent version of the full phase diagram by de Fontaine *et al.*, featuring a large number of phases in the narrow range of the T_c -plateau with a periodicity up to eight times that of the unit cell. Experimentally, the superstructure phases have been observed by neutron diffraction

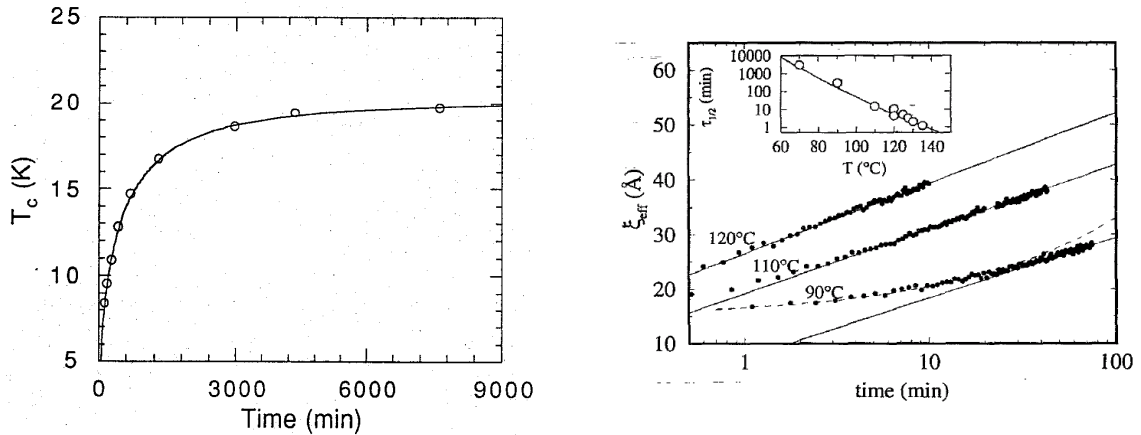


Figure 2.6: Left panel: Increase of T_c during room-temperature annealing after quenching the sample from high temperatures, from Jorgensen *et al.* [5]. Right panel: Increase of correlation length of the ortho-II superstructure in X-ray experiments during room annealing at the given temperatures, from Schleger *et al.* [32].

c lengthening in the tetragonal compounds. [33] Likewise, an underdoped compound with an ordered superstructure has more orthorhombicity and shorter c than a sample with randomly distributed vacancies. Schleger *et al.* observed directly the development of the ortho-II phase under different annealing conditions, which is reproduced in Fig. 2.6. [32] In a similar line of thought, Sadewasser *et al.* have shown, for example, that the application of pressure changes the critical temperature of the sample, and interpret their results within an oxygen-reordering picture of the change in T_c .

Oxygen reordering dynamics have been studied theoretically in the two-dimensional Ising model. [34–37] They do not follow a simple exponential relaxation law and most groups identify two consecutive growth processes: At first a merging of oxygen atoms into chains, which as an entity are less mobile in the plane, and then a second stage where the boundaries between differently ordered domains are displaced. Thermal reordering is slow at room temperature and freezes soon below. For the reproducible preparation of samples, this can be a practical disadvantage, which presumably accounts for some variance in experimental data in the underdoped compounds. In $\text{YBa}_2\text{Cu}_3\text{O}_{6.95}$, close to full oxygenation, even a glass-like transition was found in the thermal expansion coefficient which is attributed to oxygen reordering. [38]

Having established the chain-oxygen superstructures and the reordering during room-temperature annealing which is affecting T_c , it remains to explain the connection between the chain length and the electronic configuration. Early after the discovery of superconductivity in $\text{YBa}_2\text{Cu}_3\text{O}_{7-\delta}$, the Cu-O chains were thought to play a vital role for the coupling mechanism. It soon became clear, though, that the Cu-O₂-planes were carrying the superconductivity, reducing the chains to a doping reservoir for holes. Studies based on the Hubbard model by Latgé *et al.* [39] and by Aligia *et al.* [40] show that the hole doping is dependent on the valence state,

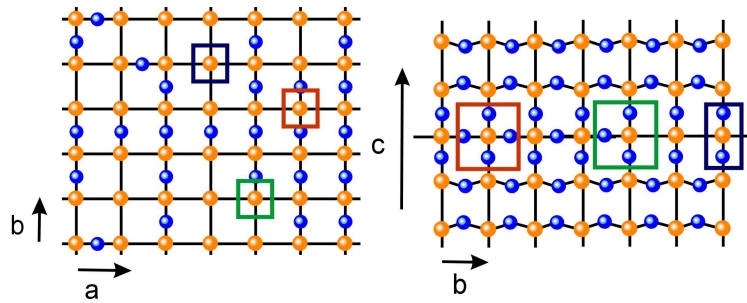


Figure 2.7: Cuts through the ab and the bc planes in the oxygen-deficient structure. Oxygen vacancy sites in the chain plane lead to differently coordinated CuI atoms. The blue marker highlights a “lone” Cu atom with oxygen neighbors along the c -axis only, which corresponds to the situation in the insulating compound, sometimes termed “Cu-O dumbbell”. We will refer to it as two-fold coordinated. The green marker highlights CuI atoms at the end of a chain fragment or a monomer, with three neighboring oxygen atoms, three-fold coordinated. The red marker shows a CuI incorporated in a chain, with four-fold oxygen coordination.

and therefore on the oxygen-coordination number of the chain-Cu atoms. Figure 2.7 illustrates the idea. In their argumentation, an average of two-fold coordinated Cu atoms (empty chain) and four-fold coordinated Cu atoms (in a full chain) in an ordered phase yields more hole doping than the equivalent number of Cu atoms with three-fold coordination (at a chain end or a monomer) in a random phase. Latgé *et al.* have calculated the number of holes transferred to the superconducting planes for varying oxygen content, comparing a random and an ordered phase for each point, with good agreement with the observed change during thermal annealing. [39] There is also some evidence for a minimum chain-fragment length required, before the charger transfer takes place, and especially before the chain plane takes part in carrying supercurrents. [41–43]

2.2 Persistent Photo-Conductivity

The slow, reversible reaction to irradiation with visible light called *persistent photoconductivity* or *persistent photo-superconductivity* (PPC/PPS) is a property unique to the oxygen-deficient $R\text{Ba}_2\text{Cu}_3\text{O}_{7-\delta}$ -compounds. Figure 2.8 illustrates the basic effect. Under illumination, the resistivity of a $\text{YBa}_2\text{Cu}_3\text{O}_{6.5}$ -film decreases, while the mobility increases, on a time scale of hours. After the illumination ceases, both quantities recover their original value on the same time scale at room temperature, so it is reversible at room temperature. [6, 7, 44, 47] The time scale is fundamentally different from the transient photoconductivity, which also occurs in the material due to photoexcited charge transfer, but on a typical time scale of 10 ns. PPC/PPS works at low temperatures, and is independent from the (super)conducting state of the sample. [48] Below 273 K for semiconducting, [49] or 254 K for superconducting films [50], the induced change is stable within laboratory time scale (for example, $\frac{\Delta R}{R} < 1\%$ in the dark at 10 K [49]). For this reason, the

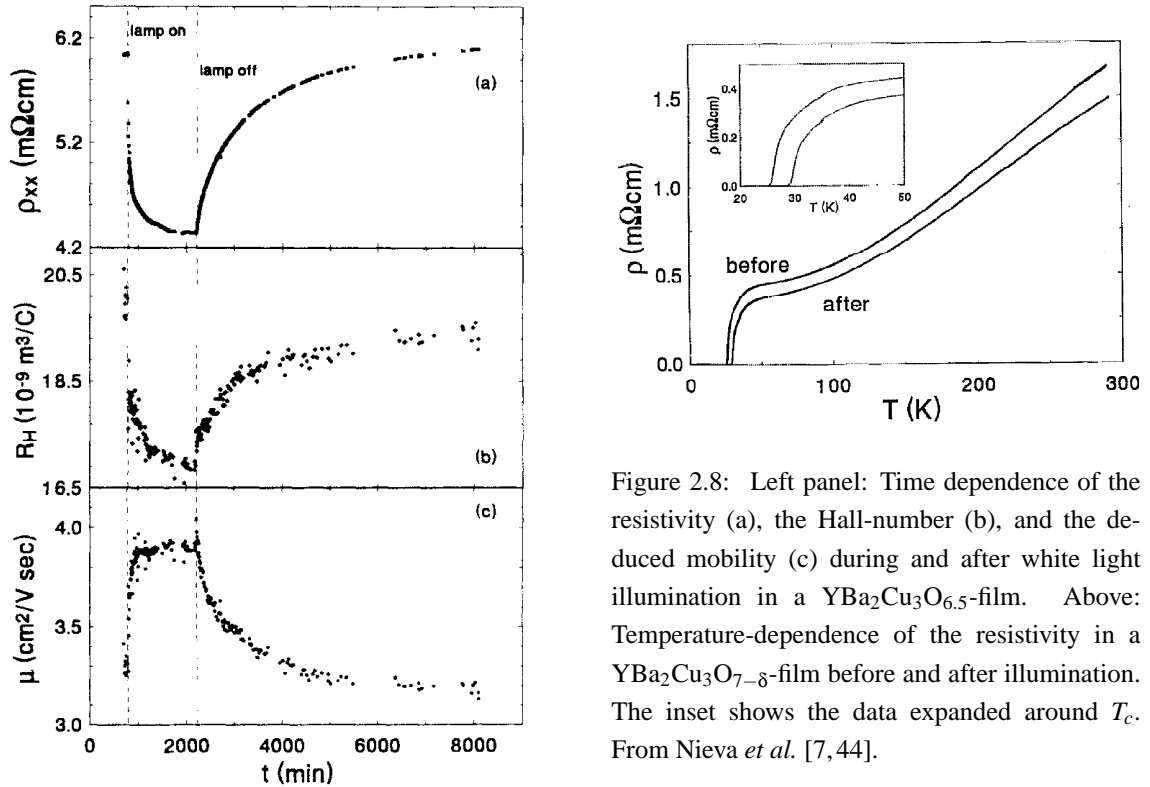


Figure 2.8: Left panel: Time dependence of the resistivity (a), the Hall-number (b), and the deduced mobility (c) during and after white light illumination in a $\text{YBa}_2\text{Cu}_3\text{O}_{6.5}$ -film. Above: Temperature-dependence of the resistivity in a $\text{YBa}_2\text{Cu}_3\text{O}_{7-\delta}$ -film before and after illumination. The inset shows the data expanded around T_c . From Nieva *et al.* [7, 44].

resistivity can be measured versus temperature up to this range unperturbed by time-dependent effects, as was done in the right panel of Fig. 2.8. Irradiation induces a downward shift of the entire curve, so that the superconducting temperature is affected along with the conductivity in the normal state. Figure 2.9(a) shows the difference in T_c reached with the same photon dose in samples with varying oxygen contents. The largest difference δT_c achieved was 7 K in a sample near to the superconducting/insulating transition, setting the order of magnitude. [9] The change in critical temperature follows that achieved by thermal reordering, ΔT_c , taken from Ref. [45], pointing to a close connection between the two processes. PPC is not, however, restricted to the superconducting samples. The highest absolute changes in normal-state resistivity are achieved for films in the transition range of oxygen content around 6.4, [51] and even a transformation from insulating to superconducting characteristics is possible. [49] According to Nieva *et al.* the increase saturates at different levels for each oxygen concentration, so not all oxygen vacancies can be compensated persistently by illumination. [7, 44]

Another interesting aspect is that irradiation with visible light shortens the c -axis length, indicating increased orthorhombicity and consequently a direct link to the structural properties of the compound. [52, 53]

Guimpel *et al.* have explicitly tested whether thermal disorder and PPC cancel each other, as both seem connected to oxygen reordering. [46] In Fig. 2.9(b) a disordered high temperature

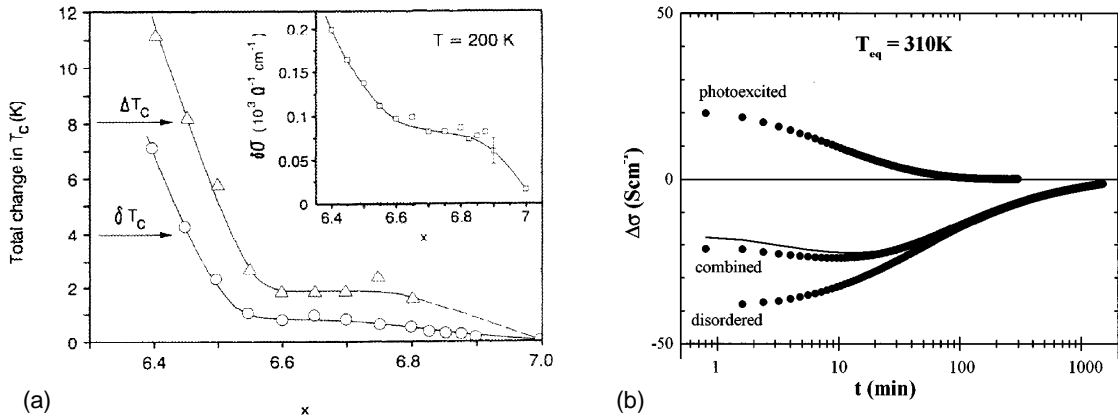


Figure 2.9: (a) Total change of T_c versus oxygen content in $\text{YBa}_2\text{Cu}_3\text{O}_{7-\delta}$, ΔT_c after thermal annealing, δT_c after a defined dose of illumination. Both changes show identical trend. From Osquiguil *et al.* [9], part of the data from [45]. (b) Relaxation of a $\text{YBa}_2\text{Cu}_3\text{O}_{7-\delta}$ film at 310 K following special preparation: In “disordered” it was quenched from 350 to 200 K and then left to relax at 310 K, in “photoexcited” it was cooled to 150 K and illuminated, then left to relax at 310 K, and in “combined” the sample was quenched, illuminated to compensate for the disorder, then warmed back to 310 K. As the combined curve is not flat, photoexcitation and thermal annealing do not cancel each other. From Guimpel *et al.* [46].

state was quenched to low temperatures and then illuminated to compensate the loss of resistivity. As can be seen from the non-constant curve upon subsequent annealing at room temperature, the effects do not cancel. Systematic Hall measurements during thermal annealing, under illumination and during relaxation afterwards have shown that photoexcitation has a stronger effect on carrier mobility than annealing. [54] They also established a hysteresis between T_c and the normal-state carrier density, which have different ratios during irradiation and annealing, indicating that the relaxation is thermally driven.

The time dependence of PPC/PPS and its relaxation are non-exponential. They resemble the dependence of T_c versus annealing time (see Fig. 2.6), which is expected to reflect non-exponential growth of chain patterns. [32, 34–36] Several groups used a stretched exponential function (with one additional parameter compared to an exponential) for their description, which we also apply to our Raman results, and therefore denote in Eq. 5.14 in Chap. 5. For the thermally-activated relaxation of PPC, Kudinov *et al.* and Markowitsch *et al.* determined an energy barrier of $\Delta E = 0.906$ eV and 0.935 eV, respectively. [49, 50] Temperature-dependent PPC onset was investigated in Ref. [10], showing also a stretched exponential characteristic, but interestingly non-monotonic behavior of the mobility at room temperature illumination. While this is at variance with the data in Fig. 2.8, the applied photon dose in Markowitsch’s experiment was much smaller, so an effect of thermal relaxation might interfere, which is not visible in Fig. 2.8.

Kudinov *et al.* ascertained that the induced change is proportional to the total photon dose, and not to the power, so PPC/PPS can be viewed as a one-photon process. Its spectral dependence has been investigated by several groups, all of which find no PPC for excitation below ≈ 1.5 eV, or even a small reversal of 2%. [55–57] We reproduce the data from Endo *et al.* in Fig. 2.10, since it includes the UV range. At 4 eV, a strong peak was found in the PPC efficiency, which coincides with an electronic resonance discussed along with results in RAS and Raman in Chaps. 4 and 5.

The correct interpretation of PPC/PPS has been subject to an intense discussion between essentially two models: While it is clear that the oxygen vacancy sites in the Cu-O chains of $\text{YBa}_2\text{Cu}_3\text{O}_{7-\delta}$ must be involved, they can either trap the carriers excited by illumination as in the *charge transfer model*, [8] or they can rearrange into more ordered structures with the assistance of photoexcitation, enabling movement at low temperatures where thermal reordering is frozen, as in the *photo-assisted oxygen reordering model*. [9] In recent work, some groups suggest a mixed model involving both mechanisms. [10]

The advantages of charge transfer are that the increased carrier density and the spectral dependence of PPC/PPS are explained naturally from the electronic band-structure of a semiconducting solid with local defects. They also account for a large change in samples around 6.4 oxygen content with many defect sites, and it would be no surprise if charge transfer did not cancel with thermal reordering. On the other hand, charge transfer is difficult to reconcile with the limited maximum change achieved through illumination, and it is not obvious that the charge traps with a high energy barrier of 1 eV can exist in a metallic sample. The charge transfer mechanism is also at odds with a weak increase in carrier density, but a strong one in mobility. Especially the fact that there is a hysteresis with the relaxation – the system is not returning by an identical path of T_c versus carrier density – is at odds with a purely electronic effect, which should take in and release carriers in the defect-sites with the same impact on carrier density and mobility. [54]

Photoassisted oxygen reordering has to rely on the spectral dependence from the excitation enabling the oxygen atoms to move. If the charge transfer occurs through chain lengthening, it has difficulty to explain a maximum change in strongly underdoped samples, though the amount of increase in T_c follows the one obtained through oxygen reordering in the metallic range very

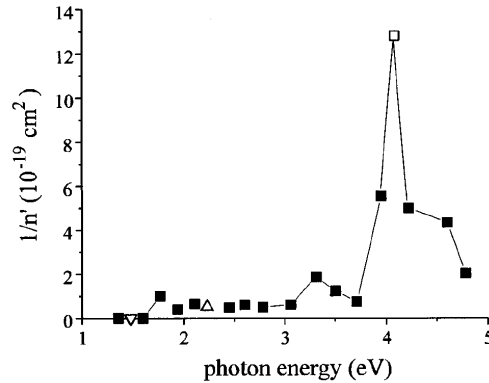


Figure 2.10: Spectral efficiency of the persistent photoconductivity by Endo *et al.* [55]: $1/n'$ vs photon energy. n' is the number of photons per unit area necessary for a 2% change in the resistance. While the efficiency goes to zero in the infrared, there is some induced change throughout the visible regime and a strong peak in the UV at 4 eV.

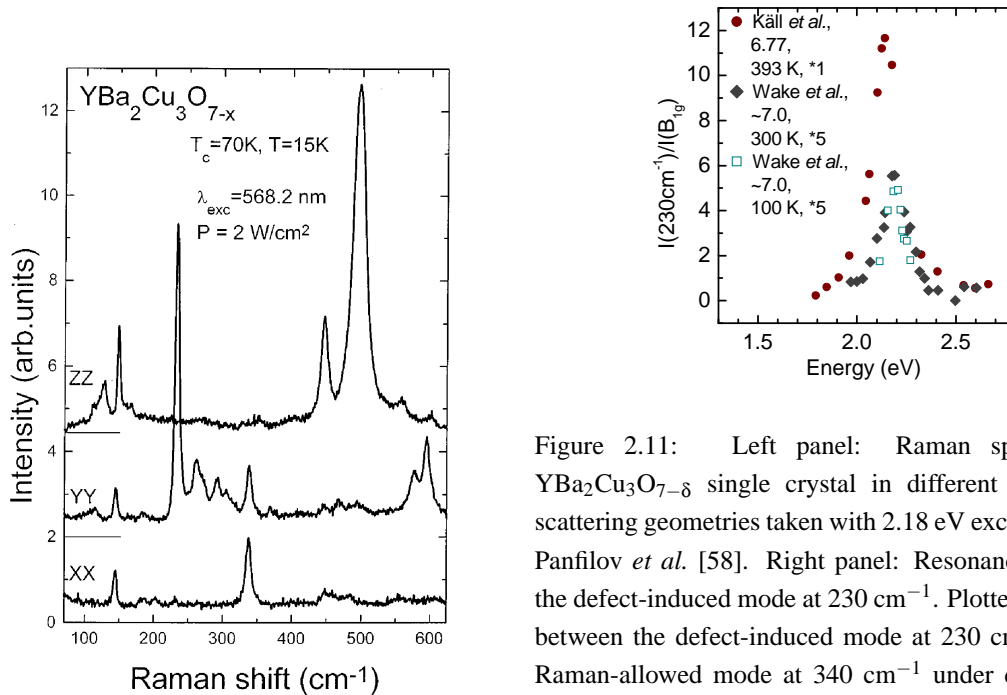


Figure 2.11: Left panel: Raman spectra of a $\text{YBa}_2\text{Cu}_3\text{O}_{7-\delta}$ single crystal in different polarization scattering geometries taken with 2.18 eV excitation, from Panfilov *et al.* [58]. Right panel: Resonance profile of the defect-induced mode at 230 cm^{-1} . Plotted is the ratio between the defect-induced mode at 230 cm^{-1} and the Raman-allowed mode at 340 cm^{-1} under different excitation energies. The data was taken from Refs. [11] and [59].

convincingly. A change of c -axis length is also straightforwardly explained. The fact that it does not cancel with thermal annealing, and that the mobility is reacting stronger to illumination than the carrier concentration is difficult to reconcile at first sight. However, this can be understood when the final state of ordering caused by irradiation deviates from purely thermal equilibrium. For example, short fragments can be appended to the longer chains by photoexcitation quickly, while the long-range order is largely unaffected. [54]

We conclude that two possibilities remain for the mechanism of PPC/PPS: Either the observed phenomena are due to photo-assisted oxygen reordering, where illumination and thermal annealing initiate different types of order, or alternatively, both ordering and trapping of charge carriers trapped in vacancy sites contribute to the effect.

2.3 Raman bleaching

Shortly after the discovery of PPC/PPS, Wake *et al.* have reported a persistent photo-induced effect in the Raman spectra of $\text{YBa}_2\text{Cu}_3\text{O}_{7-\delta}$. [11] Raman spectroscopy was applied to $\text{YBa}_2\text{Cu}_3\text{O}_{7-\delta}$ soon after its discovery, and five strong Raman-allowed modes had been assigned to A_g symmetry vibrations on the basis of shell model calculations by Liu *et al.* in 1988. [62] They also identified a number of peaks with a symmetry which was at odds with the group of the crystal structure, concluded that these were defect-induced. In fact, these modes are absent in the fully oxygenated

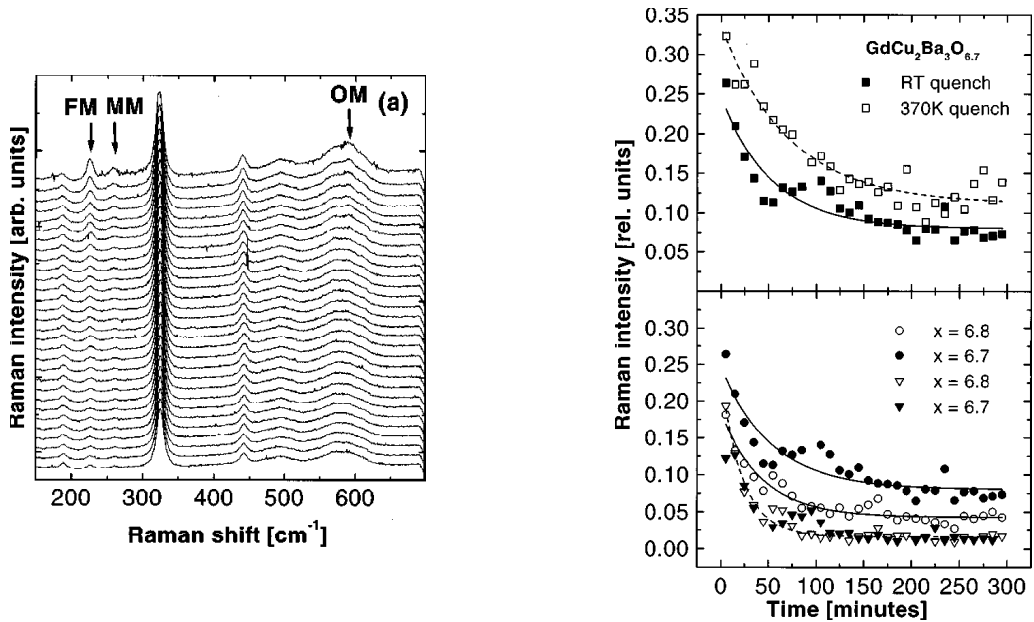


Figure 2.12: Bleaching of defect-induced modes in Raman spectra on $\text{GdBa}_2\text{Cu}_3\text{O}_{7-\delta}$ from Fainstein *et al.* [60]. Left panel: Sequential Raman spectra of $\text{GdBa}_2\text{Cu}_3\text{O}_{6.8}$ taken at 80 K with 10 min integration time at 514 nm excitation, starting at the top. The peaks marked FM, MM and OM decrease while Raman-allowed modes at 340 and 440 cm^{-1} remain constant. Right panel: The intensity of the defect-induced peaks versus illumination time in $\text{GdBa}_2\text{Cu}_3\text{O}_{6.7}$ and $\text{GdBa}_2\text{Cu}_3\text{O}_{6.8}$. The upper right panel shows Raman intensities versus illumination time after quenches from two different initial temperatures, room temperature and 370 K. The lower panel shows intensities of the peaks marked FM (circles) and MM (triangles) versus illumination time.

compound. We will discuss the Raman response of $\text{YBa}_2\text{Cu}_3\text{O}_{7-\delta}$ in more detail in Chap. 5.

Wake *et al.* reported a resonance profile centered around 2.18 eV with FWHM 160 meV for one of the modes, which is shown in the right panel of Fig. 2.11 together with resonance data by another group. [61] The left panel displays Raman spectra of an underdoped single crystal of $\text{YBa}_2\text{Cu}_3\text{O}_{7-\delta}$ under resonant excitation in scattering geometries with polarization along the three crystal axes. The five Raman-allowed modes at 115, 150, 340, 440 and 490 cm^{-1} are observed with varying strength in different geometries, as expected. In addition, strong defect-induced lines at 230, 260, 290, 305, 365, 575 and 595 cm^{-1} appear exclusively for incident and detected polarization along the chain-direction b .

Most unusual for the Raman response of any material under constant conditions, the defect-induced modes lose intensity in sequentially taken Raman spectra, as is shown in Fig. 2.12. [60,63] The left panel presents a sequence of Raman spectra taken with non-resonant 514 nm excitation, where the defect-induced modes are weaker but clearly present. In the right panel, the intensities of two of the modes were plotted versus the accumulation time of the Raman spectra in the sequence, showing the typical slow time scale of the order of hours. The Raman-allowed modes remain unaltered, and it was shown by several groups that the resonance recovers completely upon

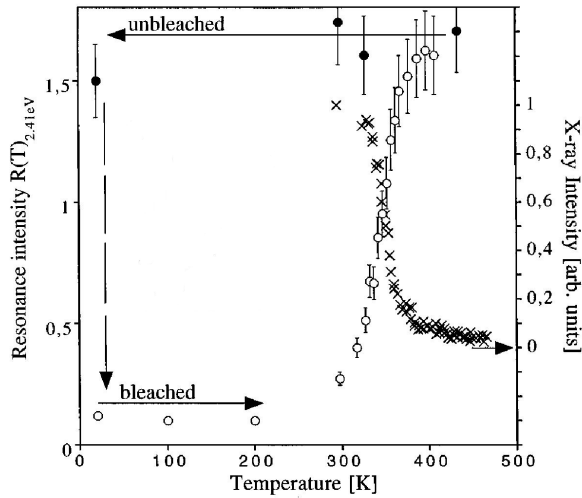


Figure 2.13: Bleaching, low temperature stability and recovery of the resonance intensity in $\text{YBa}_2\text{Cu}_3\text{O}_{6.77}$ from Käll *et al.* [61]. The resonance intensity in the bleached (open circles) and unbleached (filled circles) state is plotted together with the intensity of the ortho-III x-ray peak data (crosses) from Schleger *et al.* [31].

annealing between room temperature and 100°C , [11, 60, 61, 64] so that a destructive or corrosive process can be ruled out. Panfilov *et al.* confirmed that the intensity ratio of defect-induced and allowed modes is constant for different excitation power. [59]

Like PPC/PPS, this *Raman bleaching* occurs in oxygen deficient samples only, with a maximum intensity ratio compared to allowed modes around a content of 6.7, [59, 60] but is not restricted to $R=Y$ (the data in Fig. 2.12 is, *e.g.*, for $R=\text{Gd}$). As is shown in Fig. 2.13, it also displays metastability at low temperatures, and an onset of recovery just below room temperature, so that the Raman resonance can be cycled through equilibrium at room temperature, quenching to low temperature, bleaching, stability at low temperature and recovery upon warming. Studies of the temperature dependence of the bleaching were done by Panfilov *et al.* and will be compared to our own results in Chap. 5. [58, 59]

Fainstein *et al.* have shown that the strength of the resonance increases upon warming to 370 K, and that quenching from higher initial temperatures result in higher intensities in the bleaching sequences (see Fig. 2.12 right upper panel), pointing to the intimate connection to oxygen-vacancy disorder. [60] The data by Käll *et al.* has been directly compared to the intensity of the X-ray peak corresponding to ortho-III ordering in their sample in Fig. 2.13, showing that the recovery of the bleached state is occurring in the same temperature range as the destruction of the ordered phase. [61, 64]

Based on this close connection to the oxygen vacancy defects and on the prediction from early shell model calculations, the bleaching modes were previously ascribed to chain-vibrations. [62, 65] In particular for the peak at 595 cm^{-1} , this was supported by a site-selective isotope substitution experiment with ^{18}O , which displayed a frequency shift appropriate for substitutions in the most easily affected chain plane. [66] However, recent *ab-initio* calculations are at variance with this assignment, [67] reopening the discussion. Different suggestions were also made for the mechanism by which the defect-induced modes are activated in the Raman spectra. While it is

clear that the vacancies are involved, they can either host a resonance which is responsible for the activation, or disable selection rules via the violation of the ideal symmetry of the crystal. We will revisit both issues in connection with our Raman results in Chap. 5.

A natural consequence of the similar properties discussed above is that PPC/PPS and Raman bleaching are both discussed within the same models for persistent photo-induced change. Raman bleaching can thus either be caused by vanishing of defect sites at the end of short chain fragments during superstructure development, or the intensity of the resonantly activated modes can decrease as resonant sites are filled up with trapped photoexcited carriers.

2.4 Summary

A considerable amount of research has been carried out in the field of oxygen-deficient $R\text{Ba}_2\text{Cu}_3\text{O}_{7-\delta}$ in the years since high-temperature superconductivity was discovered and found to depend crucially on the oxygen-doping in the compound. The phase diagram shows a plateau in T_c versus oxygen-concentration at 60 K. It is caused by the ordering of oxygen vacancies in the Cu-O chain plane into complex superstructures of full and empty chains with periodicities exceeding that of the unit cell. Among them, the ortho-II phase at oxygen content 6.5 develops long range order, while the other phases reach only limited coherence. The reordering of vacancies is thermally activated and freezes soon below room temperature. A more disordered equilibrium at high temperatures can thus be frozen in a quick temperature quench, and subsequently watched during a slow relaxation process. Superstructure ordering enhances the carrier concentration of the superconducting planes, because four-fold coordinated Cu atoms incorporated in a Cu-O chain are thought to efficiently dope the plane, which is not the case for two-fold Cu atoms without in-plane oxygen neighbors, or three-fold coordinated Cu at the end of a chain fragment.

Two methods have detected persistent photo-induced effects characteristic of the oxygen-deficient $R\text{Ba}_2\text{Cu}_3\text{O}_{7-\delta}$ -compounds. In electrical transport experiments, the carrier concentration and the mobility are enhanced under irradiation with light, ranging from an onset in the infrared at 1.5 eV to the UV. In Raman spectroscopy under visible excitation, defect-induced modes lose intensity under illumination by the laser light used for Raman excitation. Both effects share their connection to the broken Cu-O chains particular to the material family, their slow time scale of the order of hours, the stability at low temperatures, and the reversibility by thermal relaxation at room temperature. It is thus reasonable to search for a common microscopical origin.

Considering all arguments discussed in this chapter, two models remain in the current discussion: Persistent photo-induced effects can be caused by a reordering of the oxygen vacancies, analogous, but not identical, to the process of thermal annealing. Or alternatively, some effects are due to repositioning of oxygen in the plane, while another contribution comes from trapping of photoexcited carriers at the vacancy sites. With this situation as a starting point, we have studied persistent photo-induced effects both in the optical and the transport properties. We chose to discuss our results in the framework of the vacancy reordering model used for thermal annealing, exploring the possibilities and constraints set for the model by our experimental data.

An ASYNNNI Monte Carlo simulation of oxygen vacancy reordering

As mentioned in the previous chapter, the structural phase diagram of $\text{YBa}_2\text{Cu}_3\text{O}_{7-\delta}$ with its superstructures in the Cu-O chain plane has been studied extensively using the Monte-Carlo based “asymmetric next nearest neighbor Ising model” (ASYNNNI) by numerous groups. Motivated by the close relation between the persistent photo-induced effects and the oxygen vacancies, and by the similarity of their dynamics, we adapted a simulation of this type from the literature for comparison to our experimental results.

Our working hypothesis is that light excitation revives the site changes of oxygen atoms, enabling reordering *below* the threshold temperature on a time scale observable in the laboratory. The threshold temperature of the thermally activated reordering, and of thermal relaxation of photo-induced effects, is caused by an energy barrier which has to be overcome by the oxygen atoms in order to change site and take part in the reordering process. Photoexcitation is then supposed to lower this barrier. The Raman intensity of the defect-induced peaks can, independently of the details of the activation mechanism, be assumed to be a measure of fragmentation in the Cu-O chain plane of $\text{RBa}_2\text{Cu}_3\text{O}_{7-\delta}$, while the transport properties are connected to the average chain length. Therefore, we monitor the number of chain fragments of various length during a reordering process towards superstructure formation for comparison.

We use the description of the anisotropic chain plane interactions in $\text{YBa}_2\text{Cu}_3\text{O}_{6.7}$ in the 2D “Asymmetric next nearest neighbor model” (ASYNNNI) as developed by Andersen *et al.* in Ref. [24]. They were able to model the static structural phase diagram including the ortho-III phase with a set of four parameters. Though there has been much work on a more detailed description which includes higher order phases, ortho-III is probably the dominant case for our experimental

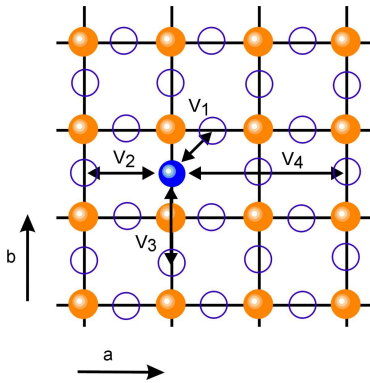


Figure 3.1: Part of the Cu-O-chain plane of a high- T_c superconductor of the $\text{RBa}_2\text{Cu}_3\text{O}_{7-\delta}$ type. Full orange symbols represent Cu, full blue symbols represent O, open blue circles indicate possible sites for neighboring oxygen atoms, and the arrows indicate the interaction parameters for four inequivalent neighboring positions, as used in Ref. [24].

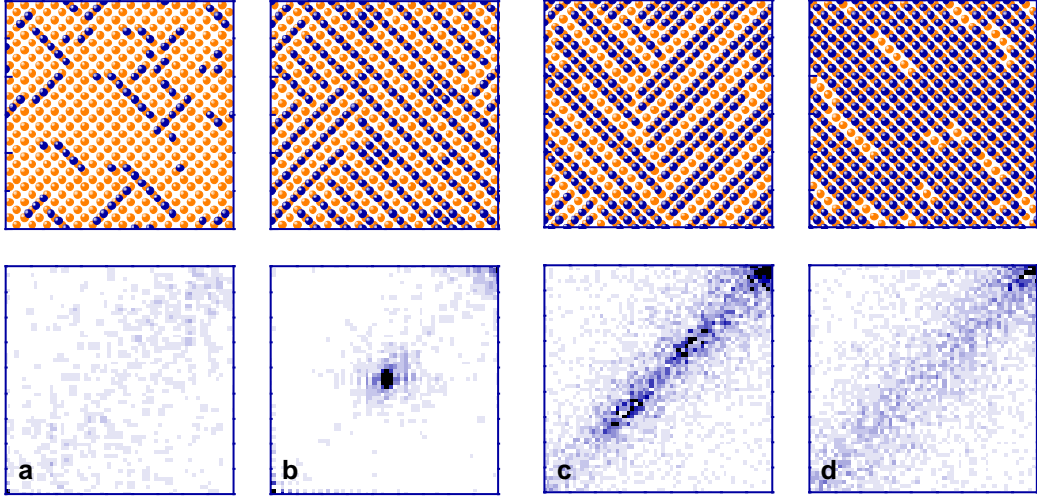


Figure 3.2: Upper row: Part of simulated Cu-O chain planes of size m^2 , $m=120$, after 10^4 MC steps/site for various concentrations of oxygen atoms (blue symbols) in the copper grid (orange symbols), from different parts of the structural phase diagram. Lower row: One quadrant of their Fourier transformations, corresponding to one twin direction, is shown to illustrate their regularity. Zero reciprocal lattice vector is at the lower left, the maximum at the upper right corner of the plots. The crystallographic axes a and b run along the diagonals. (a) $\delta=0.80$, $T=370 \cdot 10^{-3} V_1/k_B$, tetragonal phase, (b) $\delta=0.50$, $T=95 \cdot 10^{-3} V_1/k_B$, ortho-II-phase, (c) $\delta=0.33$, $T=55 \cdot 10^{-3} V_1/k_B$, ortho-III-phase, (d) $\delta=0.15$, $T=90 \cdot 10^{-3} V_1/k_B$, ortho-I-phase.

oxygen concentrations, allowing us to opt for a basic approach, which still contains all of the physical concept.

The next-nearest neighbor interaction energies for four sites relative to an oxygen position are defined in Fig. 3.1. It represents part of a Cu-O-chain plane in an Y123-crystal structure, with the full, orange circles marking the positions of Cu1 atoms at the four corners of a unit cell and the open, blue circles representing possible oxygen atom sites. In all simulations presented here we use the values for the interaction parameters V_i as obtained by Andersen *et al.* in their simulation of the experimental phase diagram of $YBa_2Cu_3O_{7-\delta}$: $V_1/k_B = 5430$ K, $V_2 = -0.36 \cdot V_1$, $V_3 = 0.12 \cdot V_1$, and $V_4 = 0.04 \cdot V_1$. [24] All interaction energies except for the one favoring chain connections across Cu-atoms are repulsive, being strongest for the smallest distance on sites in a and b direction in the same unit cell. The resulting summation of interaction energy terms gives:

$$\begin{aligned}
 E = & -V_1 \sum_{(r,r')} \sigma(r)\sigma(r') - V_2 \sum_{(r,r')} \sigma(r)\sigma(r') \\
 & -V_3 \sum_{(r,r')} \sigma(r)\sigma(r') - V_4 \sum_{(r,r')} \sigma(r)\sigma(r'), \quad (3.1)
 \end{aligned}$$

with $\sigma(r)$ and $\sigma(r')$ being one for occupied sites and zero otherwise, and the sum running up to the number of nearest and next-nearest neighbor sites, as defined in Fig. 3.1(a). We used a 120×120 oxygen site matrix with periodic boundary conditions in simulations presented along

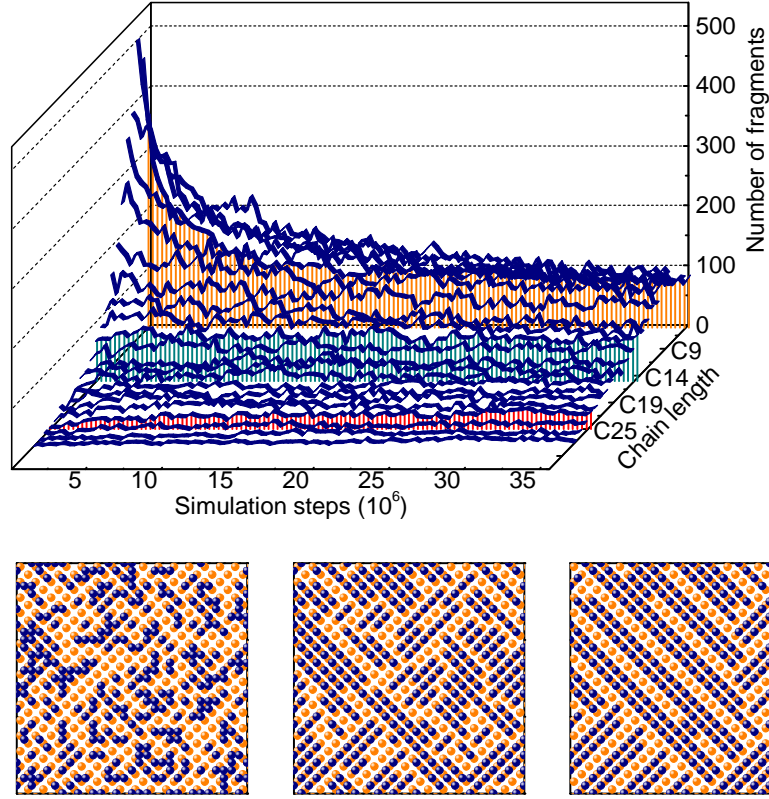


Figure 3.3: Development of the chain fragment numbers in a simulation with $\delta=0.33$ and $T=55 \cdot 10^{-3}V_1/k_B$ versus chain fragment length and simulation steps. Short chain fragment numbers decrease rapidly (orange drop lines), intermediate length remain constant due to the inflow from shorter, and the outflow to longer fragments (cyan drop lines), and long fragments increase slowly (red drop lines). The lower panels show snapshots of the plane at 1000, $5 \cdot 10^4$, and $5 \cdot 10^7$ MC steps.

with temperature-dependent Raman bleaching in Chap. 5, and a 1200×1200 for comparison to the Raman-and-transport experiment in Chap. 6. The simulations started with a randomly chosen configuration, which was annealed to equilibrium at $180 \cdot 10^{-3}V_1/k_B$ simulation temperature. After annealing, it was quenched to the temperature of interest and left for $3 \cdot 10^7$ to $5 \cdot 10^9$ Monte-Carlo steps for the entire ensemble. We give the temperature in units of the strongest interaction energy V_1 , since it sets the scale for the temperature dependence (as a reference, $100 \cdot 10^{-3}V_1/k_B = 543\text{K}$ for V_1 chosen as in Ref. [24]).

The original simulation as well as our setup yield the superstructure patterns, as seen from the real space and fast Fourier transform (FFT) plots in Fig. 3.2. Randomly distributed fragments in the tetragonal phase [3.2(a)] are opposed to orthorhombic patterns at higher oxygen occupation [ortho-II, ortho-III and ortho-I in 3.2(b),(c), and (d), respectively] with the corresponding peaks in the reciprocal lattice space. For all phases twinning can occur. We see such a twinning in Fig.

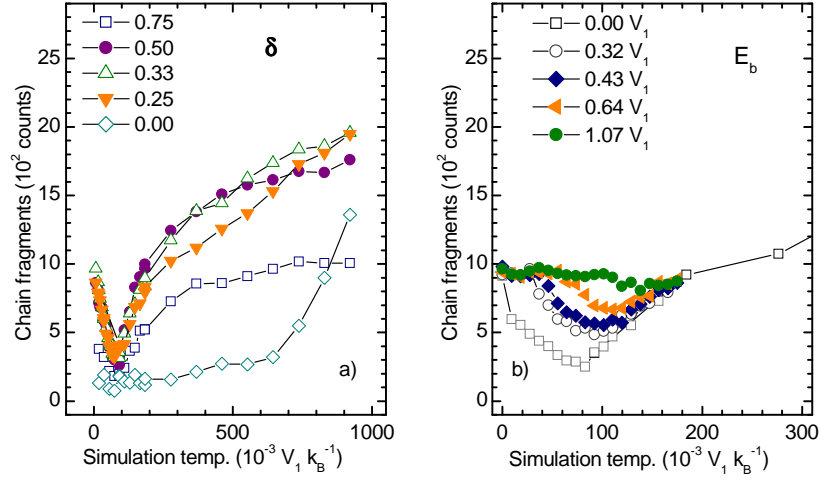


Figure 3.4: Total number of fragments in the simulation after equilibration for variable parameters. (a) Different oxygen concentrations, $\delta=0$ refers to zero oxygen deficiency, $\delta=1$ to an empty lattice. (b) Different energy barriers. The superstructure ordering lowers the fragment numbers and the total energy below $150 \cdot 10^{-3} V_1 / k_B$

3.2(c) with the domain boundary running vertically through the middle of the panel, while the phase shown in 3.2(d) is untwinned. The Cu-O chain-direction defines which axis is referred to as the b -axis of a domain. The crystal's a and b axes run diagonally in our simulation pictures of Fig. 3.2 for technical reasons.

In addition to the static model setup, Kawasaki dynamics is chosen to model the movement of oxygen atoms in the planes: In a Metropolis step an oxygen atom can change to a nearest neighbor site (corresponding to a V_1 relative position in Fig. 3.1), or to a next nearest neighbor position corresponding to the V_3 direction. The two kinds of jumps are treated identically and the total number of oxygen atoms in a simulation is constant.

Figure 3.3 shows the development of an oxygen simulation matrix in the course of the simulation. The panels represent snapshots of the matrix at different stages. Right after the start, the distribution is quite random for the chosen annealing temperature. Some steps into the process, the fragments built short chains without much interchain regularity, resembling diluted ortho-I isles, but at the end of the simulation, an ortho-III pattern with a twin boundary has evolved. In the same process, the distribution of chain length also shown in Fig. 3.3 has changed accordingly, from a narrow curve dominated by short fragments to a broader form, when the majority of the oxygen atoms is incorporated in chains.

Figure 3.4(a) shows the number of fragments at the end of a simulation for various oxygen fillings of the lattice versus simulation temperature. All chains are counted here, independent of direction or length. This includes “single” oxygen atoms, because they constitute a structure with

a defined direction in the plane together with the neighboring coppers. The number of fragments is related to the number of atoms in the matrix as well as to the degree of chain-formation. At temperatures comparable to the interaction energies, the latter process is dominant. Consequently, the lowest fragment numbers are found for a filled lattice, where chain formation is almost perfect up to temperatures of the order of V_1/k_B . There the chains disintegrate and the number of fragments rises quickly. For oxygen reduced lattices, the fragmentation is high because short chains exist statistically distributed. When temperatures get low enough, the smaller interactions $V_{2,3,4}$ set in and superstructure patterns develop, lengthening the fragments and decreasing further their number. For very low simulation temperatures, we encounter thermal freeze out. As a result, equilibrium is not reached within the simulation time and the number of fragments remains high below $70 \cdot 10^{-3} V_1/k_B$. Pattern building and freeze out in the simulations thus restrict the temperature range for comparison with experiment.

To account for the metastable photoexcitation state, a tunable frozen state is needed in the model. It is introduced as an energy barrier E_B , which has to be overcome in a site-change. Effectively, the barrier reduces the oxygen hopping rate by a value which depends only on temperature. Figure 3.4(b) shows how increasing E_B pushes the freeze-out point towards higher temperatures. We chose a value of $0.32 V_1$, matching the interaction parameters, to ensure that temperatures for which equilibrium is reached overlap with temperatures of superstructure-pattern development. The experiment suggests that the energy barrier under illumination should be significantly smaller. In a first approximation, we take it to be zero. Illumination is then simply modelled as a reduction of the barrier to zero for all oxygen atoms considered for a site change.

We summarize here the assumptions for the model: The Raman intensity of the defect-induced peaks is taken as a measure of chain fragments in the Cu-O chain plane of $\text{YBa}_2\text{Cu}_3\text{O}_{7-\delta}$, while the transport properties are connected to the average chain length. Light excitation enables reordering of oxygen vacancies within the chain plane at low temperatures, analogous to the thermally activated effect observed at higher (room) temperature. As in persistent photoconductivity relaxation, an energy barrier is associated with the thermally activated recovery process. [49, 50] Therefore, an energy barrier is introduced in the simulations, resulting in “frozen disorder” when the simulation is quenched from high temperatures. Illumination triggers further reordering at low temperatures by disabling that barrier. The dynamics is chosen to model the movement of oxygen atoms in the planes (Kawasaki dynamics): In a Metropolis step an oxygen atom can change to a nearest neighbor site, or to a next nearest neighbor position. The two kinds of jumps are treated identically and the total number of oxygen atoms in a simulation is constant. The fragment number is then monitored and compared for different temperatures, or different chain-fragment length, during the simulation, showing the development from a frozen-in disordered state towards the equilibrium state. Analogous to the dynamics in glassy materials, the latter is not reached at lowest temperatures.

Photo-induced effects on the dielectric function

A wealth of information on the dielectric function of the cuprates is available from reflectivity or ellipsometry experiments. [68–75] They were done mostly focussing on changes upon the opening of the superconducting gap at low temperatures, or on the properties of the pseudo-gap, [76] and the carrier dynamics [74] and, therefore, frequently focus on the infrared range. As cuprates are layered structures, many studies of anisotropy concern the difference between electronic and optical properties in the plane and perpendicular to the plane.

Our study, in contrast, is concerned with the in-plane anisotropy of orthorhombic, oxygen-reduced $\text{YBa}_2\text{Cu}_3\text{O}_{7-\delta}$ along the a and the b axes, and with the energy range of visible light from the near infrared (1.5 eV) to the ultraviolet (5.5 eV). Apart from the fact that reflectivity anisotropy is large enough to be seen by bare eye in samples with large twin domains, our interest was motivated by the persistent photo-induced effects found by other methods. The spectral efficiency of persistent photoconductivity shows an onset of illumination-induced resistivity change above 1.9 eV, low efficiency in the near UV, but a peak around 4 eV, defining our energy range of interest. In the Raman spectra of oxygen-deficient single crystals, the photo-sensitive modes resonant around 2.2 eV display sharply anisotropic intensities. As oxygen vacancy reordering must affect the orthorhombicity of the sample, effects in other material properties connected to the in-plane anisotropy are expected.

Ellipsometry is the usual method of choice for the measurement of the dielectric function. The similar method used here, Reflectance Anisotropy Spectroscopy (RAS), does not determine the absolute dielectric function, but is sensitive to its difference in two directions. Taking advantage of its sensitivity, we investigated detwinned single crystals of oxygen deficient $\text{YBa}_2\text{Cu}_3\text{O}_{7-\delta}$. We find well-resolved RAS peaks at 2.2 eV and above 4 eV, which are specific to the oxygen-deficient, underdoped compounds, and which indeed change under illumination in the slow, reversible way typical for persistent photo-induced effects. Thus, there is a link to the electronic anisotropy in the ab -plane induced by oxygen vacancy defect sites.

In order to connect our results to the research about the (absolute) dielectric function, we first deduce the reflectance anisotropy from exemplary literature data. After a brief introduction to the RAS method we show our experimental results. On the base of LDA calculations reported in the literature, and of a cluster model calculation on short chain-fragments, we are able to assign the RAS peaks to transitions involving the chain CuI atoms. This allows us to discuss the persistent photo-induced effects observed in RAS directly within the oxygen-vacancy reordering model.

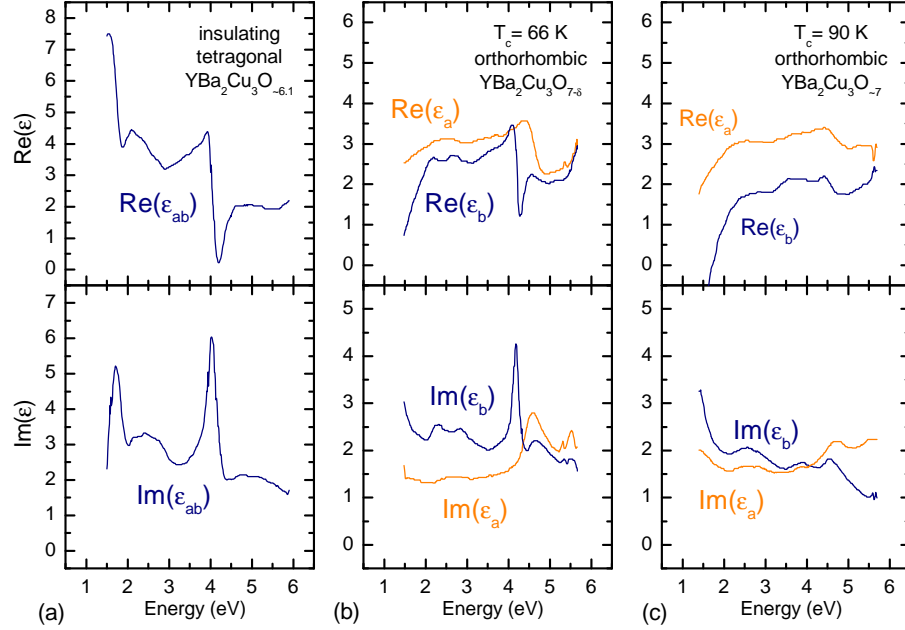


Figure 4.1: The dielectric function in the ab -plane in (a) an insulating, (b) an oxygen-reduced ($T_c = 66$ K) and (c) a fully oxygenated ($T_c = 90$ K) sample of $\text{YBa}_2\text{Cu}_3\text{O}_{7-\delta}$ deduced from ellipsometry by Kotz *et al.* [77]. The superconducting, orthorhombic crystals were detwinned and the dielectric function was determined separately for a and b .

4.1 The dielectric function of $\text{YBa}_2\text{Cu}_3\text{O}_{7-\delta}$

Figure 4.1 shows the dielectric function in the ab -plane measured with ellipsometry by Kotz *et al.* in Ref. [77]. The real part of this complex quantity is displayed in the upper panels, the imaginary part in the lower panels. Three samples of $\text{YBa}_2\text{Cu}_3\text{O}_{7-\delta}$ with different oxygen content were investigated. The data in (a) is taken from an insulating sample with approximate oxygen content 6.1, which is tetragonal and consequently identical in a and b . (b) and (c) are superconducting, orthorhombic samples, where a and b were determined separately and depicted as orange and blue lines, respectively. The dielectric function in c direction was also determined but is not shown here. The oxygen content is given in terms of superconducting critical temperature only, with $T_c=66$ K putting the sample in (b) in the oxygen-deficient range at the plateau roughly between 6.60 and 6.75, and $T_c=90$ K indicating near-optimal doping close to full oxygenation 7.0. From the dielectric function we calculated some useful quantities for practical purposes, such as the absolute magnitude of the normal-incidence reflectivity R_m , the penetration depth $1/\alpha_m$ and the

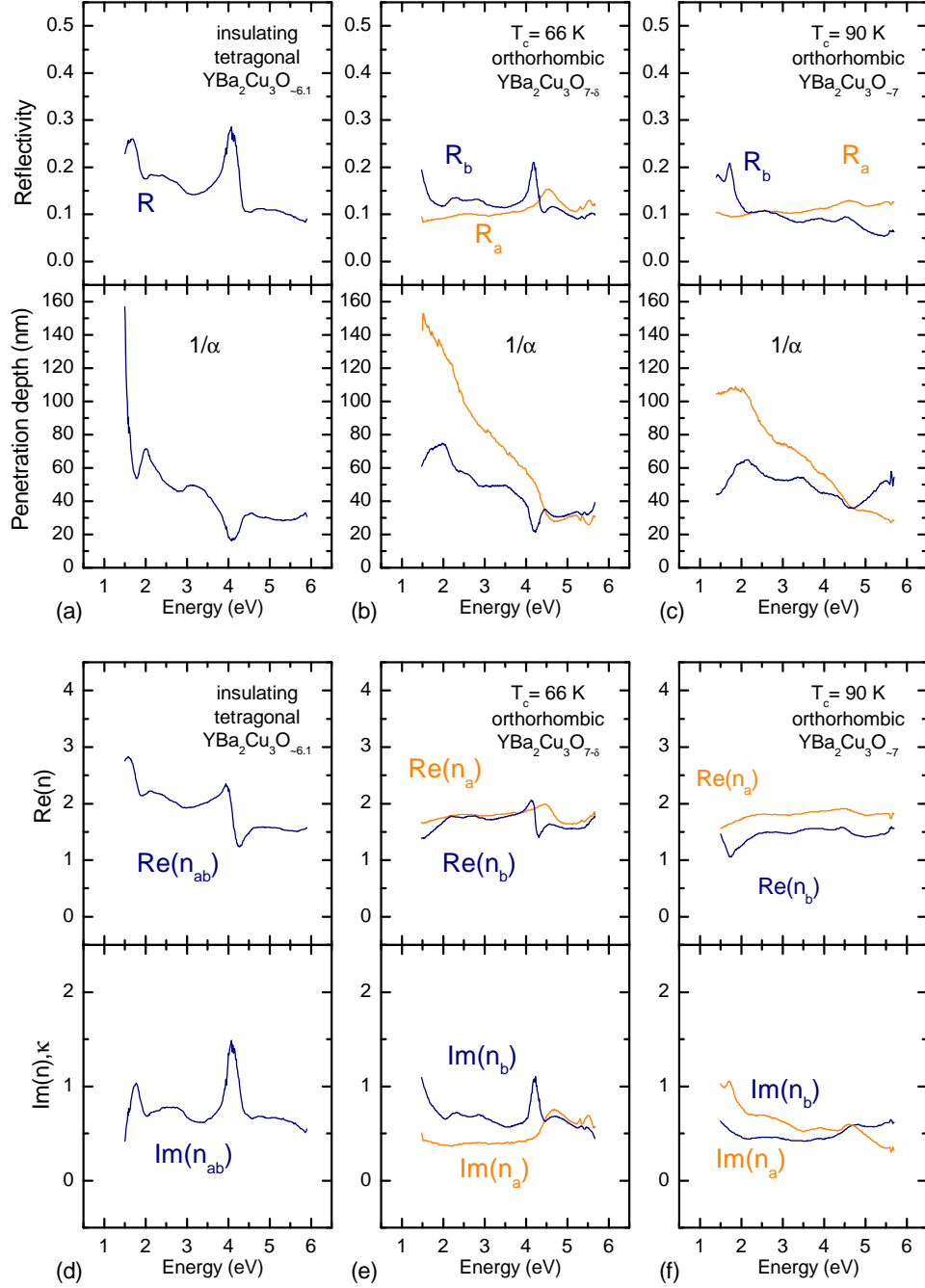


Figure 4.2: (a) to (c) normal incidence reflectivity and penetration depth $1/\alpha$, (d) to (f) complex refractive index deduced from the data in Fig. 4.1

refractive index n_m with $m = a, b$, or ab according to:

$$\epsilon_m = \epsilon_{1,m} + i\epsilon_{2,m} \quad (4.1)$$

$$n_m = n_{1,m} + in_{2,m} = \sqrt{\epsilon_m} \quad (4.2)$$

$$R_m = \left| \frac{n_m - 1}{n_m + 1} \right|^2 \quad (4.3)$$

$$\frac{1}{\alpha_m} = \frac{h \cdot c}{4\pi \cdot eE \cdot \text{Im}[\sqrt{\epsilon_m}]}, \quad (4.4)$$

where e is the elementary charge, h Planck's constant in [Js], c the speed of light, and E the energy in [eV]. The results are plotted in Fig. 4.2. The real part of the index of refraction is low, at around 2. Between 10 and 20% of the light is reflected at normal incidence, and the remaining intensity drops to a value of $1/e$ after propagating in the sample for roughly 100 nm, which is only a fraction of the wavelength in the visible. In the insulating sample the penetration depth is high at low energies, where the absorption drops quickly. The orthorhombic samples display metallic behavior, with reflectivity rising to near 100% at around 1 eV (not shown here, see, for example, Ref. [71]). The onset of the rise is at lower energy for the a -direction than for b , causing a large in-plane anisotropy in the infrared range. It has been verified in reflectance spectroscopy and used to distinguish the charge contributions from planes and chains. [72, 78]

The most prominent feature apparent in all quantities presented is the resonance at 4 eV. It is particularly strong in the tetragonal, insulating compound. Figure 4.3 shows its dependence on oxygen content, which was measured in a twinned sample. It weakens and shifts to slightly higher energy with increasing oxygen content. Along with the onset of superconductivity and the transition to the orthorhombic phase at 6.48, a second, weaker peak appears at higher energy. Both peaks can be traced to quite high oxygen content, but vanish in the fully oxygenated compound.

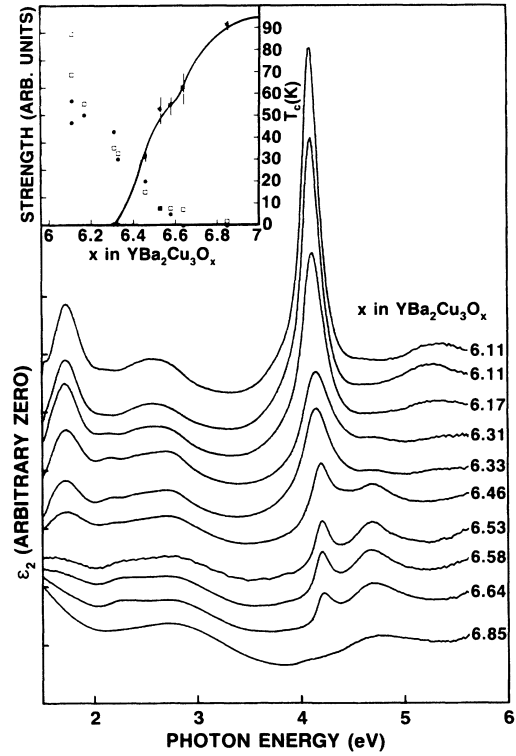


Figure 4.3: ϵ_2 determined with ellipsometry as a function of oxygen content in $\text{YBa}_2\text{Cu}_3\text{O}_{7-\delta}$ from Ref. [70]. The spectra are offset by a constant amount. In the inset, open squares correspond to the strength of the 4 eV peak, full circles to that of the 1.7 eV peak.

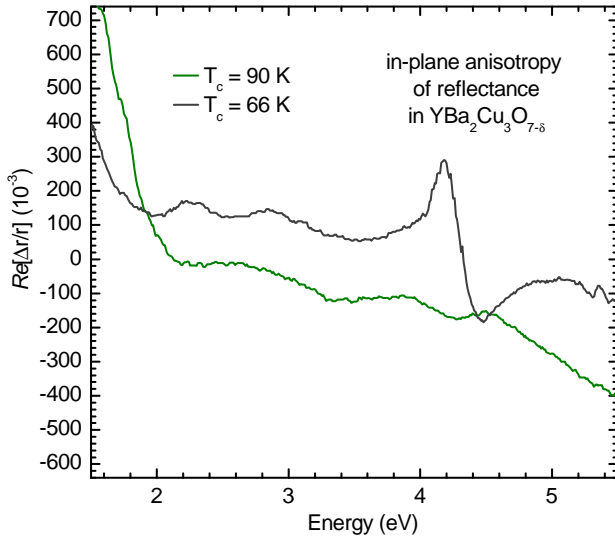


Figure 4.4: The ab , in-plane anisotropy of the reflectivity deduced from the dielectric function data in Fig. 4.1 for the underdoped and the fully oxygenated superconducting samples. In the infrared, the anisotropy is stronger for the more orthorhombic sample with higher carrier concentration. On the other hand, in the underdoped specimen the 4 eV resonance known from the insulating parent compound is strong and different in a and b direction in the orthorhombic environment.

[69, 70] Turning back to the untwinned samples in Figs. 4.1 and 4.2, it is clear that a splitting of the 4 eV feature occurs along the in-plane directions, with the lower energy part in the b direction and the higher energy part in a .

According to Ref. [79], the 4 eV resonance is due to an intraionic electron transfer of $Cu3d_{3z^2-1} \rightarrow Cu4p_x$ in the Cu atoms of the chain-plane, with some contribution of a transfer from $Cu3d_{3z^2-1} \rightarrow Ba$. The assignment was based on LDA calculations for the insulating parent compound, where the chain Cu atoms have no neighboring oxygen atoms in the plane, but two neighboring apical oxygen atoms in c -direction. We will refer to this configuration as *two-fold coordinated*. Though it is not clear if it can be transferred to the orthorhombic compounds unaltered, it is reasonable to assume that two-fold coordinated chain Cu atoms exist in decreasing numbers until all vacancies are filled up in the fully oxygenated compounds, matching the observed decrease of intensity versus increasing oxygen content. The splitting is taken to be a consequence of the orthorhombic crystal field, pushing the resonance to higher energies in the direction of the shorter a axis.

Kircher *et al.* [71] have shown that the 4 eV resonance increases in strength during thermal annealing of underdoped compounds along with the critical temperature of the sample, indicating that the number of two-fold coordinated CuI atoms increases upon superstructure development. Similarly, the large infrared anisotropy was studied during thermal annealing and found to reflect a change in carrier density upon oxygen reordering. [78] We will discuss the consequences of vacancy reordering in connection to photo-induced vacancy reordering at the end of this chapter.

In order to compare to the reflectance anisotropy spectroscopy data later, we use the dielectric function from Ref. [77] and Fig. 4.1 to calculate the real part of the complex reflectance anisotropy

$\text{Re}\left(\frac{\Delta r}{r}\right)$ according to

$$r_m = \frac{n_m - 1}{n_m + 1}, \quad m = a, b \quad (4.5)$$

$$\text{Re}\left(\frac{\Delta r}{r}\right) = \text{Re}\left(\frac{r_b - r_a}{\frac{1}{2}(r_b + r_a)}\right) \quad (4.6)$$

$$= \text{Re}\left(\frac{\epsilon_b - \epsilon_a}{\left(\frac{\epsilon_b + \epsilon_a}{2} - 1\right) \cdot \sqrt{\frac{\epsilon_b + \epsilon_a}{2}}}\right). \quad (4.7)$$

The result is plotted in Fig. 4.4 for the two orthorhombic compounds. On the scale of the plot, this quantity will be plus $2000 \cdot 10^{-3}$ if all reflected intensity comes from the b direction and none from a , and minus $2000 \cdot 10^{-3}$ viceversa. In the fully oxygenated sample (green line) the anisotropy rises sharply at the infrared end of the spectrum and is largely flat otherwise. In the underdoped compound, the onset of anisotropy is shifted to lower energies. Additionally, the b -polarized part of the 4 eV resonance shows up as a peak, and the broader a -polarized part as a dip. The weaker peak around 2.2 eV also appears exclusively in the underdoped compound. It originates from a peak in the b -component of the dielectric function, which is completely absent in a -direction.

4.2 Reflectance anisotropy spectroscopy - principle and experimental setup

The reflectance anisotropy measurements were performed on the broad-range RAS setup in the group of Prof. Dr. W. Richter, TU Berlin, together with A. Bruchhausen, Centro Atómico Bariloche. Our samples of detwinned crystalline $\text{YBa}_2\text{Cu}_3\text{O}_{7-\delta}$ were provided by Prof. Dr. G. Nieva,

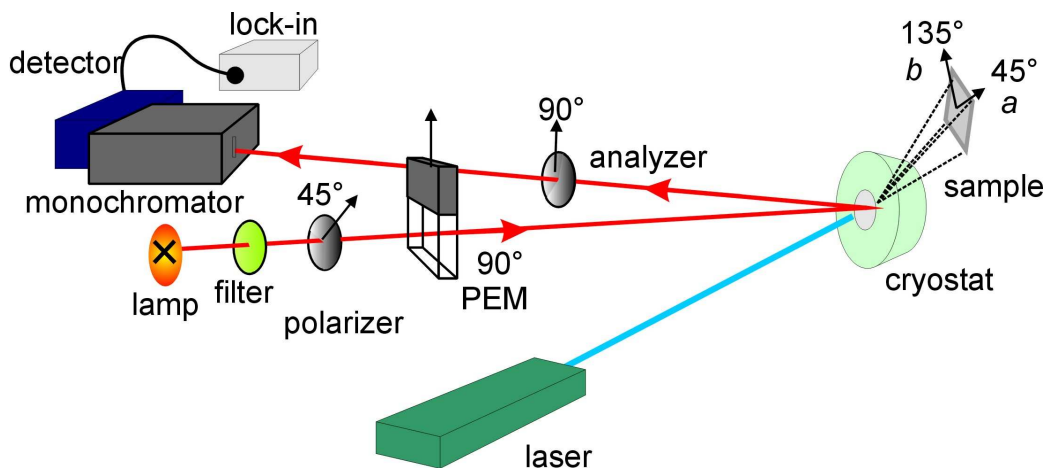


Figure 4.5: High-frequency modulation setup for the determination of the reflectance anisotropy within the surface plane of the sample at variable low temperature with additional illumination provided by a laser.

Centro Atómico Bariloche (see Appendix A). Details on the principle of measurement in RAS are found in Refs. [80–82] and references therein. Figure 4.5 shows a sketch of the RAS principle. A Xe-high-pressure lamp is used as white-light source to acquire spectra in the range from 1.5 to 5.5 eV. Its light is first polarized linearly and then modulated between two linear polarization states in orthogonal directions at 50 kHz with a photo-elastic modulator. Not shown is the convex mirror used to focus the light onto the ab sample surface in the temperature controlled He-flow micro-cryostat with a sapphire window. The reflected light is passed through the analyzing polarizer, which turns the polarization modulation into an intensity modulation. If the reflectances in the two directions, r_a and r_b are different, a change of the modulated signal will occur. The signal is dispersed by the monochromator, detected in a single channel and passed to a lock-in amplifier. A feature of the broad-range setup is that two sets of monochromators and detectors are available to cover a large spectral range: A Si-diode for the low energy part and a photomultiplier for the high energy part. The change of the detecting system causes a small discontinuity in the spectra at 3 eV. The acquisition of spectra is between 2 to 5 min, allowing *in situ* monitoring of the changes under additional illumination.

Other than in the case of the Raman experiments presented in Chap. 5, it is easy to separate the detection of spectra from the photoexcitation effects. We used a laser for additional illumination, either the 441 nm line of a HeCd Laser with a power density of 10 mW/mm², or the 632 nm line of a HeNe laser with 14 mW/mm². The power density coming from the Xe-lamp is two to three orders of magnitude lower on the sample surface.

In order to trace the relation of the signal detected by the lock-in amplifier to the reflectance anisotropy of the sample, the polarization modulation setup can be described in the Jones-matrix formalism, where each optical element transforming the polarization is represented in two dimensional matrix form. A polarizer Pol , the reflection of the sample Ref and the photoelastic modulator retardation $PEM(A)$ can be written as

$$Pol = \begin{pmatrix} 1 & 0 \\ 0 & 0 \end{pmatrix}, \quad Ref = \begin{pmatrix} r_a & 0 \\ 0 & r_b \end{pmatrix}, \quad PEM(A) = \begin{pmatrix} \exp(-i\frac{A}{2}) & 0 \\ 0 & \exp(i\frac{A}{2}) \end{pmatrix}, \quad (4.8)$$

where A is the amplitude of the phase retardation. This amplitude is modulated by the PEM at high frequency, in good approximation in sinusoidal form $A = A_0 \cdot \sin(\omega t)$. Each element is rotated to their angle ϕ to the horizontal in the setup using the rotation matrix $D(\phi)$

$$D(\phi) = \begin{pmatrix} \cos(\phi) & \sin(\phi) \\ -\sin(\phi) & \cos(\phi) \end{pmatrix}, \quad (4.9)$$

so that the full experimental setup T is given by the matrix multiplication

$$\begin{aligned} T(\alpha, \beta, \gamma, \delta, A) &= D^{-1}(\delta) Pol D(\delta) \cdot D^{-1}(\gamma) Ref D(\gamma) \cdot D^{-1}(\beta) PEM(A) D(\beta) \cdot D^{-1}(\alpha) Pol D(\alpha) \\ &= Pol(\delta) \cdot Ref(\gamma) \cdot PEM(A, \beta) \cdot Pol(\alpha) \end{aligned}$$

In our experimental setup the angles of the polarizers, the PEM and the sample are (see Fig. 4.5) $\alpha = 45^\circ$, $\beta = 90^\circ$, $\gamma = 45^\circ$, and $\delta = 90^\circ$, respectively. Sending light with the incident electrical field V_{in} polarized along the first polarizer direction through this configuration yields an electrical field vector V_r with intensity $I = V_r \cdot V_r^*$

$$\begin{aligned} V_r &= T(\alpha, \beta, \gamma, \delta, A) \cdot V_{in} \\ &= \begin{pmatrix} 0 \\ -\frac{1}{2\sqrt{2}} \exp(i\frac{A}{2})(r_a(1 + \exp(iA)) + r_b(1 - \exp(iA))) \end{pmatrix} \\ V_r \cdot V_r^* &= \frac{1}{8}(r_{a,2}^2 + r_{a,1}^2 + r_{b,2}^2 + r_{b,1}^2 + (r_{a,2}^2 + r_{a,1}^2 - r_{b,2}^2 - r_{b,1}^2) \cos[A_0 \cdot \sin(\omega t)] \\ &\quad + 2(r_{a,1}r_{b,2} - r_{a,2}r_{b,1}) \sin[A_0 \cdot \sin(\omega t)]) \end{aligned} \quad (4.10)$$

Aspnes *et al.* have used Bessel functions J of zero, first and second order to approximate the nested trigonometric functions, so that the modulated output intensity becomes [80, 81]

$$\begin{aligned} \frac{\Delta I}{I} &= 2\text{Im}\left(\frac{\Delta r}{r}\right) \cdot J_1(A_0) \cdot \sin(\omega t) \\ &\quad + 2\text{Re}\left(\frac{\Delta r}{r}\right) \cdot J_2(A_0) \cdot \cos(2\omega t) \end{aligned} \quad (4.11)$$

In this expression, $J_1(A_0)$ and $J_2(A_0)$ are constants which can be chosen for convenience via the magnitude of the photoelastic modulator vibration. Window strain and misalignments have been neglected, for the full expression see Refs. [80–82]. It turns out that the real and the imaginary part are modulated at different frequencies. In our setup, the second harmonic was detected by lock-in technique, yielding the real part of the reflectance difference.

4.3 The ab in-plane reflectance anisotropy of $\text{YBa}_2\text{Cu}_3\text{O}_{7-\delta}$

Figure 4.6 shows reflectance anisotropy spectra taken at room temperature from two detwinned single crystals with slightly different oxygen concentration, $\text{YBa}_2\text{Cu}_3\text{O}_{6.7}$ and $\text{YBa}_2\text{Cu}_3\text{O}_{6.65}$. For

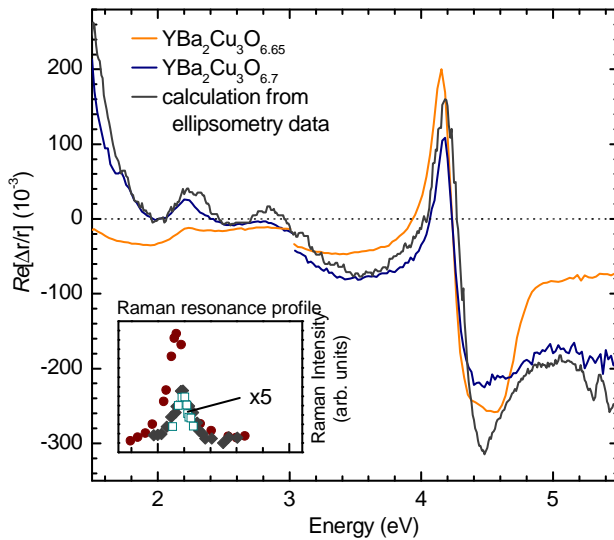


Figure 4.6: The ab , in-plane anisotropy of the reflectivity measured by RAS on two detwinned single crystals of $\text{YBa}_2\text{Cu}_3\text{O}_{6.7}$ and $\text{YBa}_2\text{Cu}_3\text{O}_{6.65}$. For comparison, the gray curve is the reflectance anisotropy deduced from the dielectric function reproduced from Fig. 4.4. It has been downshifted by 130 units. The discontinuity in the data at 3 eV occurs for technical reasons, upon detector change. [83, 84] For comparison, resonant Raman data is depicted in the inset on the same energy scale (from Wake *et al.*, [11] (multiplied by 5) and Käll *et al.*, [61]).

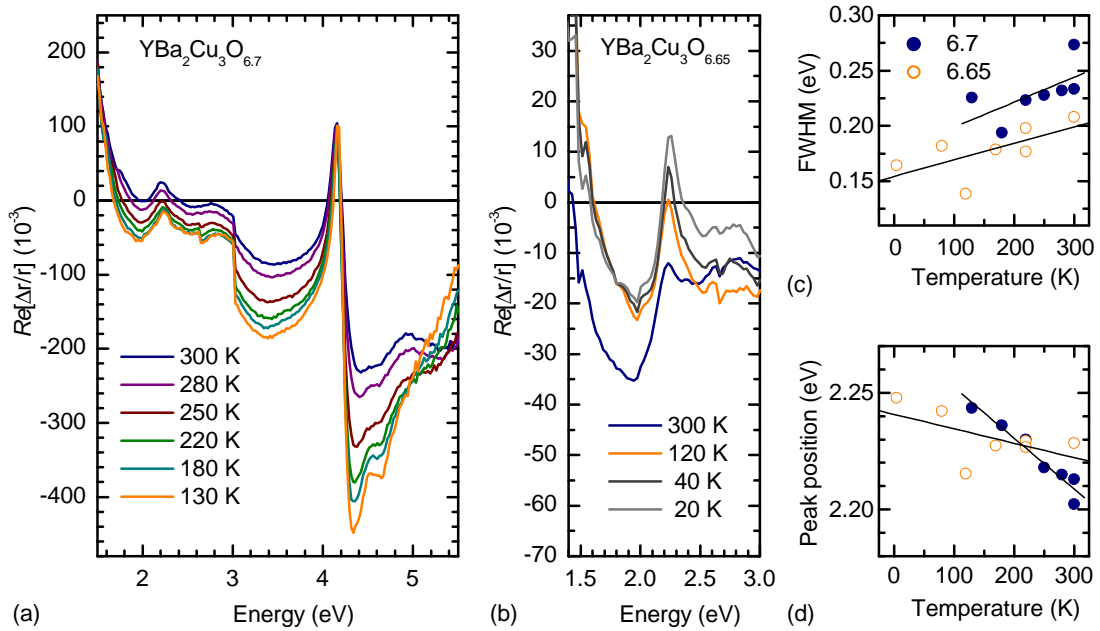


Figure 4.7: Temperature dependence of the ab , in-plane anisotropy of the reflectivity measured by RAS on two detwinned single crystals with slightly different oxygen content, (a) $\text{YBa}_2\text{Cu}_3\text{O}_{6.7}$, and (b) $\text{YBa}_2\text{Cu}_3\text{O}_{6.65}$. At low temperatures two features at 4.3 and 4.6 develop. (c) and (d) show the change in peaks position and width of the 2 eV resonance in the RAS spectra. [84]

comparison we also reproduce the curve calculated from the ellipsometric data for the underdoped sample. The match is excellent, thus validating the experiment and providing us with a clear link to the ellipsometry-based assignment of the 4 eV peak to an intraionic CuI transition. The peak is stronger in the sample with slightly lower oxygen content. This is expected, as it should have more two-fold coordinated CuI chain atoms hosting the transition. Likewise, its lower carrier concentration shifts the onset of the strong infrared anisotropy to lower energies. Despite of the small difference in oxygen concentration of 0.05, we know from X-ray measurements (see Chap. 7) that our samples have different superstructure ordering. $\text{O}_{6.65}$ shows ortho-II ordering, whereas the superstructure peak positions for the $\text{O}_{6.7}$ sample are consistent with the ortho-VIII phase suggested in Ref. [17]. The clear difference between the two spectra proves the sensitivity of RAS to oxygen content and configuration in this complex part of the phase diagram.

The peak at 2.2 eV, which comes from a b -polarized electronic resonance, is also well defined in the experimental data but has not been discussed in the literature before. To check for a possible assignment, a calculation based on the four-band Hubbard model has been performed by our collaboration partner Prof. Dr. A. Aligia, Centro Atómico Bariloche, Argentina. The details can be found in Refs. [40, 83]. The smallest unit modelling a “monomer” chain fragment is a Cu_2O_5 cluster, with two chain Cu atoms, one chain oxygen atom between them and the four nearest apical oxygen neighbors. With parameters chosen according to previous model calculations

on the $\text{YBa}_2\text{Cu}_3\text{O}_{7-\delta}$ system, the lowest transition in the cluster is found at 2.5 eV, with small variations in the parameters causing shifts of ± 0.5 eV. It is dipole-allowed for polarization of the electric field along b . In a longer chain containing three chain oxygen atoms, the same transition is found at 1.9 eV, indicating that it red-shifts quickly in longer chains. From a strong sensitivity to a configurational change on the chain ends it was concluded that it is connected to the open chain ends. As seen in Fig. 4.4, the fully oxygenated system does not show any transition in that energy range. From these facts we interpret the 2.2 eV peak as a resonance involving electronic states of a three-fold coordinated CuI atom at the end of a short chain fragment. This explains naturally that the transition occurs exclusively in one direction in the plane and only in the underdoped material.

We note also the connection to the resonance profile of the defect-induced Raman modes, which are strong under excitation energies close to 2.2 eV. The inset of Fig. 4.6 displays literature data of the Raman resonance profile taken from Wake *et al.* [11] (300 and 100 K, $\delta \approx 0$) and Käll *et al.* [61] (room temperature, $\delta \approx 0.23$). Centered at 2.18 and 2.15 eV and with a width of 160 meV it is similar, though not identical to the dielectric RAS peak. This finding points to a common origin of the two signals, with the electronic transition as a possible explanation for the activation of the Raman modes. Motivated by this agreement, we searched for defect-induced Raman modes under UV excitation, and indeed found a very strong resonance matching the 4 eV anisotropic peak in the dielectric function. As will be discussed in detail in the chapter on Raman scattering (Chap. 5), there is much evidence for a close connection between the electronic anisotropy, the activation of Raman modes and oxygen vacancy reordering.

Thinking of the metastability of persistent photo-induced effects at low temperatures, we were interested in the RAS response on cooling. Figure 4.7 shows spectra between 130 and 300 K taken from the $\text{YBa}_2\text{Cu}_3\text{O}_{6.7}$ crystal in (a), and the low-energy part for the $\text{YBa}_2\text{Cu}_3\text{O}_{6.65}$ crystal to temperatures as low as 20 K in (b). The most striking effect upon cooling is the shift of spectral weight from high to low energies that has been reported in DC reflectance measurements and ellipsometry before. [75] The reflection from the sample visibly red-shifted and darkened due to the loss of reflectivity in the visible range, leading to experimental difficulties when the signal dropped below the sensitivity level of the setup. Two separate, negative RAS peaks at 4.3 and 4.6 eV develop from the one at room temperature at 4.4 eV, and the overall anisotropy increases. The RAS peak at 2.2 eV was fitted using a Lorentzian lineshape. Figure 4.7(c) and (d) show its sharpening and its slight shift in position towards higher energies at low temperatures. The change in width of 20 % between 100 and 300 K matches the sharpening of the Raman resonance observed by Wake *et al.* as depicted in Fig. 4.6. [11]

4.4 Photo-induced effects in reflectance anisotropy

Under illumination with an additional light source, the reflectance anisotropy shows a well defined change which is almost exclusively confined to the two peaks at 2.2 and 4 eV under discussion.

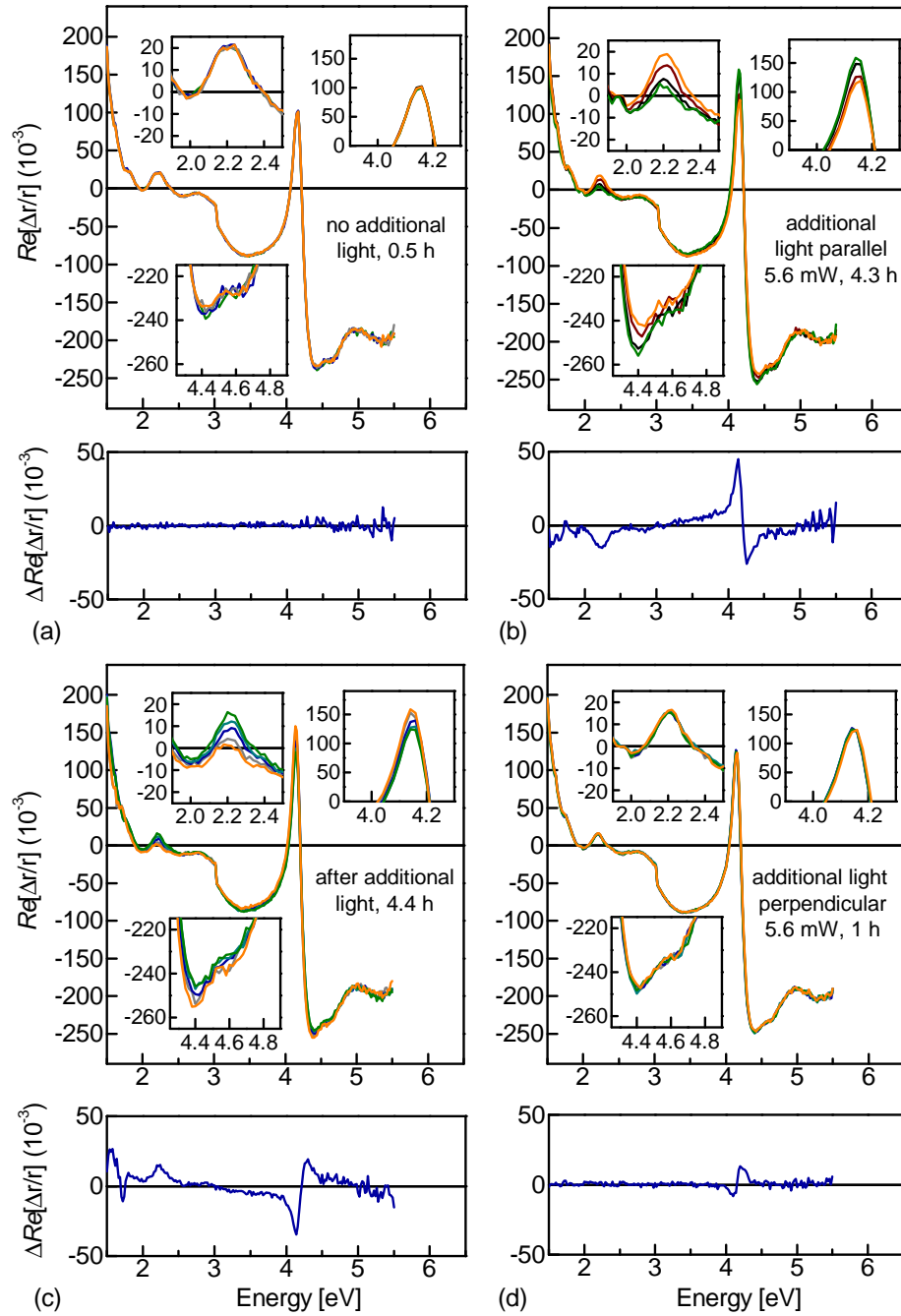


Figure 4.8: Change upon illumination in the RAS spectra of $\text{YBa}_2\text{Cu}_3\text{O}_{6.7}$ at 300 K using the 632 nm line of a HeNe laser. Orange lines depict the first, green lines the last spectra in each sequence. (a) Stability without additional illumination. (b) Change during illumination with laser light polarization parallel to the chain direction b . (c) Recovery without additional light after illumination. (d) Illumination with polarization parallel to a . [83]

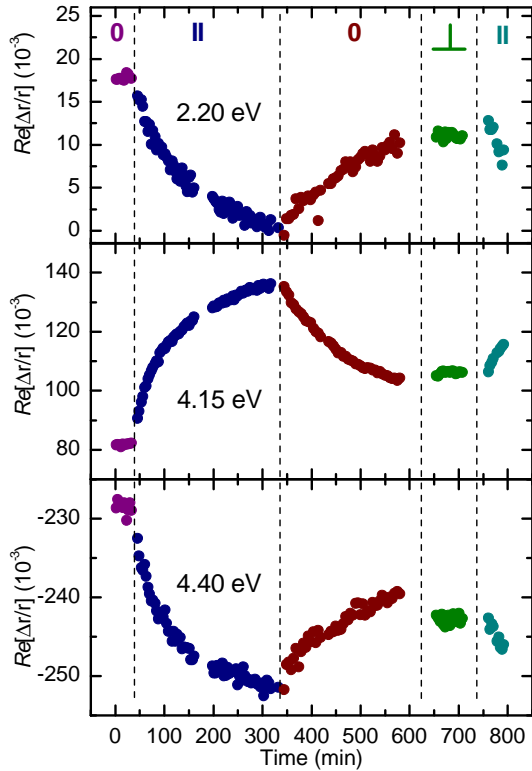


Figure 4.9: Change in the RAS spectra of $\text{YBa}_2\text{Cu}_3\text{O}_{6.7}$ at 300 K versus illumination time. The top panel shows RAS at 2.2 eV, the middle panel at 4.15 eV, and the lower panel at 4.4 eV. Stages marked 0 are without illumination, stages marked II have illumination of 5.6 mW polarized along b , the remaining stage the same illumination polarized along a . The RAS peaks decrease under illumination polarized parallel to the Cu-O chains in the ab -plane of $\text{YBa}_2\text{Cu}_3\text{O}_{6.7}$, recover in the dark during room temperature annealing, are unaffected by illumination polarized perpendicular to the chains, and the change can be reproduced by turning the polarization back along b . [83]

The sequential spectra in Fig. 4.8 illustrate an entire cycle of measurement. Each panel has selected spectra from a sequence, the first one is plotted in orange, the last in green. The three insets enlarge the ranges where photo-induced changes occur. Below each panel we show the last spectrum subtracted from the first one to illustrate the changes. In panel (a), prior to additional illumination, the spectra are stable. From the comparatively small power density caused by the Xe-lamp, no changes are expected from its illumination within laboratory time scale. With the laser light on in (b), the peak at 2.2 eV decreases. This is in analogy to the Raman bleaching modes resonant at the same energy. The peak at 4.15 eV increases, while the dip at 4.4 eV further decreases. With the match to the dielectric function, it is reasonable to assume that both peaks become more intense in their respective directions, creating greater anisotropy. The period of time shown is 4.3 h, so the RAS change matches the slow time scales of persistent photo-conductivity and Raman bleaching. After illumination, the relaxation of the effect can be observed at the same slow time scale (c). This is expected, since the experiment was carried out at room temperature. Like persistent photo-conductivity and Raman bleaching, the RAS effect is obviously reversible. Another interesting aspect is its polarization dependence as illustrated in panel (d): While the linear polarization of the laser light was previously aligned along b , it is here along a . For this configuration, the photo-induced change is almost absent, and the little change at 4 eV observed in the difference between first and last spectrum even points to ongoing relaxation according to its sign. The mechanism of oxygen vacancy reordering must thus be polarization dependent, supporting motion only for

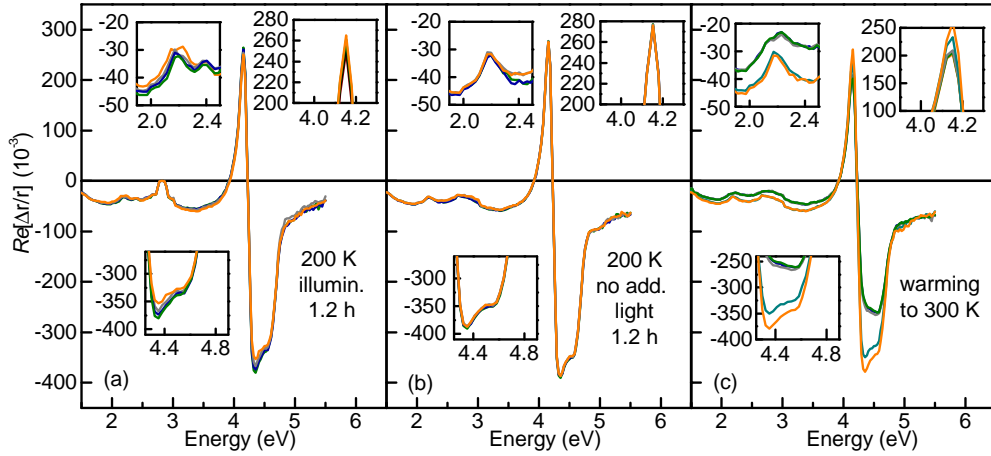


Figure 4.10: Sequential RAS spectra of $\text{YBa}_2\text{Cu}_3\text{O}_{6.7}$ at 200 K (a) Under additional illumination with the 441 nm (2.80 eV) line of a He-Cd laser, the spectra change mostly at 2.2 eV and ant 4.4 eV. (b) After illumination the change remains stable at 200 K. (c) Recovery upon heating to room temperature. [84]

excitation with polarization along the chains. This we have also shown for the case of Raman bleaching in a two-laser visible experiment, which is presented in Chap. 5. A more technical conclusion is that we can exclude heating as a possible cause for the effect. The anisotropy values at 2.2, 4.15 and 4.4 eV have been extracted from the spectra and are depicted versus illumination time in Fig. 4.9. They illustrate the opposite development for the decreasing peak in the visible and the increasing peaks in the UV, as well as the polarization dependence of the change and the recovery during room temperature annealing. Like those from Raman and transport experiments,

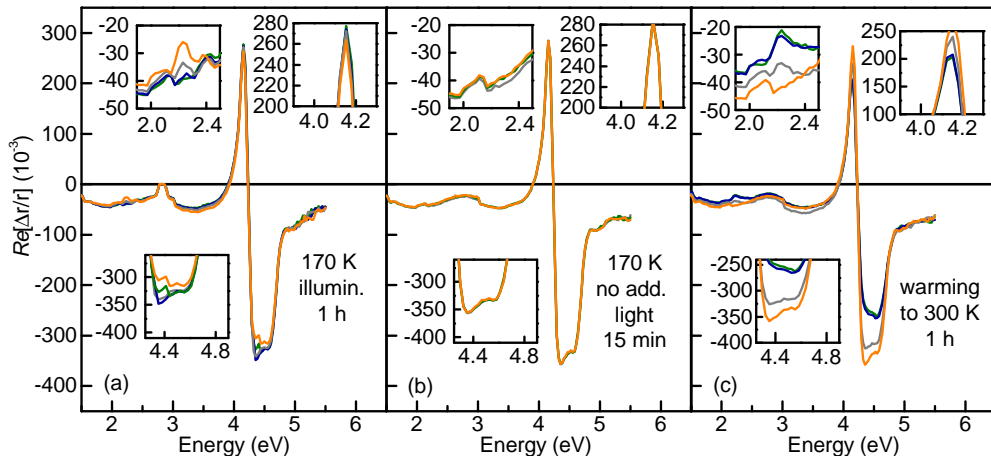


Figure 4.11: Sequential RAS spectra of $\text{YBa}_2\text{Cu}_3\text{O}_{6.65}$ at 170 K (a) Under additional illumination with the 441 nm (2.80 eV) line of a He-Cd laser, the spectra change mostly at 2.2 eV and 4.4 eV. (b) After illumination the change remains stable at 170 K. (c) Recovery upon heating to room temperature. [84]

the curves are well described by a stretched exponential functional form (see Eq. 5.14 in Chap. 5 and Chap. 6 for details).

The sequential experiments were repeated at low temperatures. Spectra taken at 200 K are shown in Fig. 4.10, those taken at 170 K in Fig. 4.11. Each figure shows in panel (a) a sequence during additional illumination, in panel (b) a sequence with the laser switched off after illumination (still at low temperature) and in panel (c) spectra taken during heating back up to room temperature. The most important results here are that the photo-induced change is not confined to the room temperature range and that it displays metastable behavior. In (a), essentially the same change occurs in the peaks as was observed under room-temperature illumination, although we note that the change in the UV resonance is restricted to the dip, leaving the 4.15 eV peak nearly unaffected. Within experimental observation times of 15 min and 1.2 h in (b), the RAS spectra were conserved at both 170 and 200 K. The relaxation process sets in upon warming in (c), superimposed to the considerable temperature-related changes in the spectra as seen also in Fig. 4.7. Both properties, the photo-induced changeability in a temperature range where thermal reordering is frozen, and the metastability after illumination, are shared by persistent photoconductivity and Raman bleaching.

We now turn to the discussion of the reflectance anisotropy results within the framework of the oxygen-vacancy reordering model. Based on the assignment of the 2.2 and 4 eV peaks discussed above, the interpretation of photo-induced change in the reflectance anisotropy is quite straightforward. The 2.2 eV peak is ascribed to a transition involving a CuI atom at the end of a short chain with three neighboring oxygen atoms, as was marked in green in Fig. 2.7 in Chap. 2. The 4 eV peaks are assigned to transitions in two-fold coordinated chain Cu atoms (blue mark). Cu atoms in the middle of a chain have four neighboring oxygen atoms altogether (red mark), and with the corresponding valence state they show neither of the two transitions. In the previous chapter, we have described the reordering of oxygen-vacancies in the chain plane into superstructures with alternating full and empty chains. As a consequence, the number of short fragments with three-fold coordinated Cu atoms decreases, while at the same time the number of four-fold and two-fold coordinated CuI increases. Upon reordering, the abundance of Cu atoms hosting the in-plane anisotropic transitions then causes the observed change in intensity. This picture is also supported by the results of Kircher *et al.* [71], who reported that the 4 eV resonance changes during oxygen-reordering at room temperature. From the fact that the photo-induced change is polarization-dependent we conclude that the movement of an oxygen atom is enabled by the absorption of the incoming photon, which enables the oxygen atom to overcome the energy barrier against hopping to an empty site between two Cu atoms.

4.5 Summary

In this chapter we presented the first experiments of reflectance anisotropy spectroscopy in the ab plane of $\text{YBa}_2\text{Cu}_3\text{O}_{7-\delta}$ under photoexcitation. We find peaks at 2.2 eV, 4.15 and 4.4 eV which change significantly under illumination. Like the persistent photo-induced effects detected with Raman spectroscopy and electrical transport experiments, the change occurs on a time scale of minutes to hours, is stable after illumination at low temperatures at least up to 200 K, but recovers during room-temperature annealing on the same time scale. We also observe that it occurs exclusively for polarization of the incident light along the chain direction b .

The peak at 2.2 eV is attributed to a resonance apparent in the dielectric function in b -direction, but absent in a . It nearly coincides with the resonance profile of defect-induced Raman modes with the same polarization selection rule with respect to its center energy, and both show the same relative sharpening upon cooling. Like the Raman intensity, it decreases under illumination. With the help of a Cu_2O_5 cluster calculation based on the Hubbard model, we assign this peak to a b -polarized, dipole-allowed transition in a three-fold oxygen-coordinated Cu atom at the end of a short chain fragment.

The peak at 4.15 eV and the negative peak at 4.4 eV are ascribed to intraionic transitions in two-fold oxygen-coordinated Cu atoms. Using data on the dielectric function from the literature to calculate the in-plane reflectance anisotropy signal, we can identify the RAS peak origin as the split-up 4 eV resonance, which is found in the insulating compound $\text{YBa}_2\text{Cu}_3\text{O}_6$. It weakens with increasing oxygen content and splits in energy along the b - (4.15 eV) and the a - (4.4 eV) direction in the orthorhombic, superconducting compounds. In the fully oxygenated samples it is absent. With the Raman results in Chap. 5, we will show a strong resonance of defect-induced modes which is connected to this peak.

Under illumination, the 2 eV peak decreases in intensity, while the absolute intensity of the 4.15 eV and the 4.4 eV peaks increases. With the above peak assignments, this provides support for the oxygen-vacancy reordering model, which gives a natural explanation for the observation. During superstructure development, the number of three-fold coordinated Cu atoms at the end of short fragments decreases, while at the same time the number of two-fold coordinated Cu atoms rises.

We conclude that the optical in-plane anisotropy in the visible and UV range is dominated by the oxygen vacancy sites, causing it to exceed the anisotropy in the – more orthorhombic – fully oxygenated compound. The change under illumination indicates an intimate link between the electronic transitions at vacancy defect sites, persistent photo-induced effects in Raman spectroscopy and electrical transport, and the reordering of vacancies which alters the distribution of chain Cu atoms with specific oxygen coordination numbers.

Reflectance anisotropy spectroscopy also proves to be very sensitive to the oxygen content and configuration in underdoped but orthorhombic, untwinned $\text{YBa}_2\text{Cu}_3\text{O}_{7-\delta}$. Since the excita-

tion of photo-induced effects can be separated from the excitation, it is a versatile tool for further investigations on persistent photo-induced effects, such as on the relaxation rates at different temperatures, or on the dependence on excitation energy in comparison to persistent photoconductivity. The intimate connection between structure and electronic anisotropy could also be used for an estimate of the chain-length variation, once the RAS signal is calibrated in a systematic oxygen-content study.

Raman spectroscopy on oxygen-deficient $\text{YBa}_2\text{Cu}_3\text{O}_{7-\delta}$

Inelastic light scattering provides experimental access to the vibrational properties of a solid, since the modulation of the electronic structure induced by the atomic motion can couple to the electric field of the incoming wave. Due to the nature of this coupling mechanism, information on the electronic structure itself is also an integral part of the signal. Together with its sensitivity to symmetry and direction, these properties make inelastic light scattering a particularly versatile tool.

This work reviews the persistent photo-induced effects in $\text{YBa}_2\text{Cu}_3\text{O}_{7-\delta}$ from the perspective of the oxygen reordering model, assuming a structural change in the compound. As was reviewed in Chap. 2, certain defect-induced Raman modes are known to respond to illumination. Raman spectroscopy was therefore an obvious choice for our purpose, and the chronological starting point for the investigation of photo-induced effects with other experimental techniques.

In the following we review the basic theoretical aspects of Raman scattering important in this context. We then proceed to the specific case of $\text{YBa}_2\text{Cu}_3\text{O}_{7-\delta}$, showing its symmetry properties and deduced selection rules. Calculated eigenvectors and phonon dispersions from the literature used for the assignment of peaks are followed by the information available on experimental frequencies. The experimental setups used are described briefly. Finally, we present our results on oxygen-vacancy activated modes and their change under illumination and compare their dynamics to results from the Monte-Carlo simulation explained in a previous chapter.

5.1 Raman scattering by phonons

The inelastic scattering of visible light from atomic vibrations is named *Raman effect* after the first author who reported its experimental observation some years after its theoretical prediction in the 1920ies. [85] Raman received the Nobel prize for his discovery in 1930, but only some 30 years later after the invention of the laser came its development towards a spectroscopical tool. The left panel in Fig. 5.1 shows a sketch of a typical modern Raman experiment. The light source sends an incident wave of frequency ω_i and wavevector k_i with the electrical field polarized along e_i onto the sample. Most of the light is reflected, absorbed or elastically scattered, but a small portion of the light undergoes a change in energy (and wavevector) during the scattering process. In the direction of choice for the detection, photons with ω_s and k_s arrive. An analyzer selects the portion which is polarized along e_s . A filter cuts the elastically scattered photons from the detection range, and a dispersive unit such as a grating or prism spectrometer spreads the Raman spectrum. The

outcome of a Raman experiment is dependent on the details of the scattering geometry, which is therefore commonly noted as $e_i(k_i, k_s)e_s$ following Porto's convention.

Atomic vibrations are one possible source for inelastic scattering. In the macroscopic, electro-dynamical picture, the electric field of the incoming light can be described as a plane wave

$$E(r, t) = E_i(\omega_i, k_i) \cos(k_i \cdot r - \omega_i \cdot t) \quad (5.1)$$

with frequency ω_i and wavevector k_i , inducing a polarization with the same wavevector and frequency in the medium, and with the amplitude depending on the susceptibility χ according to $P(\omega_i, k_i) = \chi(\omega_i, k_i)E_i(\omega_i, k_i)$. An atomic vibration displaces the atoms from their equilibrium positions also plane-wave like with the frequency of the associated phonon ω_{ph} :

$$Q(r, t) = Q_{ph}(\omega_{ph}, k_{ph}) \cos(k_{ph} \cdot r - \omega_{ph} \cdot t), \quad (5.2)$$

Taking the typical response time of the electronic system to be much shorter than the period of the phonon vibration, and its amplitude to be small compared to the bond length, the modification of the susceptibility can be described as a Taylor expansion in the atomic displacement:

$$\chi(\omega_i, k_i, Q) = \chi_0(\omega_i, k_i) + \left(\frac{\partial \chi}{\partial Q} \right)_0 Q(r, t) + \dots \quad (5.3)$$

where χ_0 is the unmodified, static part of the susceptibility, and the second term is an oscillating part induced by the oscillation of the atoms. With these two expansion terms the polarization becomes:

$$\begin{aligned} P(r, t, Q) &= \chi_0(\omega_i, k_i) E_i(\omega_i, k_i) \cos(k_i \cdot r - \omega_i \cdot t) \\ &+ \left(\frac{\partial \chi}{\partial Q} \right)_0 Q_{ph}(\omega_{ph}, k_{ph}) \cos(k_{ph} \cdot r - \omega_{ph} \cdot t) \cdot E_i(\omega_i, k_i) \cos(k_i \cdot r - \omega_i \cdot t) \end{aligned} \quad (5.4)$$

Rewriting the product of the cosine functions yields:

$$\begin{aligned} P(r, t, Q) &= \chi_0(\omega_i, k_i) E_i(\omega_i, k_i) \cos(k_i \cdot r - \omega_i \cdot t) \\ &+ \frac{1}{2} \left(\frac{\partial \chi}{\partial Q} \right)_0 Q_{ph}(\omega_{ph}, k_{ph}) E_i(\omega_i, k_i) \cdot \cos((k_i + k_{ph}) \cdot r - (\omega_i + \omega_{ph}) \cdot t) \\ &+ \frac{1}{2} \left(\frac{\partial \chi}{\partial Q} \right)_0 Q_{ph}(\omega_{ph}, k_{ph}) E_i(\omega_i, k_i) \cdot \cos((k_i - k_{ph}) \cdot r - (\omega_i - \omega_{ph}) \cdot t) \end{aligned} \quad (5.5)$$

Consequently, in a first order approximation the resulting polarization wave is frequency-modulated and has three contributions: An unaltered, elastic wave propagating with the frequency and wavevector of the incident light, a *Stokes scattered* wave with a frequency lowered by that of the phonon and an *Anti-Stokes scattered* wave with a frequency increased by that of the phonon. Usually, the Stokes-scattered light is analyzed in spectroscopic studies of the phonon frequencies while all other components, especially the elastically scattered light, are blocked by efficient filters.

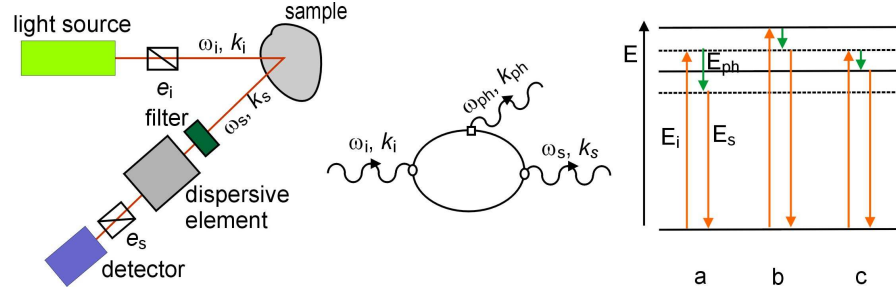


Figure 5.1: The left sketch shows a schematic view of a Raman setup. In the middle, an example Feynman diagram for the quantum mechanical view on the Stokes scattering process is displayed. On the right is an energy diagram with the possible cases for inelastic scattering in terms of the electronic states involved: dashed lines are virtual electronic bands, solid lines are real states. The incoming and outgoing light is represented by the red arrows, the energy of the created phonon by the green arrow. (a) non-resonant: Neither the incoming nor the outgoing light matches an energy difference between real electronic bands. (b) incoming resonance: The incoming light excites a carrier to a real excited state. A photon is emitted, leaving photon emitted on recombination from a virtual state. (c) outgoing resonance. A real state in the scattering process leads to strongly enhanced Raman scattering probabilities, as the denominator of the expression in Eq. 5.9 goes to zero.

The scattering process must conserve energy and momentum., i.e.

$$\hbar\omega_i = \hbar\omega_s + \hbar\omega_{ph} \quad (5.6)$$

$$k_i = k_s + k_{ph}. \quad (5.7)$$

The energy of the phonon, typically 40 meV, is much smaller than that of the incoming light in the visible range around 2.5 eV, so that the incoming and outgoing light have almost the same energy, which poses the crucial experimental challenge. The opposite situation occurs for the momentum. The maximum transfer is reached in backscattering geometry and amounts to $k_{ph} = 2k_i$. In a material with $n=1.5$ and visible light of 500 nm it is of the order of $k_i = \frac{2\pi n}{\lambda} = 0.002 \text{ \AA}^{-1}$. The range of momentum for the phonons, on the other hand, is defined by the boundaries of the Brillouin zone $\frac{\pi}{a}$, which amount to 0.8 \AA^{-1} in the plane of $\text{YBa}_2\text{Cu}_3\text{O}_{7-\delta}$. Consequently, in good approximation only the Γ -point phonons can interact with light from the visible energy range in a first order process, and methods like X-ray Raman scattering and neutron scattering are necessary to probe other parts of the Brillouin zone. Even under visible Raman excitation, however, there are several mechanisms which can partly lift this constraint. For example, structural defects in the material can take up momentum and balance the equation for phonons from other parts of the Brillouin zone. Higher order processes involving more than one phonon can also occur, where only the sum of the wavevectors must be small. In the case where pairs of phonons with almost identical but opposite momentum are created across the zone, the resulting spectrum can be used to estimate the density of states.

For a one-phonon scattering process, however, the wavevector of the phonon k_{ph} can be approximated to zero. This leaves the scattered intensity proportional to the square of the incoming amplitude, the derivative of the susceptibility tensor and the amplitude of the atomic displacements. By normalizing and contracting the displacement with the derivative, a second-rank tensor called the *Raman tensor* is obtained. Together with a polarization e_s chosen for the detection, the observed intensity is:

$$I_s \propto |e_i \cdot \left(\frac{\partial \chi}{\partial Q} \right)_0 Q_{ph, norm}(\omega_{ph}) \cdot e_s|^2 = |e_i \cdot R \cdot e_s|^2 \quad (5.8)$$

The Raman tensor components are governed by the atomic displacements of the vibrating atoms, and therefore its symmetry reflects that of the phonon and the underlying structure. By varying the direction and polarization of the incoming and the detected light, combinations of tensor components can selectively be tested. In a highly symmetric material, the scattering intensity vanishes for certain geometries. These so-called Raman selection rules allow for a determination of the symmetry of the phonons and the structure of the sample. All possible symmetry-groups of regular structures have been classified by group theory, the possible eigenvectors with their symmetries were calculated and the resulting Raman tensors can be found tabulated. [86] We will show the group theoretical properties and Raman tensors of $\text{YBa}_2\text{Cu}_3\text{O}_{7-\delta}$ later in this chapter.

A special consequence of Raman selection rules worth noting applies to centro-symmetric crystals like $\text{YBa}_2\text{Cu}_3\text{O}_{7-\delta}$, where all eigenvectors can be classified into odd and even parity. The structure is invariant under inversion, so the physical properties such as the derivative of the susceptibility must not change under that transformation. However, for an odd parity phonon its sign changes along with that of the elongation of the bonds. Consequently, the Raman tensor for odd-parity phonons must vanish to fulfill the constraint and the phonon is not visible in any geometry in the spectrum. Infrared spectroscopy, on the other hand, shows only the odd symmetry phonons and is therefore a complementary technique for the study of centro-symmetric crystals.

For the resonance phenomena in Raman spectroscopy, it is instructive to make what can only be a brief detour to the quantum mechanical description. An example of a Feynman diagram describing the Stokes process for electrons is displayed in the middle panel of Fig. 5.1. The incident photon excites an electron-hole pair, the electron then creates a phonon, and the scattered photon is emitted upon recombination of the electron and hole. The electron remains unchanged by the process and returns into its initial state. In the resonant case, contributions from other scattering processes become comparatively small and can be approximated with a constant, C . Multiplying the terms of the matrix elements for the vertices along the diagram shown, the scattering probability can then be written as: [87]

$$p \propto \left| \frac{\langle 0 | H_{r-e} | a \rangle \langle a | H_{e-ph} | a \rangle \langle a | H_{r-e} | 0 \rangle}{(E_a - \hbar\omega_i - i\Gamma_a)(E_a - \hbar\omega_s - i\Gamma_a)} + C \right|^2 \quad (5.9)$$

Here, p is the scattering probability, $\langle 0 |$ is the initial, and final, state of the electron, $\langle a |$ is an intermediate state, H_{r-e} is the Hamiltonian for photon-electron interaction, H_{e-ph} the one for

electron-phonon interaction, E_a corresponds to the energy difference between initial and excited state, Γ_a to the damping parameter due to the finite life-time of the intermediate state, and $\hbar\omega_i$ and $\hbar\omega_s$ the energy of the incident and scattered radiation.

In the non-resonant case, the intermediate electron-states are virtual. If the energy of the photon matches one of the intermediate states, the denominator of the above expression tends to zero and the scattering probability is very much enhanced. In the case of the first intermediate state this is called an ingoing resonance, but the match can also be with the second intermediate state, creating an outgoing resonance. The right panel of Fig.5.1 illustrates the (a) non-resonant, (b) ingoing resonance, and (c) outgoing resonance cases. In the case where both intermediate states are real we speak of a double resonance. In the vicinity of such a resonance, the selection rules can be altered, since $k=0$ is no longer a good approximation. Detailed information on resonant Raman scattering can be found in Ref. [88].

The resonance phenomenon alters the Raman cross section for scattering by phonons at different excitation energies. The phonon, however, will always be detected in the spectrum at the same absolute energy difference from the incident wave. By another channel, the electronic configuration also alters the line-shapes, and to a certain extent, the detected position of a phonon. Coupling of the phonon to the electronic background leads to a renormalization of the phonon energy. The Raman-peak in the spectrum appears asymmetric, shifted, and in a first order approximation has a Fano-lineshape instead of a Lorentzian, so that the “bare” phonon frequency can only be deduced after appropriate analysis. Reference [89] reviews the renormalization of phonons in superconductors.

5.2 Structure, symmetry and phonon eigenvectors in $\text{YBa}_2\text{Cu}_3\text{O}_{7-\delta}$

Group theoretical analysis yields information on the Raman and infrared active modes and their selection rules in a crystallographic structure. It is a prerequisite for the assignment of peaks detected in Raman spectroscopy to the eigenmodes of the compound. Extensive work has been done on $\text{YBa}_2\text{Cu}_3\text{O}_{7-\delta}$ in optical spectroscopy and neutron scattering. With the assistance of calculations using a shell model, almost all optically active Γ -point phonon eigenmodes were successfully assigned. However, the origin of the oxygen-vacancy activated peaks under consideration in this work is still an open question. As a base for this discussion later in this chapter, we review here the general symmetry properties and information on phonons in $\text{YBa}_2\text{Cu}_3\text{O}_{7-\delta}$.

The fully oxygenated $\text{YBa}_2\text{Cu}_3\text{O}_7$ has 13 atoms per unit cell, yielding 39 linearly independent eigenmodes of which 3 are acoustic. This leaves 36 optical eigenmodes, which are either Raman active or infrared active, or silent. We give a summary of the modes and their theoretically and experimentally obtained frequencies in Tab. 5.1. The structure is depicted with the labels for inequivalent atomic element positions in the middle panel of Fig. 5.2. In contrast to earlier pictures, the chain plane in Fig. 5.2 is at the center of the two unit cells drawn. The symmetry of the

Table 5.1: Phonon frequencies of $\text{YBa}_2\text{Cu}_3\text{O}_{7-\delta}$, fully or optimally oxygenated, in (cm^{-1}). Columns: *eigenv.* predominant character of the mode, *shell* shell model calculations [90], *abin.* ab initio calculation [67], *neutron* neutron scattering, *IR* infrared spectroscopy from [91] and [67] and references therein, *Raman* Raman results $\text{YBa}_2\text{Cu}_3\text{O}_{7-\delta}$ [15, 62, 91, 92], *YBCO6* corresponding Raman frequencies in $\text{YBa}_2\text{Cu}_3\text{O}_6$ [93], *Y124* corresponding Raman frequencies in $\text{YBa}_2\text{Cu}_4\text{O}_8$ [94], (*) there is an additional CuI phonon at 250 cm^{-1} , the 605 cm^{-1} peak has previously been assigned to the OI mode and the 500 cm^{-1} and vice versa [94, 95].

rep.	eigenv.	shell	abin.	neutron	IR	Raman	YBCO6	Y124
A_{1g}	Ba	115	119	120		112 - 116	115	104
	CuII	157	152	157		145 - 154	145	153
	O2O3-	353	340	340		335 - 340	341	341
	O2O3+	377	407	434		435 - 440	454	438
	OIV	509	473	506		493 - 500	472	500, 605*
B_{2g}	Ba	70	65			70		
	CuII	142	140			142		
	OIV	346	224			210		
	OIII	428	387			371		
	OII	564	576			580		
B_{3g}	Ba	91	79			83		
	CuII	137	140			140		
	OIV	490	295			304		
	OII	411	366			379		
	OIII	545	526			526		
B_{1u}	Ba	95	130			-, 104		
	CuI	151	167	157		155, 151		
	Y/CuII	196	192	193		193, 191		
	O2O3-	308	218			-, -		
	OI	317	241			275, 280		
	O2O3+ in	370	325	300		300, 309		
	OIV	531	551	550		567, 563		
B_{2u}	Y/Ba	37	83	82				
	OI	115	132	126				
	CuI	197	153	157				
	Y/CuII	354	176	194		190		
	OIV	361	270	283		280		
	OIII	565	360	355		362		
	OII	153	580	600		597		
B_{3u}	Y/Ba	101	81	82				
	CuI	127	159	157				
	Y/CuII	191	171	189		189		
	OIV	348	337	367		362		
	OII	362	344	359		362		
	OI	546	496	479		478		
	OIII	573	530	549		546		

Table 5.2: Crystallographic groups and dimensions of $\text{YBa}_2\text{Cu}_3\text{O}_{7-\delta}$ and related compounds.

compound	gr. No.	space group	point group	a (Å)	b (Å)	c (Å)
$\text{YBa}_2\text{Cu}_3\text{O}_7$ [89]	47	D_{2h}^1, P_{mmm}	D_{2h}, mmm	3.8136	3.8845	11.6603
$\text{YBa}_2\text{Cu}_3\text{O}_6$ [33, 93]	123	$D_{4h}^1, P_{4/mmm}$	$D_{4h}, 4/mmm$	3.8544	3.8544	11.8175
$\text{YBa}_2\text{Cu}_4\text{O}_8$ [94]	65	D_{2h}^{19}, A_{mmm}	D_{2h}, mmm	3.852	3.879	27.27

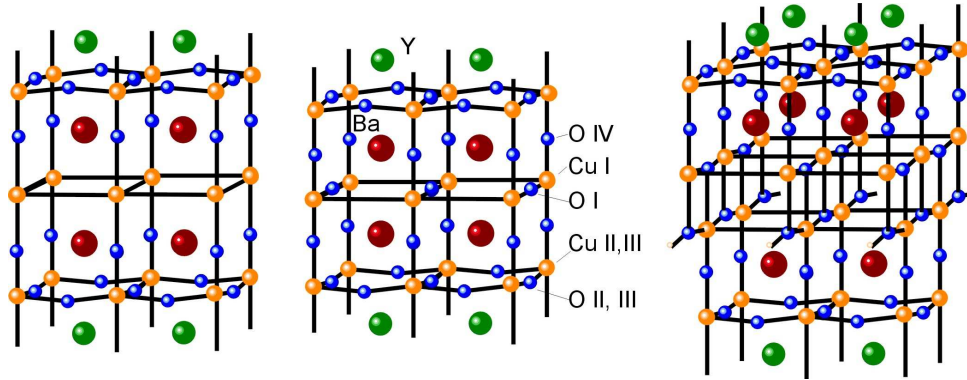


Figure 5.2: Left panel: insulating parent compound $\text{YBa}_2\text{Cu}_3\text{O}_6$, tetragonal, no or empty Cu-O chains, inversion-invariant, point group D_{4h} . Middle panel: fully oxygenated $\text{YBa}_2\text{Cu}_3\text{O}_7$, orthorhombic, point group D_{2h} , Cu-O chains at inversion centers of the cell. Right panel: $\text{YBa}_2\text{Cu}_4\text{O}_8$, a related compound, orthorhombic, with a double Cu-O chain so that the chain atoms are not at centers of inversion. Details on the symmetry and dimensions are summarized in Tab. 5.2.

$D_{2h}(\text{mmm})$	E	C_{2z}	C_{2y}	C_{2x}	I	σ_z	σ_y	σ_x	
A_g	1	1	1	1	1	1	1	1	x^2, y^2, z^2
A_u	1	1	1	1	-1	-1	-1	-1	
B_{1g}	1	1	-1	-1	1	1	-1	-1	xy
B_{1u}	1	1	-1	-1	-1	-1	1	1	z
B_{2g}	1	-1	1	-1	1	-1	1	-1	xz
B_{2u}	1	-1	1	-1	-1	1	-1	1	y
B_{3g}	1	-1	-1	1	1	-1	-1	1	yz
B_{3u}	1	-1	-1	1	-1	1	1	-1	x

Table 5.3: Character table of the point group, with the symmetry transformations and the irreducible representations

structure belongs to the point-group D_{2h} in Schönflies-notation (mmm in international notation). As seen from the corresponding character table in Tab. 5.3, it has three mirror planes and three C_2 rotational axes. The crystallographic axes in $\text{YBa}_2\text{Cu}_3\text{O}_{7-\delta}$ are at right angles to each other, so it is easy to find the planes and rotational axes in the structure along the crystallographic axes and their planes. The group also includes the inversion operation. As explained in the previous section, the phonon eigenvectors are consequently divided in even, Raman active, and odd, infrared active modes. The analysis of the dynamical matrix yields $5 A_g + 5 B_{2g} + 5 B_{3g} + 7 B_{1u} + 7 B_{2u} + 7 B_{3u} = 36$ representations for the phonon-eigenmodes of $\text{YBa}_2\text{Cu}_3\text{O}_7$. [62, 89] Only the $5 A_g$ modes are found at 112, 154, 340, 440 and 500 cm^{-1} in most Raman spectra, the Raman cross section of the B_{2g} is very small. [62, 92]

A full set of eigenvectors according to their representation, together with results on the frequencies, the Raman spectra and the mode assignment can be found in Refs. [62, 90, 91]. Here, we show some examples in Fig. 5.3. Though in principle any number of atoms can be involved

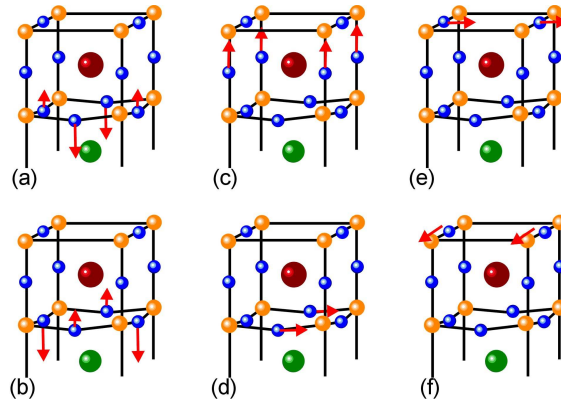


Figure 5.3: Schematic phonon eigenvectors, the lower half of the unit cell can be obtained by mirroring (even) or inverting (odd) the upper half. For most Γ -point vibrations, there is little mixing and the eigenvectors can be characterized by giving the “dominantly” moving atom. (a) and (b) show the O2O3-, or oxygen-out-of plane, or pseudo B_{1g} mode. This mode has the full symmetry of the system, A_g . The same is true for the OIV, or apical mode in (c). (d) shows an in-plane oxygen mode of B_{2g} type, which must have a similar frequency to the corresponding B_{2g} . Only the chain modes in (e) and (f) are fundamentally different looking in a and b direction. A full set of eigenvectors from a shell model calculation can be found in Refs. [62, 91].

in each mode, for most phonons at the Γ point a predominant motion can be assigned to atoms on specific sites in the unit cell. In Fig. 5.3(a) and (b) we show schematically the elongations for the mode where the in-plane oxygen atoms vibrate out of phase (O2O3- in Tab. 5.1). Obviously, the difference between a and b direction is just a phase, so that the mode has the full symmetry of the structure, A_g . The same is true for the apical oxygen mode in (c) (OIV in Tab. 5.1), which has elongations along the c direction, like all five modes with A_g symmetry. Fig. 5.3(d) shows an in-plane oxygen mode with elongation in the plane and, consequently, symmetry B_{2g} or B_{2u} . It has a related phonon where the oxygen atoms in the b direction make the same motion, that is expected to display a very similar frequency. This again is true for all modes except the chain-plane related ones. The bond-stretching vibration of the oxygen atom along the chain in Fig. 5.3(f) has no related mode other than the bond-bending one in (e) with a much lower frequency.

In Fig. 5.2 it can be seen that the CuI and the OI chain atoms, like the Y atom, occupy inversion centers of the cell. All related modes must therefore be odd and consequently not Raman-active. This is not the case in the related compound $\text{YBa}_2\text{Cu}_4\text{O}_8$, which is depicted in Fig. 5.2. It is similar to $\text{YBa}_2\text{Cu}_3\text{O}_7$, but has two Cu-O chains per unit cell, which are shifted with respect to each other along b by half the length of the base vector. The point group of this structure is still D_{2h} , but the chain atoms are no longer at centers of inversion. Indeed, the Raman spectra of $\text{YBa}_2\text{Cu}_4\text{O}_8$ show two additional modes at 250 cm^{-1} and 605 cm^{-1} , which have consequently been assigned to chain vibrations. [94] Recent ab-initio calculations, however, swap the assignment of the apical oxygen mode and the chain-oxygen mode, putting the latter at 500 cm^{-1} . [95] The anisotropy provides some assistance for this reassignment, since the intensity in $z(x,x)z$ and $z(y,y)z$ is more anisotropic

Table 5.4: Correlation table D_{4h} to D_{2h} .

D_{4h}		A_{1g}	A_{2g}	B_{1g}	B_{2g}	E_g	A_{1u}	A_{2u}	B_{1u}	B_{2u}	E_u
D_{2h}	$C_{2'}$	A_g	B_{1g}	A_g	B_{1g}	$B_{2g}+B_{3g}$	A_u	B_{1u}	A_u	B_{1u}	$B_{2u}+B_{3u}$
	$C_{2''}$	A_g	B_{1g}	B_{1g}	A_g	$B_{2g}+B_{3g}$	A_u	B_{1u}	B_{1u}	A_u	$B_{2u}+B_{3u}$

for the 500 cm^{-1} mode than for the 605 cm^{-1} mode in Ref. [94]. The additional bond of the chain atoms thus alters the vibrational properties, hindering a direct comparison of the chain modes in $\text{YBa}_2\text{Cu}_4\text{O}_8$ and $\text{YBa}_2\text{Cu}_3\text{O}_7$.

Another structure worth considering for its similarity is the insulating parent compound $\text{YBa}_2\text{Cu}_3\text{O}_6$, which is depicted in Fig. 5.2 on the left. Here, all chain oxygen atoms are missing, and the a and b axes are identical, so that the structure has a fourfold rotational symmetry around the c direction instead of only a twofold. Consequently, this compound belongs to the higher symmetry point-group D_{4h} . Because the structural difference to the superconducting compound is small, the higher symmetry properties of D_{4h} are reflected in the relative signal strength in D_{2h} . Table 5.4 shows the correlation between the representations. The general form of Raman tensors belonging to the same irreducible representation as the phonons are tabulated in Ref. [88], and are for these two groups:

$$\begin{pmatrix} xx & & \\ & yy & \\ & & zz \end{pmatrix} \begin{pmatrix} & yx & \\ xy & & \\ & & \end{pmatrix} \begin{pmatrix} & & zx \\ & & \\ xz & & \end{pmatrix} \begin{pmatrix} & & \\ & & zy \\ & yz & \end{pmatrix} \quad (5.10)$$

$$\begin{array}{l} D_{2h} : \\ (mmm) \end{array} \quad \begin{array}{cccc} A_g (\Gamma_1^+) & B_{1g} (\Gamma_2^+) & B_{2g} (\Gamma_3^+) & B_{3g} (\Gamma_4^+) \end{array}$$

$$\begin{pmatrix} xx & & \\ & xx & \\ & & zz \end{pmatrix} \begin{pmatrix} & yx & \\ -yx & & \\ & & \end{pmatrix} \begin{pmatrix} xx & & \\ & -xx & \\ & & \end{pmatrix} \begin{pmatrix} & yx & \\ yx & & \\ & & \end{pmatrix} \quad (5.11)$$

$$\begin{array}{l} D_{4h} : \\ (4mmm) \end{array} \quad \begin{array}{cccc} A_{1g} (\Gamma_1) & A_{2g} (\Gamma_2) & B_{1g} (\Gamma_3) & B_{2g} (\Gamma_4) \end{array}$$

$$\underbrace{\begin{pmatrix} & zx \\ xz & \end{pmatrix} \begin{pmatrix} & \\ & zy \\ yz & \end{pmatrix}}_{E(\Gamma_5)}$$

According to the correspondence table 5.4, A_g representations in D_{2h} originate from either A_{1g} or B_{1g} in D_{4h} .

Five Raman-active peaks are found in the tetragonal compound with vibration in z -direction, four of A_{1g} and one of B_{1g} symmetry (see frequencies in Tab. 5.1). [93] These compare well with the five strong A_g phonons in the orthorhombic compound, of which 4 are A_{1g} -like, and one, the in-plane oxygen out of phase mode at 340 cm^{-1} , is B_{1g} -like (*hence it is often referred to as pseudo- B_{1g}*). The in-plane components for the modes at 440 and 500 cm^{-1} are small, the peaks are strong in spectra taken with polarization along the c -axis.

5.2.1 Parameters influencing the phonon frequencies

The phonon frequency depends on the bond length between atoms in the unit cell, which in turn depend on the temperature, the rare earth R in $\text{R}\text{Ba}_2\text{Cu}_3\text{O}_{7-\delta}$, the oxygen content and the ordering. The work invested into this complex field is extensive and cannot be reviewed here, so we restrict ourselves to giving information for further reading.

The change of bond-length upon substitution of the rare earth atom is summarized in Ref. [16], the corresponding change in Raman frequencies can be found in Refs. [96,97]. Bond length versus oxygen depletion were published by Cava *et al.* [33], with the corresponding Raman frequency shift in Ref. [98]. The apical oxygen mode shifts by a comparatively large amount of 10 cm^{-1} throughout the phase diagram and therefore is a good indicator of oxygen content. The shift is linear according to Ref. [98]. In Ref. [15], however, a deviation from linear behavior is found.

$\text{YBa}_2\text{Cu}_3\text{O}_{7-\delta}$ allows for site-selective isotope substitution of the oxygen atoms, which can be monitored using Raman spectroscopy. [66, 99–101]. The work of Ref. [15] is a recent, detailed review on oxygen diffusion in the compound, including isotope substitution, axes length and Raman frequencies. In Ref. [102] Raman spectra of impurity phases are shown, which occurred in some samples in the early stage of the research on growth.

A review on light scattering in high temperature superconductors is found in Refs. [89] and [103], a review on the infrared active modes in Ref. [91], a review on neutron scattering results by Reichardt in Ref. [104] and very recently by Pintschovius in Ref. [105].

5.2.2 Phonon dispersion

Defect-related modes do not necessarily obey the $k=0$ selection rule in Raman scattering, so modes from other parts of the Brillouin zone can be of interest. The phonon dispersion of $\text{YBa}_2\text{Cu}_3\text{O}_{7-\delta}$ was calculated early on the base of a shell model by Kress *et al.* [62, 65, 90] Recently, another shell model approach has been used by Pintschovius *et al.* [105–107] and compared to neutron scattering results, which have also progressed to great detail. With growing computer capacity ab-initio calculations on such larger unit cells were published. The Raman response for some allowed modes versus excitation energy was calculated on the base of ab-initio (density functional, plane wave) methods by Heyen *et al.* [108] and Ambrosch-Draxl *et al.* [109] Another group, Bohnen *et al.*, calculated the phonon and the electronic dispersion using a mixed-basis, pseudo

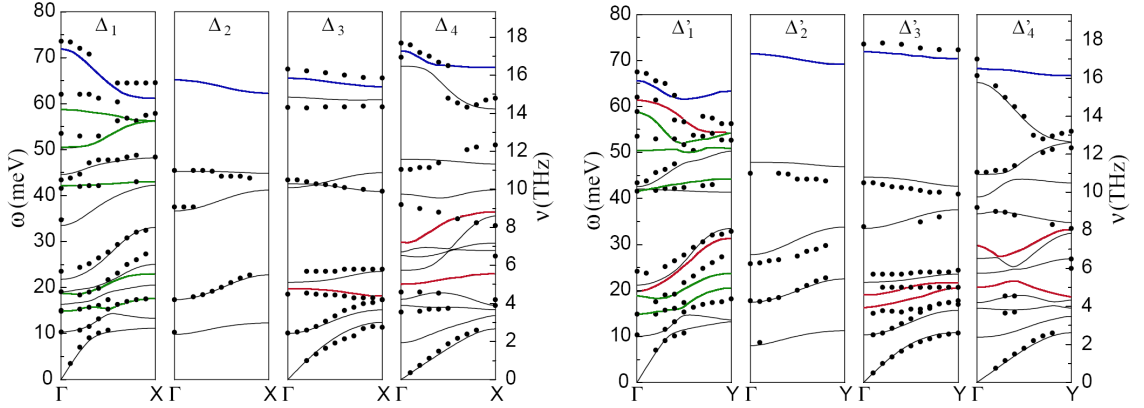


Figure 5.4: Phonon dispersion obtained from first principles calculations and neutron scattering data, taken from Ref. [67]. On the left, phonons are propagating along (100), on the right along (010). We highlight dispersion branches according to their Γ -point symmetry here. Green dispersion branches correspond to A_g symmetry, the Raman-active, strong modes. Red branches involve chain-atoms. Blue branches are the in-plane oxygen vibrations of B_{2g} , B_{3g} , B_{2u} and B_{3u}

Table 5.5: Correlation table D_{2h} to C_{2v} .

D_{2h}		A_g	B_{1g}	B_{2g}	B_{3g}	A_u	B_{1u}	B_{2u}	B_{3u}
C_{2v}	C_{2x}	$A_1 (\Delta_1)$	$B_1 (\Delta_3)$	$B_2 (\Delta_4)$	$A_2 (\Delta_2)$	$A_2 (\Delta_2)$	$B_2 (\Delta_4)$	$B_1 (\Delta_3)$	$A_1 (\Delta_1)$
	C_{2y}	$A_1 (\Delta_1)$	$B_1 (\Delta_3)$	$A_2 (\Delta_2)$	$B_2 (\Delta_4)$	$A_2 (\Delta_2)$	$B_2 (\Delta_4)$	$A_1 (\Delta_1)$	$B_1 (\Delta_3)$

potential method. [67] We reproduce their phonon dispersion in Fig. 5.4 and compare the phonon frequencies to that of the shell model and the experimental findings in Tab. 5.1.

Figure 5.5 shows the Brillouin zones of D_{2h} and D_{4h} with the notation for the directions in the zone. In D_{2h} , the direction from Γ to X is called Σ , from Γ to Y it is Δ . To avoid a confusion with Γ to M in D_{4h} , the pseudo-tetragonal notation is used with Δ and Δ' . Away from the high symmetry points, the symmetry in the Brillouin zone for phonons with a non-vanishing k vector and a propagation direction along Δ or Δ' is reduced to C_{2v} , with the representations $A_1 (\Delta_1)$, $A_2 (\Delta_2)$, $B_1 (\Delta_3)$ and $B_2 (\Delta_4)$. The table 5.5 shows the correspondence.

With the help of the representation and the frequencies given in Ref. [67], we have highlighted the phonon branches corresponding to the Raman active A_g modes at Γ in green. Modes involving

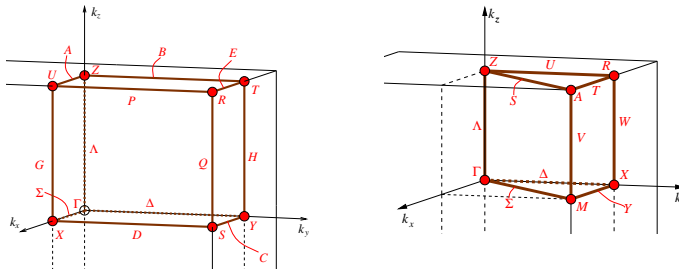


Figure 5.5: Brillouin zones for the point groups D_{2h} (left) and D_{4h} (right). [110]

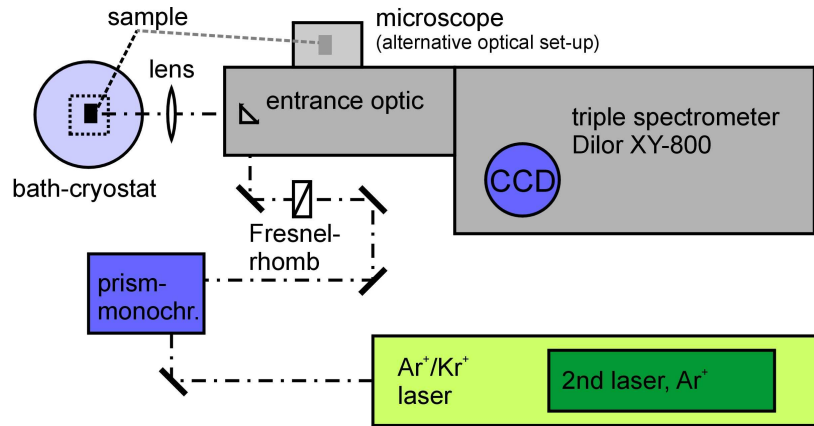


Figure 5.6: Raman setup with a Dilor XY 800 triple spectrometer for the visible and near infrared range at the group of Prof. Dr. C. Thomsen, Technical University Berlin, Germany.

chain-atoms are highlighted in red, and the highest modes, which are all in-plane OII and OIII related, in blue. We have highlighted the chain and the in-plane modes, because their positions are at variance with early shell model calculations and question the assignment of the oxygen-vacancy activated Raman peaks made previously. We will discuss the modes further in the context of our Raman results in section 5.4.

5.3 Raman experimental details

The Raman experiments in this work were taken on different setups, in order to account for the dependence of the spectra on the excitation energy used. As mentioned in section 5.1, the Raman cross section greatly depends on the electronic resonances. After finding that reflectance anisotropy spectra show persistent photo-induced change in the ultraviolet we explicitly studied Raman in this excitation range. We performed the experiment with our collaborators from the Université Paul Sabatier Toulouse, France, and from Universität Hamburg, Germany. A setup used for simultaneous Raman and transport experiments in the Centro Atómico Bariloche, Argentina, is described in the next chapter. All samples studied in the Raman experiments were provided by Prof. Dr. G. Nieva, Centro Atómico Bariloche (see Appendix A).

5.3.1 Dilor XY 800, Berlin

This setup was used in most spectra and illumination series acquired in the visible range, in particular for resonant scattering of oxygen-vacancy activated modes at 2.18 eV. A sketch of the configuration is shown in Fig. 5.6. The spectrometer is a Dilor XY 800 triple stage monochromator with a grating of 1800 lines/mm (or optional 1200 lines/mm), equipped for the visible and near-infrared range. The first two stages were used in subtractive mode to cut out the spectral

window of interest and to ensure good stray-light suppression. Typically, the entrance and exit slits were $300 \mu\text{m}$. This configuration allows measurements close to the laser line with a spectral resolution of about 2 cm^{-1} . The spectrometer is equipped with two charge coupled device detectors, a Peltier-cooled camera optimized for the infrared range, and a liquid-nitrogen cooled camera from Wright Instruments for the visible range. A full spectrum can thus be acquired at once. Generally, the cuprates are poor scatterers, requiring a minimum accumulation time of about 60 s per spectrum. All experiments were done in backscattering geometry. An achromatic lens or a camera lens focus the incoming beam onto the sample and collect the scattered light. The focus diameter was between 20 and $100 \mu\text{m}$.

The incident polarization is chosen by turning the linearly polarized laser light with a Fresnel-rhomb. A linear polarization filter selects the detected polarization in the entrance optic of the spectrometer. Among the available lasers we used the 488, 514 and 568 nm lines of an Ar^+ - Kr^+ gas laser, and in the two-color experiments a second Ar^+ laser with 488 and 514 nm. A prism spectrometer filters the plasma-lines from the beam. The excitation power used was between 3 and 6 mW outside the cryostat windows, a rather low value in order to avoid heating effects.

For the low-temperature measurements the sample was mounted in an Oxford bath-cryostat with a maximum cooling rate of 20 K/min. Prior to sequential experiments on the photo-induced change, the samples were kept in the dark for several weeks to ensure full relaxation to the equilibrium state. We then quenched them to the chosen temperature at the maximum cooling rate. Care was taken to chose a new, previously unilluminated spot for each run. When no more unilluminated spots were available, the samples were relaxed at room temperature in the dark for at least 12 h.

In a two-color experiment, the second laser was reflected into the path through the same focussing lens at a small angle ($< 10^\circ$). The polarization of the second laser-beam (vertical or horizontal in the laboratory frame, along a or b crystallographic axes in the frame of the sample) was chosen using a $\lambda/2$ -plate and a polarizer before the last mirror, which was oriented at 45° to the beam.

5.3.2 Dilor spectrometer equipped for UV, Toulouse

In the group of Prof. Dr. W. Bacsa and coworkers, we took spectra at 3.7 eV excitation energy. The setup is similar to the one described previously, but specially trimmed for the UV, namely a triple Dilor spectrometer equipped with UV mirror optic and gratings. It has a liquid-nitrogen cooled CCD detector. Similar to the visible setup, we again used backscattering geometry with a lens focussing and collecting the scattered light.

For the excitation, we used the 333.6 nm line of an Ar^+ laser with a power of 4 mW. The size of the focus was $40 \mu\text{m}$ in diameter. The spectra had relatively long accumulation times of between 15 min and two hours to make up for the weak Raman cross-section of the high- T_c materials. The full width at half maximum of the plasma lines is 5 cm^{-1} .

5.3.3 UV-VUV Raman spectrometer UT-3, Hamburg

The Raman experiments at higher UV excitation energies 4.1 and 4.8 eV were performed in the group of Prof. Dr. M. Rübhausen on a McPherson Raman spectrometer equipped with a UV-sensitive charge-coupled device. It is a recently developed triple grating spectrometer with an entrance optic constructed from parabolic mirrors in a Cassegrain-type arrangement. This fully reflective concept makes the system achromatic, providing access to the large spectral range between 165 and 1000 nm. Between the first two monochromator stages, which are used as a band filter for the spectral range of interest as in the other spectrometers, an extra stage is built in for enhanced stray-light suppression. Detailed information about the instrument can be found in Ref. [111].

The samples were mounted in a He-cooled exchange gas cryostat. For excitation, we used the 575 nm line of a Kr^+ laser with 14 mW and the 302 nm line of an Ar^+ laser with 5 mW. For these wavelengths, the incident polarization was chosen with a polarization scrambler and a subsequent linear polarizer. The detected polarization was also linear. For excitation at 4.8 eV, an intra-cavity frequency doubling unit was used to double the 514 nm line to 257 nm. At this energy we did not select a completely linear polarization. The power ratio along the maximum and minimum directions were 1.8 mW to 0.3 mW. The diameter of the focus was 20 μm for all wavelengths.

In order to compare the intensity of the spectra taken with this setup at different wavelengths, the following corrections were applied to the spectra:

- subtraction of a camera-related background
- division by system-sensitivity data obtained from Ulbricht sphere calibration lamps
- multiplication by the Bose correction factor to account for different temperatures
- normalization to incident power of 5 mW and integration time of 30 s.

5.4 Oxygen-vacancy activated phonons

In this section we present our experimental data on the basic properties of the oxygen-vacancy activated Raman modes. We summarize their identification, selection rules, and dependence on composition, temperature and excitation energy in various types of strongly underdoped $R\text{Ba}_2\text{Cu}_3\text{O}_{7-\delta}$ (R rare earth atom). We find that the Raman selection rules and the cross section are directly connected to the electronic anisotropy described in Chap. 4. These properties yield clear criteria for the identification of signals related to photo-induced change. The possibilities for the peak assignment are discussed, before we proceed to the study of the dynamics of photo-induced change in the next section.

Figure 5.7 shows Raman spectra taken sequentially on a ceramic $\text{YBa}_2\text{Cu}_3\text{O}_{6.7}$ sample using two different excitation energies. Since the sample is polycrystalline, the scattered signal is

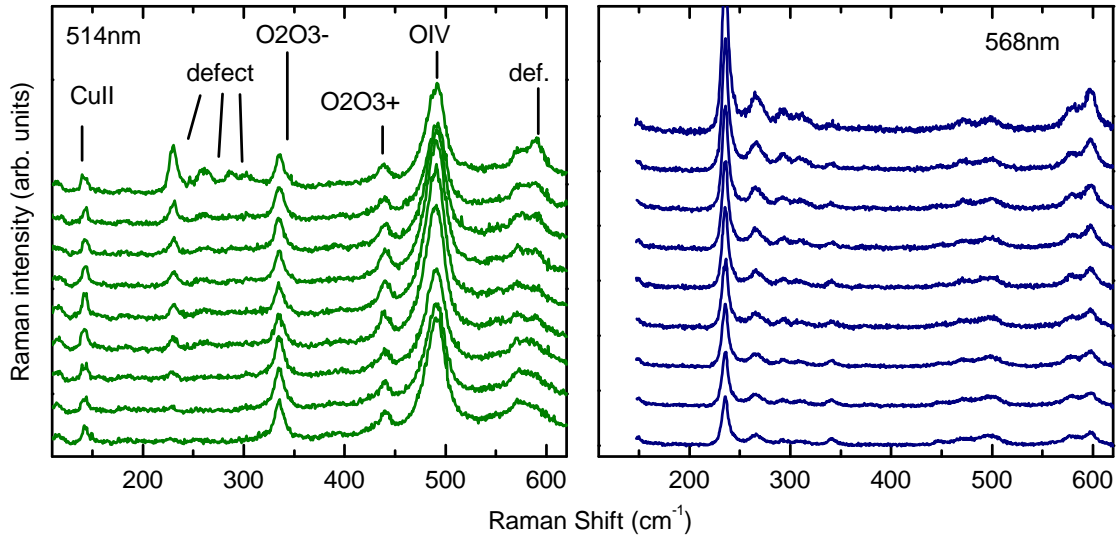


Figure 5.7: Sequence of Raman spectra taken during a time span of 2 h on a polycrystalline sample of $\text{YBa}_2\text{Cu}_3\text{O}_{6.7}$ at 80 K with 514 nm and 568 nm excitation. In the latter the oxygen-vacancy activated modes are strongly resonant. The spectra are offset by a constant amount, the first spectrum is at the top.

averaged over the crystallographic directions, and all A_g modes in range can be identified in the left panel (compare also the example Raman spectra from a single crystal in Fig. 2.11 in the introductory Chap. 2): The CuII mode, the O2O3- (or pseudo- B_{1g} , or oxygen out-of-phase) mode, the O2O3+ (oxygen in-phase) mode and the OIV (apical) mode. The Ba mode at 112 cm^{-1} is not included in the spectral window, and the B_{2g} and B_{3g} are too weak to be seen, although they are allowed by symmetry in this configuration. In the sequence of spectra, the Raman-allowed modes remain unaltered, whereas the oxygen-vacancy activated (or shorter, defect-induced) modes change during illumination. The peaks indicated as “defect” above 230 and around 600 cm^{-1} decrease in intensity compared to the Raman-allowed modes, showing the “photo-bleaching” first reported by Wake *et al.* as described in Chap. 2. From the fact that the Raman-allowed modes do not weaken or shift, it is clear that the process is not destructive or corrosive. Meanwhile, this conclusion is also supported by the reflectance anisotropy results, where recovery from photo-induced change at room temperature can be watched directly. Note the time-scale of the process evident in the 2-h sequence. The right panel in Fig. 5.7 shows the same experiment on a fresh location on the sample using 2.18 eV excitation energy. This lies within the known resonance of the defect-induced modes centered around 2.2 eV with FWHM 160 meV, which is not shared by Raman-allowed modes. [11,61] In fact, the B_{1g} , oxygen in-phase and apical mode are still present, but dwarfed on the scale of the dominating defect-induced modes here. The peaks are asymmetric, which is most obvious in Lorentzian lineshape fits to the peak at 234 cm^{-1} , and sit on top of a broad background, which possibly contains more features. The asymmetry of the peaks indicates

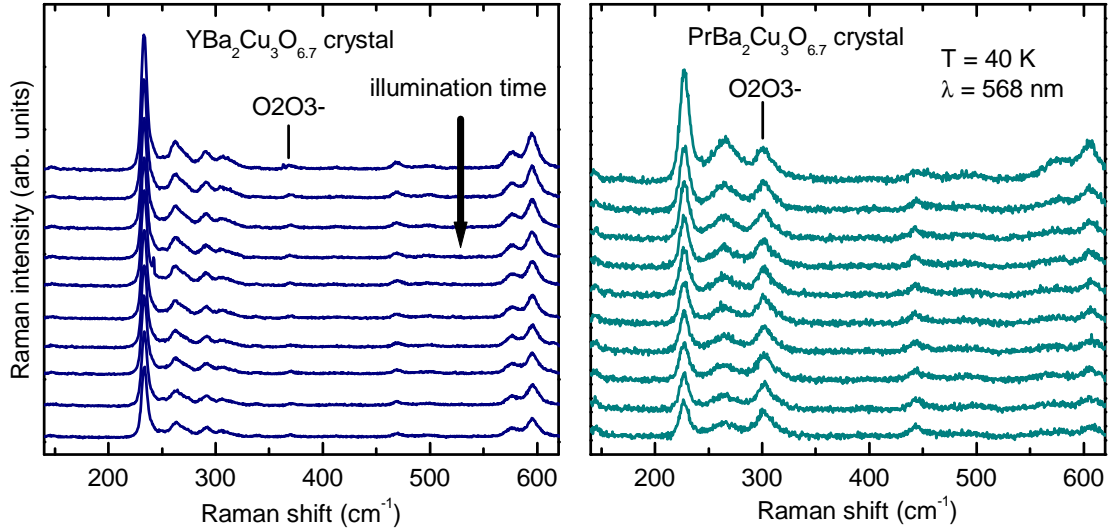


Figure 5.8: Sequence of Raman spectra taken during a time span of 45 min on $\text{YBa}_2\text{Cu}_3\text{O}_{6.7}$ and $\text{PrBa}_2\text{Cu}_3\text{O}_{6.7}$ single crystals at 40 K with 568 nm excitation ($P=6$ mw, $t=90$ s). In $R=\text{Pr}$, the defect modes exist and bleach, but are smaller in comparison with the Raman-allowed modes. The spectra are offset by a constant amount, the first spectrum is at the top.

either that they renormalize upon interaction with some electronic background, or that they reflect part of a density of states instead of just Γ -point phonons. Peaks at 234, 265, 291, 309, 579 and 597 cm^{-1} again decrease under illumination (see Tab. 5.6 for a summary of all modes).

In Fig. 5.8 a similar sequential study on single crystals of $\text{YBa}_2\text{Cu}_3\text{O}_{6.7}$ and $\text{PrBa}_2\text{Cu}_3\text{O}_{6.7}$ is displayed. The macroscopically defined crystallographic axes in these samples enable the selection of a specific scattering geometry, which here was in-plane, with the laser beam propagating along the c axis [$z(y,y)z$ in Porto's notation]. Consequently, the oxygen in-phase and the apical oxygen modes are only weakly detected in the $\text{YBa}_2\text{Cu}_3\text{O}_{6.7}$ (compare Fig. 2.11, Chap. 2). The B_{1g} is barely visible on this scale, where the resonant defect-induced modes dominate. The resonance is different in a sequence taken from a $\text{PrBa}_2\text{Cu}_3\text{O}_{6.7}$ crystal with the same excitation energy, as shown in the right panel of Fig. 5.8. The B_{1g} , oxygen in-phase and apical modes show at 301, 443 and 490 cm^{-1} , respectively. The defect-induced modes have about the same intensity as the allowed modes here. They show the same type of intensity decrease under illumination (at 228, 264, 573 and 607 cm^{-1} , see Tab. 5.6 for a summary of defect-induced mode frequencies).

5.4.1 Systematic variation of the rare earth atom and the oxygen concentration

Oxygen-vacancy related Raman peaks have been identified in this material family for all rare earth atoms investigated. [60,63,97] Since the rare earth ions have slightly different ionic radii, the volume and orthorhombicity of the unit cell changes, leading to a systematic shift in the vibrational

frequencies versus ionic radius. [16, 96, 97] We note again that even the non-superconducting compound with $R = \text{Pr}$ displays the photo-induced modes and bleaching. Examples of spectra taken under non-resonant conditions at 2.41 eV and resonant conditions at 2.18 eV excitation energy are displayed in Fig. 5.4 along with the frequency shift of selected Raman-allowed and photo-induced modes. In the spectra taken at 2.18 eV excitation energy the defect-modes decrease in intensity with increasing ionic radius, indicating that the electronic excitation responsible for the resonance centered at 2.2 eV is either weakening or shifting. In Fig. 5.8, this caused the Raman-allowed modes to be observable on the same scale as the defect-induced modes in the bleaching sequence. To the best of our knowledge, the resonance profile has so far only been determined for the Y component. [11, 58, 61] It would be interesting to measure it for a different rare earth.

Another, more central issue where the determination of a resonance profile could resolve open questions is the dependence of the resonance on oxygen content. As was reported in the literature,

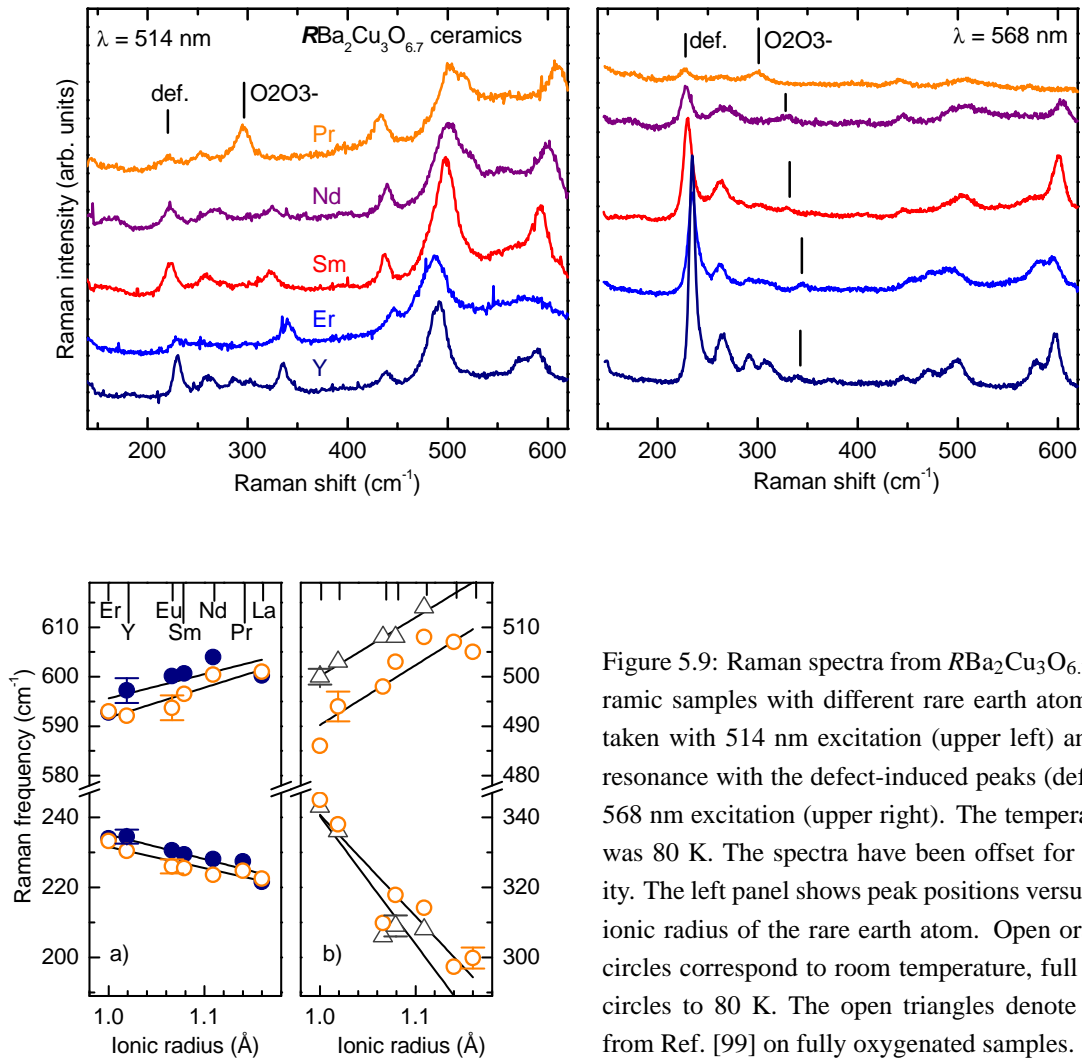


Figure 5.9: Raman spectra from $\text{RBa}_2\text{Cu}_3\text{O}_{6.7}$ ceramic samples with different rare earth atoms R , taken with 514 nm excitation (upper left) and in resonance with the defect-induced peaks (def.) at 568 nm excitation (upper right). The temperature was 80 K. The spectra have been offset for clarity. The left panel shows peak positions versus the ionic radius of the rare earth atom. Open orange circles correspond to room temperature, full blue circles to 80 K. The open triangles denote data from Ref. [99] on fully oxygenated samples. [97]

the intensity ratio of the defect-induced signal to the Raman-allowed one is strongly dependent on oxygen content. [58, 60] In Fig. 5.10 we show spectra taken from a set of c -axis oriented $\text{GdBa}_2\text{Cu}_3\text{O}_{7-\delta}$ thin films with varying oxygen content and compare the intensity ratio of the strongest defect-induced mode and the B_{1g} to data from the literature. For fully oxygenated samples the defect-induced modes are absent. Upon oxygen reduction their strength increases steeply and reaches a maximum for the underdoped regime of the 60-K plateau. Towards the insulating phase transition around $\delta \approx 0.4$, they were reported to vanish again. However, in our data they are still weakly present in the tetragonal film with $\delta \approx 0.85$. From the fact that the modes are absent in fully oxygenated compounds stems their label “oxygen-vacancy activated” or more simply “defect-induced”. It points to an assignment of chain-related vibrations becoming Raman active due to broken symmetry, or to any vibrations activated by resonances in defect-related electronic states. The decrease in intensity towards very low oxygen contents can be interpreted in two ways: If the modes are chain-related, a certain number of defects in the chain layer can activate them, but stronger oxygen depletion will also mean that more and more of the vibrating atoms are removed. On the other hand, the electronic resonance could detune with ongoing oxygen depletion. The resonance profiles were reported for samples with 6.77 (centered at 2.15 eV) [61] and ≈ 7 (centered

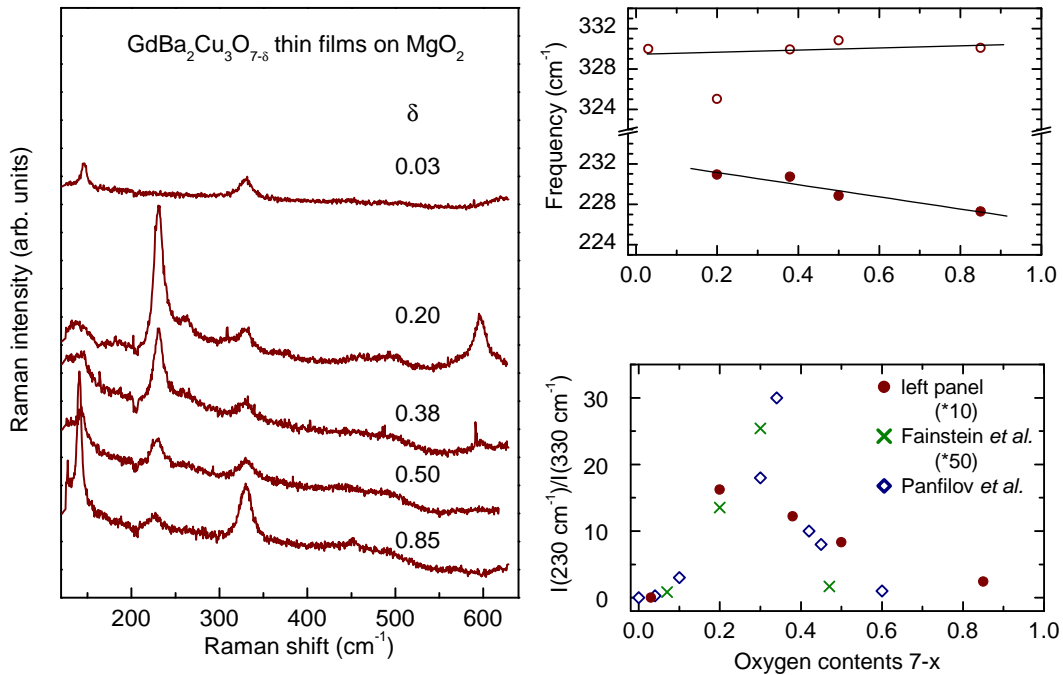


Figure 5.10: Oxygen-activated modes versus oxygen content in a set of $\text{GdBa}_2\text{Cu}_3\text{O}_{7-\delta}$ films. The spectra (left panel) were taken at room temperature using 568 nm excitation and are offset for clarity. The top right panel shows the frequency shift of the prominent peak around 230 cm^{-1} and the Raman-allowed pseudo- B_{1g} at 330 cm^{-1} . The lower right panel shows the intensity relation of the two peaks in comparison to data from Ref. [60] ($\text{GdBa}_2\text{Cu}_3\text{O}_{7-\delta}$ with 514 nm) and from Ref. [58] ($\text{YBa}_2\text{Cu}_3\text{O}_{7-\delta}$ with 568 nm).

Table 5.6: Frequencies of the oxygen-vacancy activated modes of crystalline samples in cm^{-1} . Additionally, there is a broad background probably containing more features between 230 and 330 cm^{-1} in the visible and between 100 and 700 cm^{-1} in the UV range. The experimental error is $\pm 0.5 \text{ cm}^{-1}$ at 2.18 eV and 4.10 eV, $\pm 1 \text{ cm}^{-1}$ at 3.71 eV, and $\pm 5 \text{ cm}^{-1}$ at 4.82 eV.

PrBaCuO6.7		YBaCuO6.7									
2.18 eV		2.18 eV		4.10 eV				3.71 eV		4.82 eV	
300 K	40 K	300 K	40 K	300 K		20 K		300 K	20 K	290 K	80 K
				30 min	30 s	30 min	30 s				
				110	112	112	112				
				150	150	152	155				
				179	180	178	179				
225	227	231	232	229	231						
				249	249	250	250				
260	264	261	264								
		288	291								
		306	306								
				372	373						
		576	576								
599	607	594	596	586	590	592	592	600	600	580	580

at 2.18 eV) [11]. Though this is a rather small difference compared to the width of 0.16 eV, it is reasonable to expect a larger shift when the phase transition to the tetragonal region in the oxygen phase diagram is crossed. Again, only a resonance profile of a tetragonal sample could resolve this issue.

5.4.2 Resonant Raman scattering under visible and UV excitation

After exploring the oxygen-vacancy activated modes in Raman spectroscopy under visible excitation, the results from reflectance difference anisotropy with their large, photo-sensitive feature in the UV above 4.15 eV motivated us to record Raman spectra using UV excitation in search of another resonance of the modes. Figure 5.11 shows a comparison of data taken at different wavelengths, where all spectra except the one at 2.41 eV stem from the same sample and were taken at approximately the same temperature. The inset in the uppermost panel shows a RAS spectrum with the Raman excitation energies indicated for direct comparison. At 3.7 eV, still below the onset of the UV RAS resonance, we identified a defect-induced mode at 600 cm^{-1} . [112] The group above 230 cm^{-1} is absent. This is different from the visible resonance, where the low-frequency group is prominent and the profile is very similar for both groups. [58, 59]

At 4.10 eV, a huge resonance featuring many known and new defect-induced modes on top of a broad asymmetric background ranging from 80 cm^{-1} up to 1000 cm^{-1} was discovered (This is more easily seen in the room temperature spectra we show in Fig. 5.12.). [113] The peaks

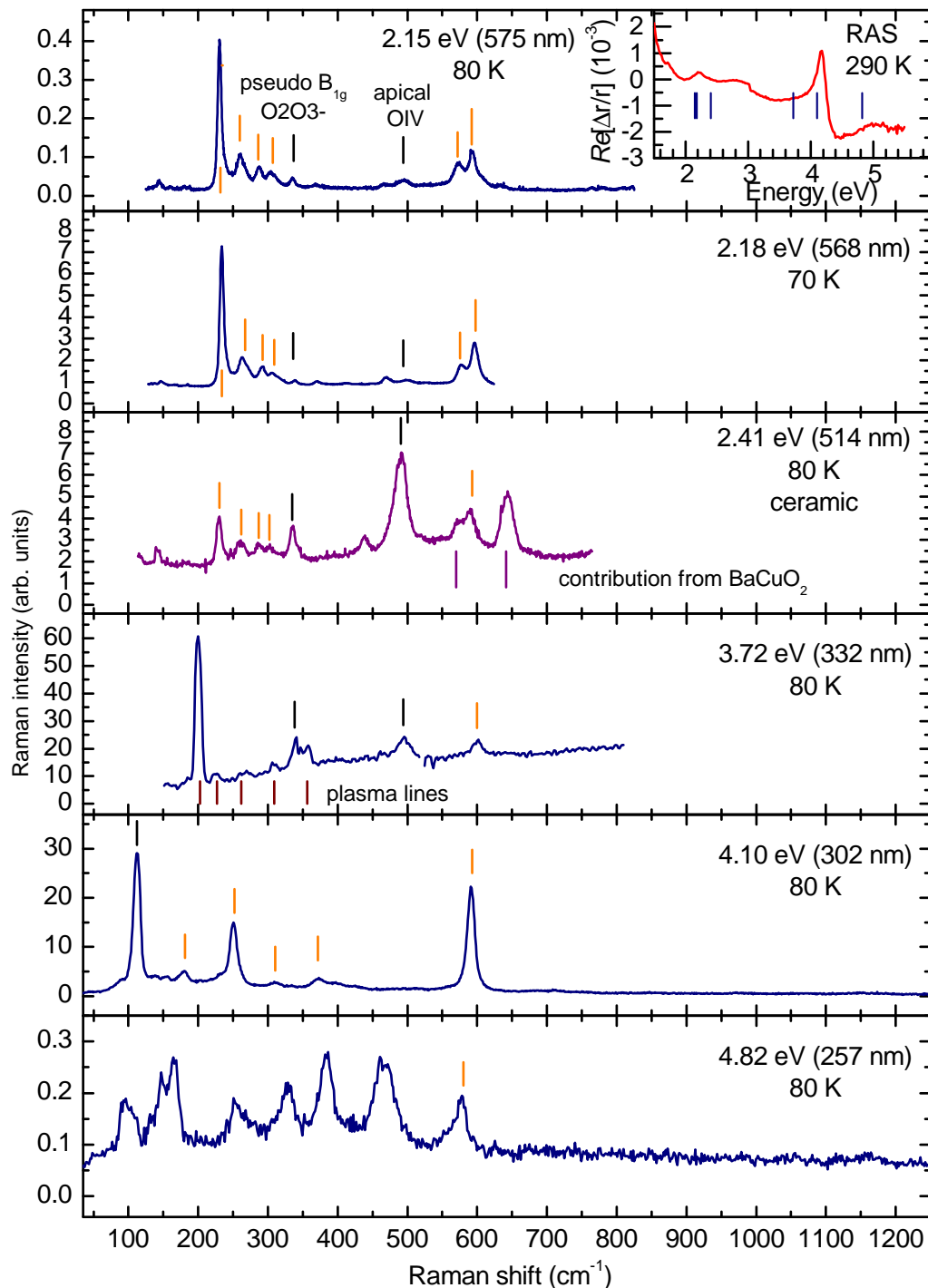


Figure 5.11: Raman spectra of $\text{YBa}_2\text{Cu}_3\text{O}_{6.7}$ taken at excitation energies varying from the visible to the UV. The excitation energies are marked in the RAS spectrum reproduced in the inset. The spectra at 2.15, 4.10 and 4.82 eV are normalized using the procedure described in section 5.3.3 and consequently have identical intensity scales. Note the strong resonance of defect-induced peaks at 4.10 eV. The spectrum at 2.41 eV is from a ceramic sample, the others all from the same single crystal. Raman-allowed modes are indicated by black lines, oxygen-vacancy activated modes by orange lines.

at 590 cm^{-1} and at 230 cm^{-1} have now reversed intensities, with the 230 cm^{-1} peak visible only at higher temperatures. Instead, new peaks appear at 112 cm^{-1} , 231 cm^{-1} , 249 cm^{-1} , and 373 cm^{-1} . The strong peak at 112 cm^{-1} coincides with the Raman-allowed A_g Ba-vibration. This can be understood from the contribution of a transfer from Cu to Ba in the 4 eV resonance. [69, 79] Beyond this resonance, at 4.82 eV excitation energy, the peak at 580 cm^{-1} is again identified (Fig. 5.11). The spectra at 2.15, 4.10 and 4.82 eV were taken on the same setup and normalized to the same standard, so that their intensity scales are comparable to each other. The Raman cross section at 4.1 eV is at least two orders of magnitude larger than for visible excitation at all temperatures, and is even higher compared to that of the Raman-allowed A_g modes, which are not visible on the same scale. Essentially the same signature of peaks, but with much lower intensity, was found in optimally doped, and even very weakly in fully oxygenated samples. [114]

We identify the oxygen-vacancy activated modes by their typical in-plane anisotropic selection rules, which were reported along with the discovery of photo-induced Raman bleaching and later reproduced in stronger depleted single crystals. [11, 58] In contrast to the Raman-allowed modes with A_g symmetry, which have nearly identical strength in $z(x,x)z$ and $z(y,y)z$ scattering geometry, the oxygen-vacancy activated modes appear only for light polarized along the chain direction b in the visible. In Fig. 5.12(a), spectra taken in these geometries from a detwinned single crystal are shown. For incident and detected polarization along a , only the B_{1g} mode, which is small on this scale, remains in the spectrum.

At 3.7 eV in Fig. 5.12(b), only the peak at 600 cm^{-1} follows the same selection rule, and is consequently identified as the only defect-induced mode in this spectrum. In (c), again all peaks at 4.1 eV are strong for incident and detected light polarized along the b -axis of the crystal, but absent for polarization along the a -axis. In addition, the scattering geometries $z(x,y)z$ and $z(x',y')z$ are shown. With the intensity in $z(x,y)z$ and $z(x,x)z$ taken as zero (there is a small signal left in the experimental spectra, which is assumed to be due to polarization leakage and uncertainty in angular alignment) and in $z(x',y')z$ approximately one quarter of that in $z(y,y)z$, the following constraints arise for the possible Raman tensor:

$$I \sim | \underline{e}_{beo} \underline{R} \underline{e}_{ein} |^2 \quad \underline{R} = \begin{pmatrix} h & j \\ l & m \end{pmatrix} \quad (5.12)$$

$$\begin{aligned}
 z(xx)z &\Rightarrow I_{xx} = \left[\begin{pmatrix} 1 & 0 \\ 0 & 0 \end{pmatrix} \begin{pmatrix} h & j \\ l & m \end{pmatrix} \begin{pmatrix} 1 \\ 0 \end{pmatrix} \right]^2 = h^2 = 0 \\
 z(yy)z &\Rightarrow I_{yy} = \left[\begin{pmatrix} 1 & 0 \\ 0 & 0 \end{pmatrix} \begin{pmatrix} h & j \\ l & m \end{pmatrix} \begin{pmatrix} 1 \\ 0 \end{pmatrix} \right]^2 = m^2 \\
 z(xy)z &\Rightarrow I_{xy} = \left[\begin{pmatrix} 0 & 1 \\ 0 & 0 \end{pmatrix} \begin{pmatrix} h & j \\ l & m \end{pmatrix} \begin{pmatrix} 1 \\ 0 \end{pmatrix} \right]^2 = l^2 = 0 \\
 z(x'y')z &\Rightarrow I_{x'y'} = \left[\frac{1}{\sqrt{2}} \begin{pmatrix} 1 & -1 \\ 0 & 0 \end{pmatrix} \begin{pmatrix} h & j \\ l & m \end{pmatrix} \frac{1}{\sqrt{2}} \begin{pmatrix} 1 \\ 1 \end{pmatrix} \right]^2 \\
 &= \frac{1}{4}(h^2 + j^2 + l^2 + m^2) + \frac{1}{2}(hj + lm) - \frac{1}{2}(hl + hm + jl + jm) \\
 &= \frac{1}{4}(j^2 + m^2) - \frac{1}{2}(jm) = \frac{1}{4}m^2 \rightarrow j = 0
 \end{aligned} \tag{5.13}$$

The only non-zero component is thus m , yielding a type of tensor which is not among the choice of Γ -point phonons in the symmetry groups D_{2h} and D_{4h} .

Returning to Fig. 5.12, we find that the polarization situation is reversed further into the UV. The spectra in (d) were acquired using partially polarized light of 4.82 eV (the polarization ratio was 6:1). The peaks at 150 and 580 cm^{-1} are stronger for incident and detected polarization perpendicular to the Cu-O chains than parallel to the chains. At 90 and 470 cm^{-1} , peaks are visible in both geometries. For the peaks at 580 cm^{-1} (defect-induced), 150, 330 and 480 cm^{-1} (Raman-allowed), we can find counterparts at the other excitation energies.

This reversal of anisotropic selection rules is in agreement with the anisotropy of the dielectric function and the RAS signal at 4.8 eV, which is reproduced as an inset for comparison. While the RAS signal has b polarized features around 2.2 eV and 4.15 eV, it displays a -polarization further in the UV. The signal strength of the Raman modes follows that of the anisotropy of the dielectric function over the entire spectral range, and seem connected to these electronic properties more closely than to the structural symmetry and vibrational eigenstates.

The photo-induced change of oxygen-vacancy activated Raman modes under resonant UV excitation at 4.1 eV is another example where the Raman signal follows the reflectance anisotropy. In Chap. 4 we have seen that the RAS spectra have a small resonance centered around 2.2 eV which is decreasing under illumination, while the UV resonance is increasing. The same is true for the defect-induced modes seen with the corresponding UV excitation energy: They grow under illumination. Figure 5.13 illustrates the situation with two Raman sequences at different excitation energies and the corresponding ranges in a RAS sequence reproduced in the inset. In contrast to the visible case, the growth under illumination is accompanied by a shift in frequency, which is strongest for the 590 cm^{-1} mode. A more detailed presentation of this phenomenon follows in section 5.5.4.

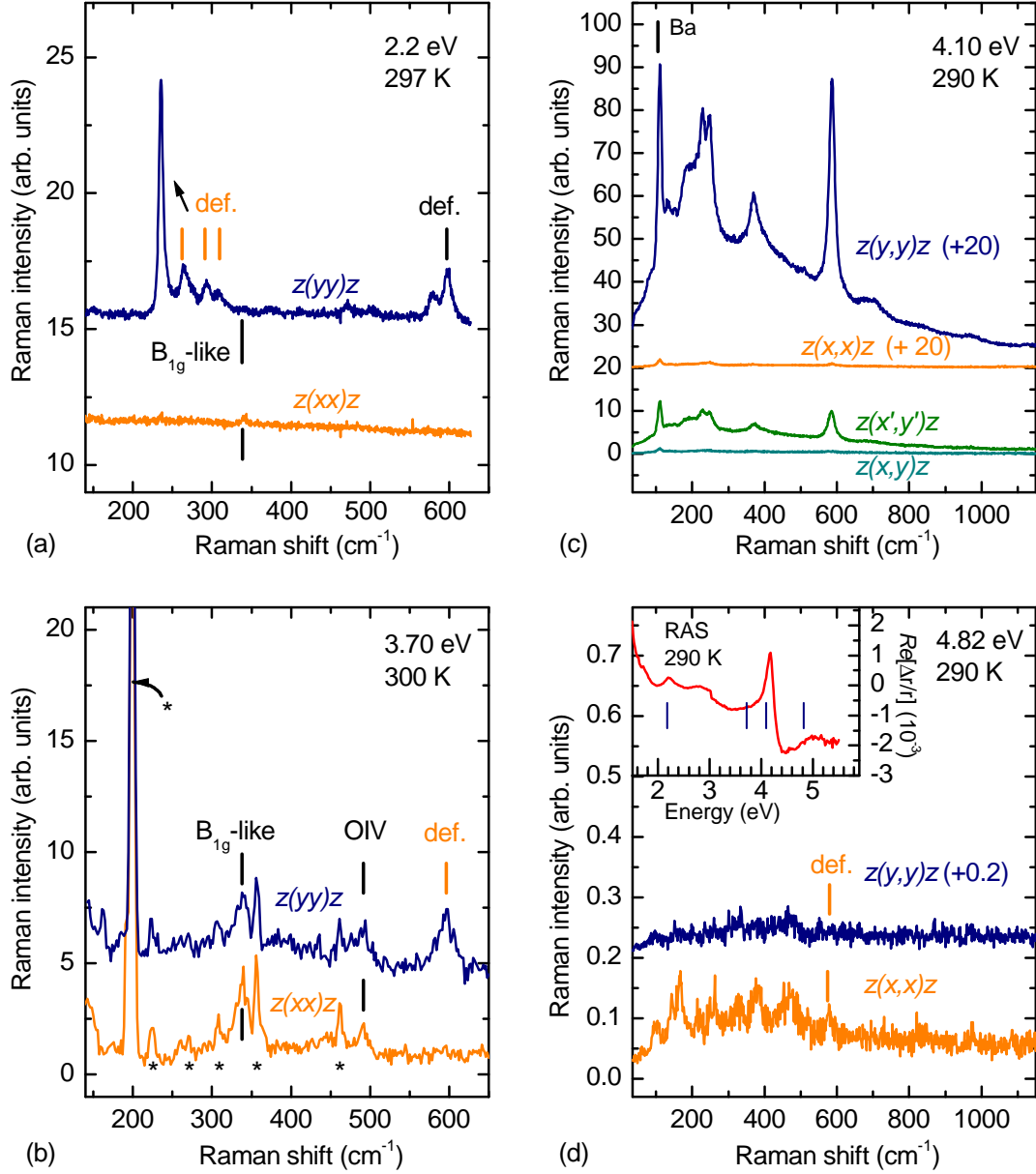


Figure 5.12: Selection rules of the oxygen-vacancy activated modes at different excitation wavelength. The modes are visible for incident and detected polarization along the b axis, except for $E_{exc}=4.82$ eV, where they show along the a axis and the RAS signal reproduced in the inset also has a pronounced peak in the a direction. Raman-allowed modes are indicated with black lines, defect-induced modes with orange lines. The stars in (b) mark plasma lines.

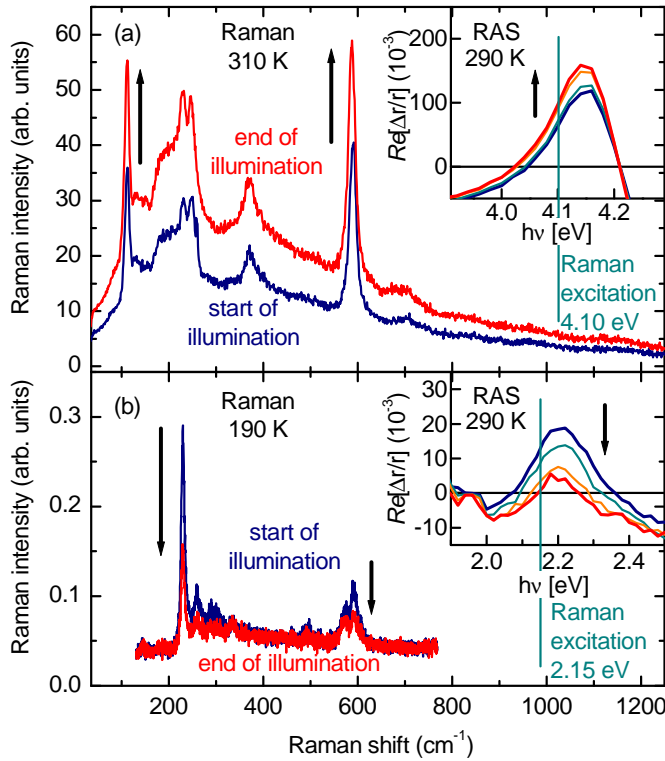


Figure 5.13: Illumination-induced change in the Raman spectra of $\text{YBa}_2\text{Cu}_3\text{O}_{6.7}$. (a) 4.10 eV excitation, beginning and end of 30 min illumination (b) 2.15 eV, 36 min. The insets show changes during a RAS illumination experiment. The arrows indicate the chronological direction of the sequences.

5.4.3 The temperature dependence of oxygen-vacancy activated modes

We now turn to the temperature dependence of the oxygen-activated modes at the two resonant excitation energies, starting in the visible. Raman spectra of an untwinned single crystal of $\text{YBa}_2\text{Cu}_3\text{O}_{6.7}$ and a twinned single crystal of $\text{PrBa}_2\text{Cu}_3\text{O}_{6.7}$ at various temperatures are shown in Fig. 5.14. While being very distinct at low temperatures, they change around 160 K into broader, washed out and smaller forms. At temperatures above 250 K the satellite peaks of the largest defect feature at 232 cm^{-1} become indistinguishable. Thermally induced oxygen hopping becomes active in that temperature range, indicating a connection. For $\text{YBa}_2\text{Cu}_3\text{O}_{6.7}$ the defect-related peaks are more pronounced at low temperatures and particularly weak around $T < 130\text{ K}$. In part, this is due to the different time constants for bleaching, as we will discuss in more detail in the next section. In the $\text{PrBa}_2\text{Cu}_3\text{O}_{6.7}$ spectra, the shape and number of peaks changes little with temperature; only the features at 264 and 576 cm^{-1} become more pronounced at low temperatures. Different intensities in the time integrated spectra of Fig. 5.14 are again caused by different decay rates. We supply selected peak positions and intensities versus temperature in Fig. 5.16(a) and (b) for completeness. As expected for decreasing bond length with decreasing temperatures, both Raman-allowed and defect-induced peaks harden.

Under UV excitation, the situation is different: In Fig. 5.15(a) all peaks decrease in intensity with decreasing temperature after Bose correction, which is uncommon for inelastic scattering on phonons (note that the offset of the spectra is reversed compared to Fig. 5.14). From temperature-

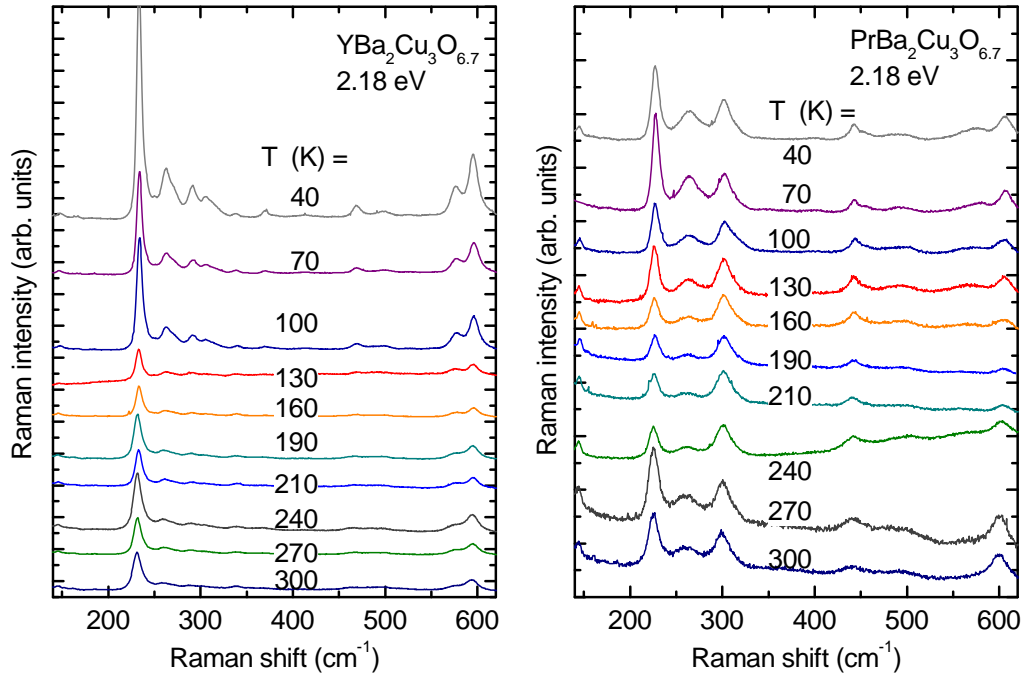


Figure 5.14: Temperature dependent Raman spectra taken at 568 nm on a $\text{YBa}_2\text{Cu}_3\text{O}_{6.7}$ and $\text{PrBa}_2\text{Cu}_3\text{O}_{6.7}$ single crystal. The integrated intensity increases at low temperatures, more strongly for $R=\text{Y}$ than for $R=\text{Pr}$.

dependent RAS experiments reproduced in (b) we can see that the 4 eV resonance sharpens and shifts to higher energies upon cooling. [84] Therefore, we conclude that the unusual decrease in Raman intensity is caused by detuning of the resonant condition and the excitation energy when the temperature changes. Though the resonance profile was not explicitly determined, we expect it to be comparatively narrow, with a steep shoulder on the low-energy side, from the pronounced intensity change induced by cooling. The existence of a narrow feature at 4 eV in ellipsometry data on $\text{YBa}_2\text{Cu}_3\text{O}_{7-\delta}$ supports this assumption. [75]

Although the spectra in Fig. 5.15 were offset by a constant amount, a gap is visible between 230 and 250 K. It results from the illumination-induced increase in the Raman cross section during the accumulation time, which is much more efficient at high temperatures under UV excitation. Figure 5.15(c) shows a comparison of the intensities of two modes after 30s accumulation time (open symbols) and after 30 min accumulation time (full symbols). Upon cooling, the peak intensities decrease to a different extend, indicating independent coupling constants to the resonant electronic excitation. For example, the Ba-mode is smaller at room-temperature, but equals the 590 cm^{-1} peak at 20 K. The photo-induced change at high temperatures also affects the peaks differently, adding to the difference in intensity. Figure 5.16(c) shows the position and peak width versus temperature. Different from the visible where only the intensity changes, the width and the position are also affected by illumination.

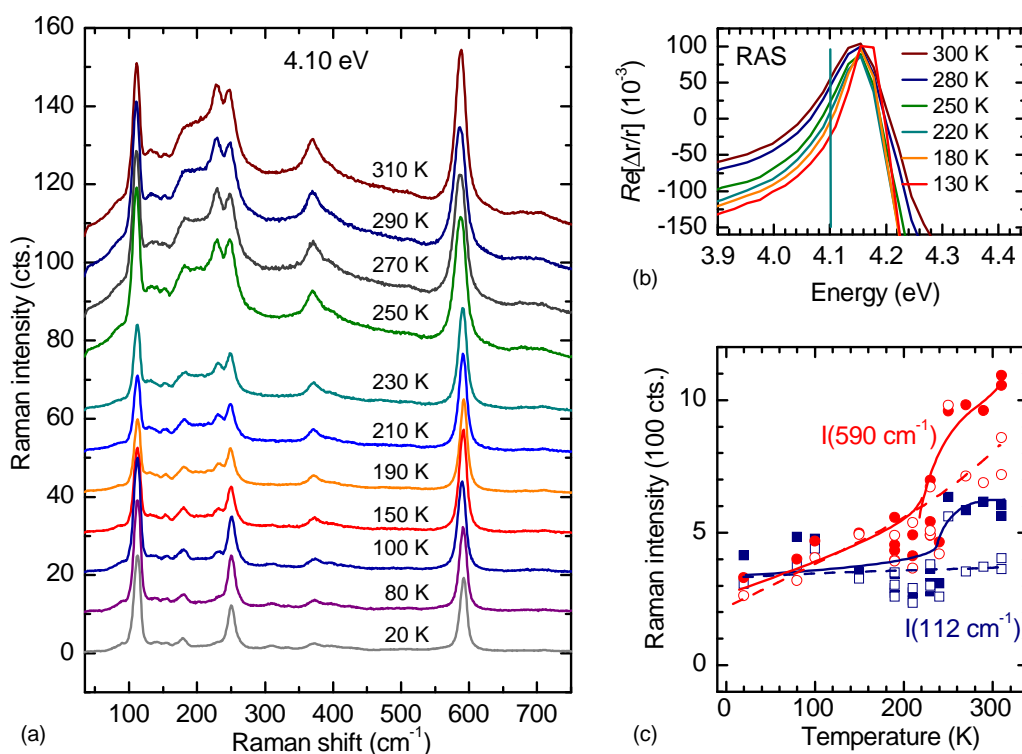


Figure 5.15: (a) Temperature dependent Raman spectra taken with 302 nm excitation on a $\text{YBa}_2\text{Cu}_3\text{O}_{6.7}$ and single crystal. In contrast to the visible case, the Raman intensity decreases at low temperatures. Note that the direction of the offset is reversed with respect to Fig. 5.14, with the high-temperature spectra at the top. (b) Temperature dependent RAS signal around 4.1 eV. The anisotropy-peak shifts and narrows at low temperatures, causing detuning of the resonance condition. (c) Fitted peak area at 112 and 590 cm^{-1} . The peaks equal each other at 20 K, but increase differently with temperature. Above 250 K, the peaks increase with illumination time, giving different results after 30 s and 30 min integration time of the spectra.

5.4.4 Origin and mechanism of activation

An open question is the origin of the defect-induced peaks and the mechanism of their Raman activation. From the fact that they vanish for fully oxygenated compounds and that the oxygen vacancies occur in the chain planes of the unit cell, we take it for certain that the vacant chain oxygen sites are central to their appearance. Since this structural defect can change the selection rules either by breaking the symmetry or via the connected resonant electronic excitation, the suggestions for the mechanism are numerous.

A large number of modes on top of a broad background appear in the Raman spectra at two specific resonant excitation energies (2.2 and 4.1 eV), in both cases exclusively for polarization along the Cu-O chains. The most pronounced peaks under visible excitation at 231 cm^{-1} and at 590 cm^{-1} have reversed intensities in the UV. The spectra also show peaks which are unique to

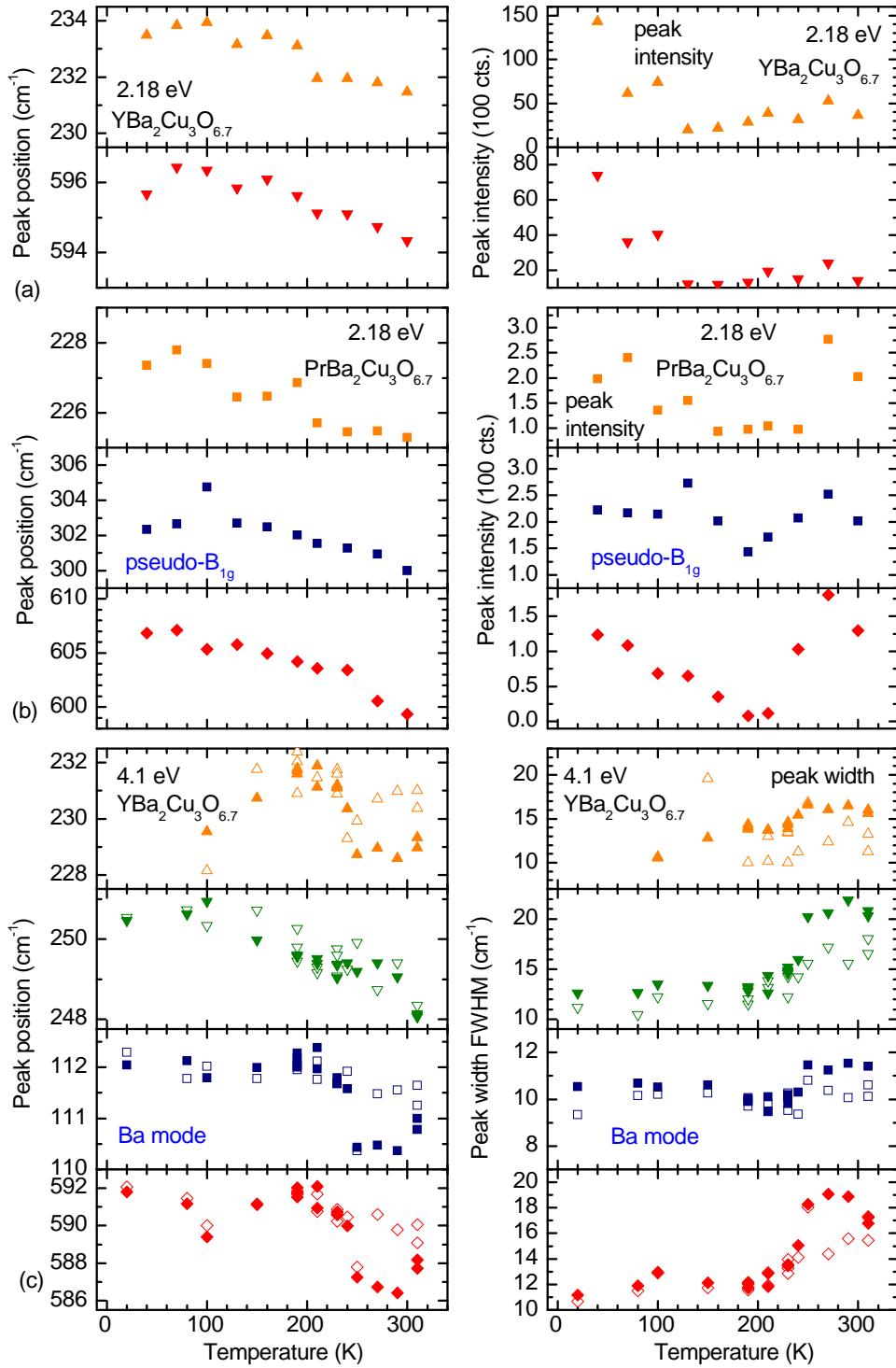


Figure 5.16: Position (left panels) and intensities or peak width (right panels) versus temperature. Values taken from Raman spectra under visible and UV Raman excitation in Figs. 5.14, 5.15 using Lorentzian fits. (a) 2.18 eV, $\text{YBa}_2\text{Cu}_3\text{O}_{6.7}$, 2 h accumulation time (b) 2.18 eV, $\text{PrBa}_2\text{Cu}_3\text{O}_{6.7}$, 2 h accumulation time. (c) 4.10 eV, $\text{YBa}_2\text{Cu}_3\text{O}_{6.7}$, full symbols correspond to spectra accumulated for 30 min, open symbols to spectra accumulated for 30 s.

each resonant excitation. Table 5.6 contains a synopsis of the frequencies of defect-induced resonant modes, while the Raman-allowed and infrared-allowed phonons were summarized in Tab. 5.1 in a previous section. Comparison shows that the defect-induced peak positions match neither the Raman-active, nor the infrared-active vibrations at the Γ -point, so they are either strongly renormalized, or they stem from other parts of the Brillouin zone. The broad background may contain more phononic features, or be a signature of electronic scattering. The polarization selection rule and the photoinduced change match the reflectance anisotropy of the underdoped compound.

One early idea for the mode assignment were chain-end vibrations. [60, 63] On either side of a vacant oxygen site in the chain plane open chain fragments exist, which can have localized vibrations that are not subjected to the symmetry constraints of the solid. From the heavy Cu-atom at the chain end we expect a low vibrational frequency, from the much lighter O-atom next to it a high frequency, which matches the two groups of peaks found around 230 and 600 cm^{-1} . The satellite peaks are in this picture due to variations of the local structure: A monomer, that is a single O atom between to Cu atoms, will be different from the end of a long chain. The surrounding local configuration will influence the vibrational frequency. Against this picture, however, speaks the dependence of the vacancy-activated peaks on oxygen content (see Fig.5.10). If different peaks were due to different chain length, they should swap intensity in heavily underdoped samples, since the number of monomers must exceed the number of long chains at one point. There is, however, no independent intensity change discernable in the Raman sequences of Figs. 5.7 and 5.8.

Another interpretation is based on the symmetry argument. [97] The CuI and OI chain atoms are both at inversion centers of the unit cell. As explained in Sec. 5.1, this means that their vibrations are odd and therefore infrared active and Raman forbidden. Due to the vacancy, the inversion symmetry is lost and the chain-vibrations become Raman active. Moreover, the $k = 0$ rule does not apply anymore and the phonon dispersion branches (partly) fold onto the Γ -point, showing as a density of states. This picture can explain the number of peaks as well as the dependence on oxygen concentration: On the one hand, defects are necessary for the activation, but on the other hand, the vibrations vanish along with the chains that host them at very low oxygen content. Chain vibrations as the only orthorhombic feature in a near tetragonal structure are also the phonons of which in-plane anisotropic selection rules could be expected. The common dependence on illumination follows naturally from the assumption that the signal is basically the phonon density of states.

The third possibility put forward is the resonance. [58,59] As was mentioned very briefly in the introductory section of this chapter, selection rules can be different in the case of resonant enhancement. Especially polar phonons can couple via their net charge fluctuation (Fröhlich interaction) and so become active. This picture is supported by the close connection between the Raman signal and the anisotropic electronic resonance studied with RAS. The electronic states involved in the resonance are connected to oxygen vacancies. In this picture, the observed polarization depen-

dence of the activated peaks originates from the symmetry of the electronic transition, screening the Raman tensor of the coupling phonon. It then remains an open question by which criteria the coupling phonons are chosen.

In this context, the assignment of the mode at 594 or 590 cm^{-1} may be questioned. In the majority of work reported, the assignment was to the chain-oxygen vibration along the bond. [62, 66] The short bond justifies the high frequency, and it turned out from early shell model calculations by Kress *et al.* accordingly. [65] Moreover, in a site-selective oxygen-isotope substitution experiment the 600 cm^{-1} shifts at the same substitution level as the apical mode, and not with the pseudo B_{1g} . [66] This is a clear sign for its connection to the apical or the chain oxygen atom, which are more easily substituted in diffusion experiments than the oxygen atoms of the superconducting planes. [15, 99, 100] As was explained in Sect. 5.2, the related compound $\text{YBa}_2\text{Cu}_4\text{O}_8$ the chain vibrations are Raman active, because the site on the double chain do not occupy centers of inversion. Apart from five A_g modes at positions similar to those in $\text{YBa}_2\text{Cu}_3\text{O}_7$, two additional peaks in the spectrum were found at 250 and 605 cm^{-1} and assigned to the CuI and OI vibrations, supporting the original assignment of the 600 cm^{-1} defect-induced peak. [94]

However, more recent calculations based again on the shell model [107] and on ab-initio calculations [67] place the OI vibration at lower energies (around 485 cm^{-1} in Ref. [67]), which is in agreement with the assignment of some infrared modes. [115] They leave only oxygen vibrations in the superconducting planes for an assignment of peaks above 70 meV (565 cm^{-1}). Ab-initio calculations on $\text{YBa}_2\text{Cu}_4\text{O}_8$ also disagree with previous assignments: They claim that the apical vibration is pushed up to 607 cm^{-1} , and the chain-oxygen is the one at 500 cm^{-1} . [95]

To resolve the apparent contradiction with the isotope substitution experiments, the eigenvector of the mode requires a significant out-of plane contribution, either from the apical or the chain oxygen site. Raman experiments on underdoped, site-selectively isotope-substituted compounds could resolve this issue. Another way to check the 600 cm^{-1} -assignment is Raman spectroscopy on the chain-free insulating compound $\text{YBa}_2\text{Cu}_3\text{O}_6$ in resonance with the 4 eV excitation.

Assuming that the peak is, in fact, due to an oxygen vibration in the superconducting planes, two interesting conclusions follow. Firstly, oxygen-vacancy activated phonons need not be directly chain related, other vibrations can couple to the resonance. For these, however, we cannot deduce orthorhombic character from the eigenvectors, which contradicts the idea of a phonon density of states of chain vibrations. Secondly, its prominent appearance as an oxygen-defect induced peak indicates that the in-plane oxygen modes couple strongly to anisotropic electronic excitations, which exclusively exist in oxygen-reduced compounds. The excitations are related to defects localized next to lone chain Cu atoms, and are as such not included in the present theoretical descriptions. Neutron scattering yielded an anisotropic renormalization of the dispersion of in-plane oxygen vibrations in underdoped $\text{YBa}_2\text{Cu}_3\text{O}_{6.6}$. [106] The strong Raman resonance suggests that coupling of phonons to defect-related electronic states contributes to the anisotropic phonon-dispersion in the *ab*-plane.

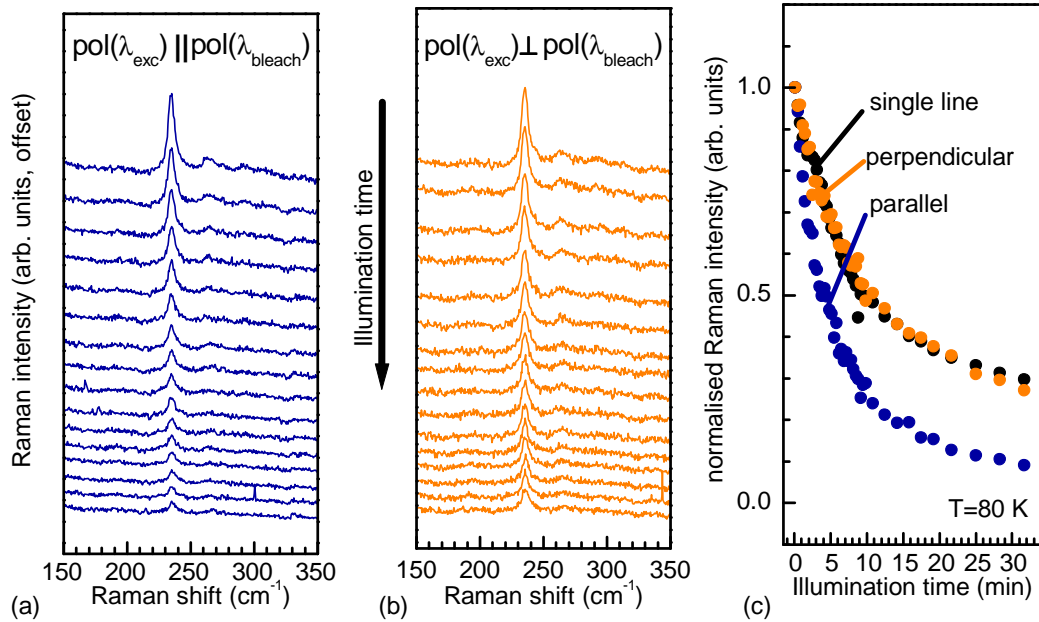


Figure 5.17: Raman spectra taken on a $\text{YBa}_2\text{Cu}_3\text{O}_{6.7}$ single crystal at 2.18 eV in $z(y,y)z$ geometry, 5 mW, 80 K. A second laser beam is focussed on the same spot (2.54 eV, 5 mW). In (a) its polarization is parallel to the Raman excitation, in (b) it is perpendicular. (c) Decrease of Raman intensity of the mode at 231 cm^{-1} versus illumination time extracted from the spectra in (a) and (b) and from an experiment without the second laser.

In summary, though the discovery of the UV resonance substantially widens our perspective on the oxygen-vacancy activated peaks, their assignment is not entirely conclusive, making site-selective isotope-substitution studies necessary. Considering the fact that the entire set of detected peaks does not coincide with the Γ -point phonons we conclude that phonons from other parts of the Brillouin zone become active due to the absorption of quasi momentum by the abundant oxygen defects. The activation is caused by resonant coupling to the electronic defect states, which are in-plane anisotropic and dominate the scattering. This indicates a strong electron-phonon coupling to the defect states. Calculations of the Raman resonances would be interesting, but are hampered by the fact that the irregular defect-sites play the central role in the resonance.

5.5 Photoinduced change in Raman and oxygen-vacancy reordering

In this section we present results on the time-dependence of the oxygen-vacancy activated peaks in the Raman spectra. As was explained in detail earlier in Chap. 3 and Chap. 4, the observed change can be attributed to the decrease of short chain fragments in favor of longer chains during the development of superstructure patterns. The process is then analogous to the thermally determined process of reordering during room-temperature ageing of underdoped samples, but triggered by the

excitation of oxygen atoms through light. Here we will discuss the Raman dynamics within this picture. We show that the effect is polarization dependent, and that it quickens when the unit cell is enlarged in compounds with larger rare earth ions. An advantage over the reflectance anisotropy is that the low temperature regime, where thermal reordering is frozen and photo-induced change occurs and is metastable, is more easily accessible. The temperature dependence of the effect is probed and compared to reordering dynamics obtained from a Monte Carlo study using the asymmetric next nearest neighbor Ising model described in Chap. 3. The case of UV excitation is in some aspects different from the visible situation and will be discussed at the end of this section.

5.5.1 The influence of polarization: Two-color Raman bleaching

Different from other methods such as electrical transport or reflectance anisotropy, the photo-induced change cannot be separated from the observance of the corresponding modes in the Raman spectra, since they are in observed and changed by the same light. Difficulties arise whenever statements about intensity comparison (and in the UV excitation case even position) are sought, restricting reliable comparisons to spectra within one illumination sequence. This problem was a motivation for the reflectance anisotropy studies.

The two-color study shown in Fig. 5.17 was performed in order to analyze the polarization dependence of the bleaching effect in visible Raman. [116] As we saw in the previous section, the selection rules of the defect-induced modes are anisotropic in the ab -plane, with the modes visible exclusively for light polarized along the b -axis of a crystal. In a sequence of Raman spectra taken with the appropriate scattering geometry $z(y,y)z$ they diminish, as is seen in Fig. 5.17(a) and (b). The task was to find out if the underlying change in the system is also polarization dependent, without changing the scattering geometry for the Raman detection. To this end a second laser beam with independent polarization (and different wavelength, $\lambda_{bleach}=488$ nm) was focussed and carefully overlaid with the Raman spot. In Fig. 5.17(a) its polarization was along that of the Raman light source ($\lambda_{exc}=568$ nm), in (b) it was perpendicular. In addition, the experiment was repeated on a fresh spot without the second laser. The photo-induced change was reported to scale linearly with the total photon dose on the sample, [11, 59, 61] so we expect faster bleaching for more illumination power. We chose the strongest oxygen-vacancy activated mode at 231 cm^{-1} to follow the change and extracted its intensity using a Lorentzian fit. Figure 5.17(c) shows the intensity versus illumination time for the three cases. The decrease is faster for the two light sources polarized parallel to each other and to the chain direction b , while the curve for perpendicular configuration falls onto that of the single laser experiment. Evidently, light polarized perpendicular to the chains does not take part in the process of photo-induced change. This is in agreement with the findings in reflectance anisotropy, where the effect also proved to be polarization-dependent and indicates that the reordering of oxygen atoms is triggered by an excitation which is connected to, or identical with the resonance activating the modes. A more technical aspect of the experiment is that it excludes the influence of heating caused by the laser focus as possible origin for Raman bleaching, since heating would not be polarization dependent.

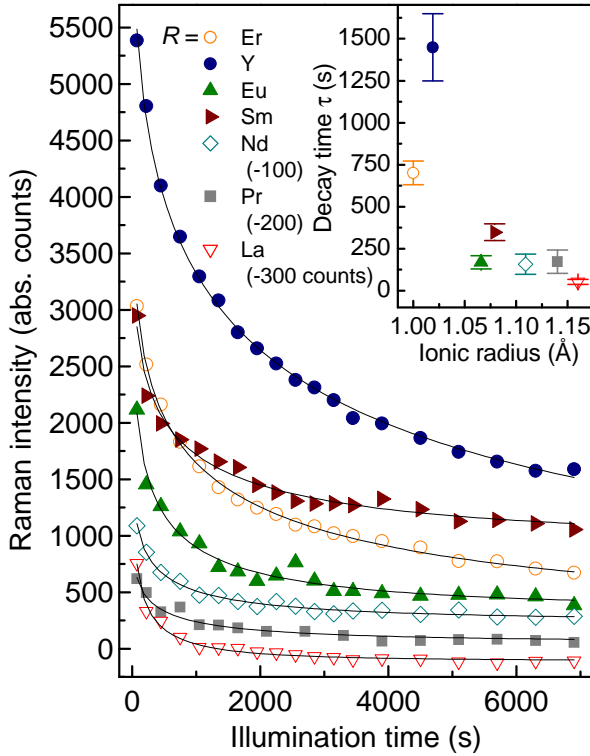


Figure 5.18: Intensity of the peak at 230 cm^{-1} over illumination time for ceramic samples of $\text{R}\text{Ba}_2\text{Cu}_3\text{O}_{6.7}$. For clarity, the lower three curves were offset by the amounts given in the legend. The fits were performed using a stretched exponential law with a common exponent $\beta = 0.36 \pm 0.04$ for all data sets. The inset shows the relaxation time τ depicted versus the ionic radius of R .

5.5.2 The influence of the bond-length: Raman bleaching in compounds with different rare earth atoms

The fact that the oxygen-vacancy activated peaks appear in all oxygen-reduced compounds of the $\text{R}\text{Ba}_2\text{Cu}_3\text{O}_{7-\delta}$ -family can be utilized for a systematic study of the bleaching dynamics in systems with varying cell size. Along the row of the rare earth elements in the periodic table the ionic radius decreases systematically with increasing atomic number when inner shells are filled up. As already illustrated in Fig. 5.4, Raman-allowed as well as defect-induced modes shift in frequency, when the ionic radius of the rare earth atom in the unit cell center changes, because the dimensions of the entire cell change, mainly the length of the a and b axes. In terms of the oxygen vacancy reordering model, we expect a change in the dynamics stemming from different diffusion or “hopping” barriers for the oxygen atoms in the chain plane.

We studied the time dependence of the defect-induced Raman modes under visible excitation (2.18 eV) at 80 K in a set of samples with $R = \text{Y, Er, Eu, Sm, Nd, La, Pr}$, including again $R=\text{Pr}$, the only non-superconducting variation of $\text{R}\text{Ba}_2\text{Cu}_3\text{O}_{7-x}$. The intensity of the strongest defect-induced mode at this excitation energy was traced and the results displayed in Fig. 5.18. There is a clear dependence of the initial intensity and the bleaching dynamics on the ionic radius: While for the smaller ions like Er and Y the initial intensity is high and the bleaching slow, the samples containing ions with larger radius like La and Pr show low initial intensities combined with a very steep drop in the first stages of the illumination and levelling later on.

Though simple exponential decay functions have been used to describe the Raman-intensity decrease before, they clearly do not fit our data. [59] To find another quantitative description for our decay law, we applied a so-called stretched-exponential or Kohlrausch function, which had been used for persistent photoconductivity data before: [49, 50]

$$I(t) = I_0 \exp \left[- \left(\frac{t}{\tau} \right)^\beta \right] + \text{const.} \quad (5.14)$$

This Kohlrausch law is applied to the relaxation processes in disordered, amorphous or complex systems such as glasses and highly doped semiconductors and can be traced back theoretically to a distribution of relaxation constants [117]. In this scenario, τ is interpreted as a relaxation time similar to those in the usual exponential decay laws, while the exponent β is related to the width of the distribution of relaxation times, and so to the degree and type of disorder. β runs between 0 and 1, where 1 corresponds again to a δ -distribution of time constants τ , that is to the simple exponential case. Although this approach is heuristic and not too much emphasis should be put on detailed physical conclusions from the fit parameters, β can be interpreted as an indicator for the disorder in the chain oxygen pattern, which is frozen in during the temperature quench.

Since we treated all samples alike in the quenching procedure, a common value of β would be in good agreement with the type of disorder suggested. In fact, fits to the data sets of the individual samples yielded similar values for the exponent, though in some cases ($R=\text{Sm}, \text{Pr}, \text{La}$) with high statistical uncertainties. Taking β to be the same for all data sets (but variable) we can fit our results with $\beta = 0.36 \pm 0.04$ and τ and I_0 as given in Table 5.7. The fits are also shown in Fig. 5.18 and describe the data well. In contrast to the exponent β , the decay constant τ does depend on the rare earth atom, matching the first impression of the development of Raman intensities. It is depicted versus ionic radius of R in the inset to Fig. 5.18. Within the oxygen reordering model, this quickening indicates a decrease in the activation energy which is necessary for the diffusion of the oxygen atoms, speeding up their reorganization within the planes of the chains.

We now turn to the difference in initial amplitude observed in Fig. 5.18. Among the reasons for this difference the possible detuning of resonant conditions with changing rare earth was already mentioned in the previous section. A more “technical” aspect is connected to the sample

$R\text{Ba}_2\text{Cu}_3\text{O}_{6.7}$	exponent $\beta = 0.36 \pm 0.04$	
R	initial intensity I_0	decay constant $\tau(\text{s})$
Er	4400 ± 400	700 ± 70
Y	7400 ± 500	1400 ± 200
Eu	3700 ± 400	170 ± 40
Sm	3400 ± 300	350 ± 50
Nd	1900 ± 300	160 ± 60
Pr	1200 ± 100	170 ± 70
La	2700 ± 300	50 ± 15

Table 5.7: Fit parameters for a stretched exponential function. We performed a simultaneous fit with a shared (but variable) exponent β for all data sets.

preparation: Since the intensity of the defect modes strongly depends on the exact oxygen content of the sample, the apparent systematics in the initial amplitude could reflect that of oxygen diffusion for different rare earths. Another intrinsic effect to Raman bleaching is that the intensity can only be extrapolated back to zero illumination, since the accumulation of the first spectrum requires a finite amount of time (here 5 min, in the single crystal sequences 30 to 60 seconds). Different time constants of Raman bleaching therefore lead to differently integrated intensities in each accumulation period.

In the light of this work, explaining persistent photo conductivity and Raman mode bleaching could run as follows: During the temperature quench, a state of disorder in the distribution of oxygen atoms in the Cu-O-chains becomes frozen, when the relaxation times for reaching a new energetically more favorable state grow much longer than the inverse cooling-rate. This assumption matches the complicated structural phase diagram and corresponds well to the results of Nagel *et al.*, who found a glass-like transition in the thermal expansivity of oxygen deficient material upon cooling at about 280 K. [38] The system is left in a disordered state, in which neither the total energy nor the doping level of the superconducting planes is at optimum. The number of defects, that is, open chain ends, are large right after the quench. Illuminating the sample in this state provides the activation energy for the oxygen atoms to change site. During this induced diffusion the energetically favorable superstructures form, increasing the doping level and the average length of the chains. [40] The dynamics of this process will likely be described similar to a relaxation in a glass, for which laws of the stretched exponential type are appropriate.

5.5.3 Oxygen reordering dynamics in temperature-dependent Raman bleaching

In order to obtain a more detailed criterion for the comparison of oxygen-vacancy reordering to photo-induced Raman bleaching we now turn to the temperature dependence. The Monte Carlo simulation based on the asymmetric next-nearest-neighbor Ising model that we have introduced in Chap. 3 was adapted from a model describing the structural phase diagram. The reordering of vacancies into chains and superstructure patterns is governed by thermally activated processes. Once the interaction parameters for neighboring atoms have been set for a particular simulation, the oxygen concentration and the temperature are the only parameters which determine the motion of individual atoms and the equilibrium pattern. While thermally-activated superstructure-development freezes out soon below room temperature, the photo-induced bleaching of Raman-intensity under visible excitation does not. It exists down to the lowest temperatures investigated, the change remains stable after illumination below the room temperature annealing regime, and its velocity has a distinct temperature dependence. [11, 59] In a temperature range between 40 and 300 K we find that the bleaching slows down on cooling, displaying a pronounced change in dynamics around 160 K for $R=Y$. As was described in Chap. 3, we added to the model rules for the available sites and an energy barrier for a change, to obtain a dynamic description and to account for the thermal freeze out. The temperature is a free parameter in this simulation setup. In this section the

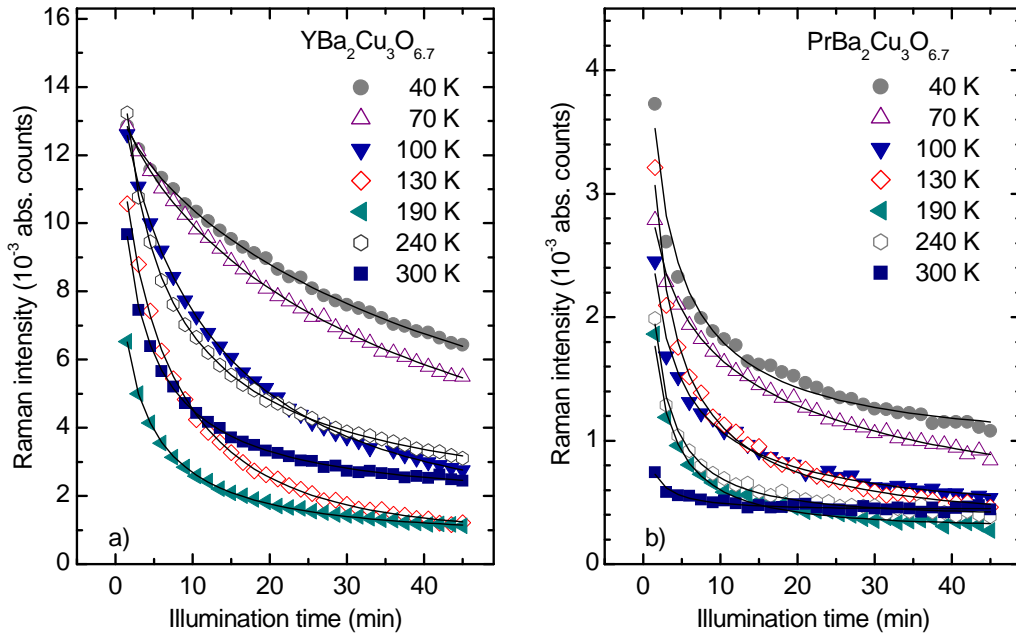


Figure 5.19: Decrease of the Raman intensity of the peak at 232 cm^{-1} in an untwinned $\text{YBa}_2\text{Cu}_3\text{O}_{6.7}$ (a), and at 228 cm^{-1} in a twinned $\text{PrBa}_2\text{Cu}_3\text{O}_{6.7}$ (b) single crystal under illumination for various temperatures. Solid lines are fits with Eq. 5.14; for fit parameters see Fig. 5.20.

development of chain fragments in a simulation is compared to the results from the temperature-dependent experiment. We chose visible resonant Raman excitation (2.18 eV) for this study, and expect no significant shift with temperature due to its broadness. The small sharpening of the resonance profile observed upon cooling should not interfere with the interpretation of Raman results in terms of vacancy-reordering dynamics.

Figure 5.19 shows results from temperature-dependent Raman spectroscopy on two single crystals of $\text{YBa}_2\text{Cu}_3\text{O}_{6.7}$ and $\text{PrBa}_2\text{Cu}_3\text{O}_{6.7}$. Similar to previous studies, the values were extracted from sequences of spectra taking the intensity of the largest defect-induced Raman-feature (at 232 cm^{-1} in $\text{YBa}_2\text{Cu}_3\text{O}_{6.7}$ and at 228 cm^{-1} in $\text{PrBa}_2\text{Cu}_3\text{O}_{6.7}$) and plotting it versus illumination time. Again, for a more detailed description parameters are extracted from the curves in Fig. 5.19 using a stretched exponential function. The fit parameters are given in Fig. 5.20, already together with parameters extracted from simulations, which will be explained later in this section. We note that a simple exponential function was used in a different Raman investigation on $\text{YBa}_2\text{Cu}_3\text{O}_{7-\delta}$ by Panfilov *et al.*, however, it does not describe our data well, as we clearly find $\beta < 1$. [59] A small value for β corresponds to curves with high initial steepness and flat asymptotic behavior compared to a simple exponential function. The decay times τ are displayed in Fig. 5.20(a), showing that the decay becomes much faster with increasing temperature. In case of $R=Y$, the decay times exceed the duration of the experiment (45 min) for the lowest temperatures investigated. The Raman

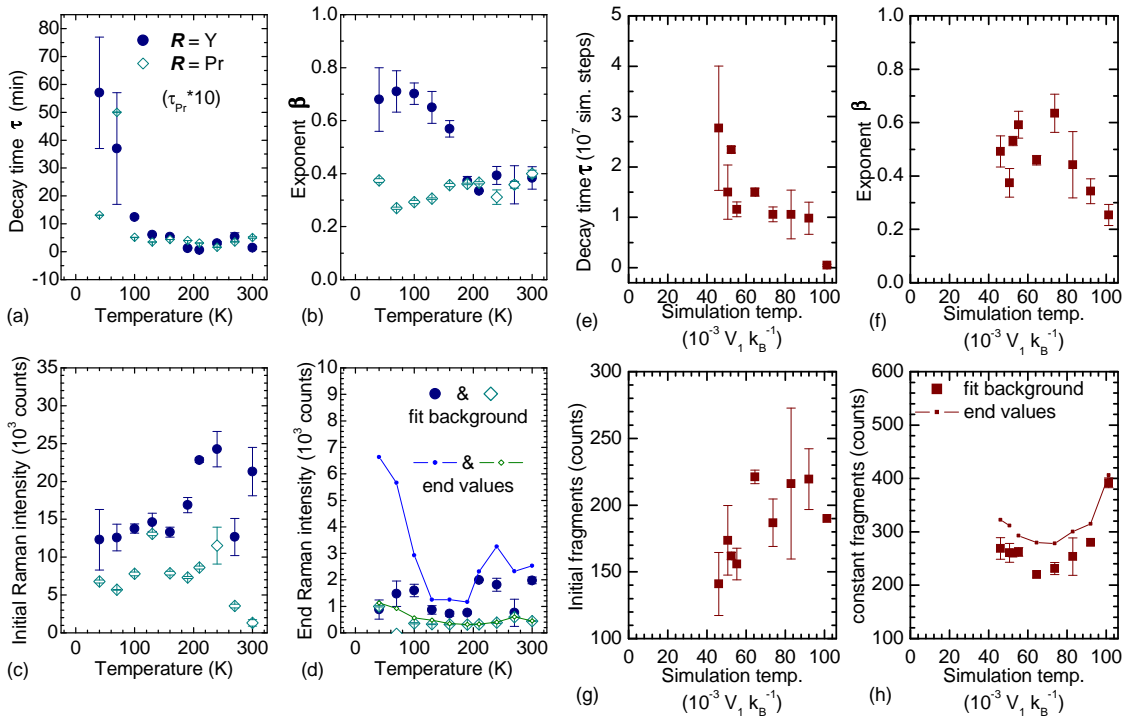


Figure 5.20: Left: Parameters from the fits in Fig. 5.22, full symbols correspond to $\text{YBa}_2\text{Cu}_3\text{O}_{6.7}$, open symbols to $\text{PrBa}_2\text{Cu}_3\text{O}_{6.7}$. (a) decay time τ , note that the values for Pr have been multiplied by 10, (b) exponent β , (c) initial intensity, (d) end intensity from fit and actual last value of the sequence (lines). Right: Parameters from fits with a stretched exponential function to the simulation data versus temperature. (e) decay time τ , (f) exponent β , (g) initial fragment number, (h) end fragment number from fit and actual last value of simulation (lines). In some of the simulation fits the background had to be fixed in order to achieve convergence of the fit (symbols without error bars).

intensity in $R=\text{Pr}$ decreases faster by an order of magnitude in comparison to Y, in accordance with our previous findings in an investigation on a set of samples with different R at fixed temperature. [97] It reflects that $\text{PrBa}_2\text{Cu}_3\text{O}_{6.7}$ has a considerably larger unit cell and is more tetragonal than $\text{YBa}_2\text{Cu}_3\text{O}_{7-\delta}$. Accordingly, the faster decay indicates lower barriers against oxygen hopping.

The exponent β is shown in Fig. 5.20(b). Interestingly, for $R=\text{Y}$ the type of the bleaching curves changes towards a steeper beginning and flattened end at temperatures above about 160 K, which is reflected in a pronounced change of β between two fairly constant values [0.70 and 0.35 (± 0.05), full symbols in Fig. 5.20(b)]. We found the same property in previous experiments on ceramic $\text{YBa}_2\text{Cu}_3\text{O}_{7-\delta}$ samples. [116] $\text{PrBa}_2\text{Cu}_3\text{O}_{6.7}$ [open symbols in Fig. 5.20(b)], in contrast, shows constant $\beta=0.35$ (± 0.05). It remains an open question whether $\text{PrBa}_2\text{Cu}_3\text{O}_{6.7}$ does not display a change in β at all, or the corresponding temperature threshold is below the reach of our investigation. The change of decay in that temperature range points to a change in the type of dynamics, or maybe to an energy barrier comparable to the thermal energy. Freezing temperatures for thermally activated oxygen hopping deduced from transport measurements and X-ray moni-

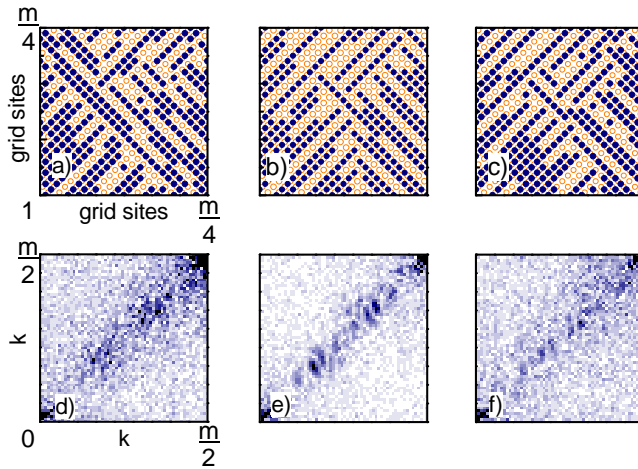


Figure 5.21: (a), (b) and (c) show parts of simulation matrices for $0.07 V_1/k_B$, before and after illumination, and after warming. (d), (e) and (f) display the corresponding 2D Fourier transformations, an increase of ortho-III pattern fractional peaks is observed in (e).

toring of the structural parameters are considerably higher (above 280 K [49]). We therefore conclude that illumination-induced oxygen hopping in $\text{YBa}_2\text{Cu}_3\text{O}_{6.7}$ is governed by a different, smaller energy barrier than thermally induced reordering.

The curves in Fig. 5.19 show that a slow decay at low temperatures is combined with high starting points in the first illumination time interval. We mentioned the different initial amplitudes in Raman spectra with identical accumulation time earlier. This behavior is a consequence of the finite accumulation time of 90 s for the first spectrum of a series. In contrast, the initial intensities extrapolated from the fits [Fig. 5.20(c)] are roughly constant, showing even a slight increase towards higher temperatures for $R=Y$.

The high-temperature decay ends at higher values of peak intensity than some of the intermediate: the most efficient bleaching occurs at 190 K in our experiments. This is best seen in Fig. 5.20(d), where we put the background values (the constant in the stretched exponential fit equation) from the fits as well as the last data point of each set. A discrepancy between these two values indicates that the decay is far from equilibrium. A comparison emphasizes what is obvious from the decay times already: Most of the dynamics are completed within the experimental time span of 45 min. Only for the two lowest temperatures ($T < 70$ K) in $R=Y$ is the decay slowed down so much that large uncertainties of the fit-parameters result.

Simulation results

Having described the experimental findings, we summarize the consequences for the oxygen-vacancy reordering model as follows: The intensity of defect-induced Raman peaks can, quite independently of the actual activation mechanism, be a measure for the amount of disorder in oxygen deficient $R\text{Ba}_2\text{Cu}_3\text{O}_{7-\delta}$. At 2.18 eV resonant excitation, it is a measure of the number of short oxygen fragments, or “monomers”, which host the electronic transition. Illumination decreases the Raman intensity, indicating a development of longer full or completely empty chains at the expense of short fragments. This implies that light excitation enables oxygen diffusion in the

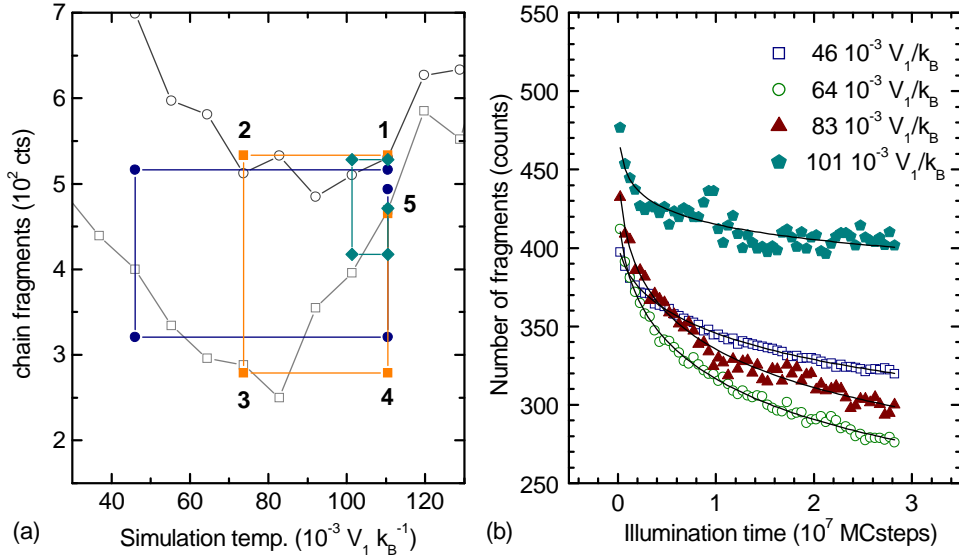


Figure 5.22: (a) Open symbols represent fragment numbers after simulation with zero barrier (open squares) and $E_B = 0.32V_1$ (open circles). Full symbols show simulation cycles for three different temperatures. The process of bleaching is modelled as a simulation run at a temperature of $0.11 V_1/k_B$ (point 1) and then quenching to lower simulation temperature (point 2). The energy barrier is diminished as a consequence of light excitation (to point 3), the stage which is compared to the bleaching and displayed versus simulation steps in (b). Finally, warming up again (point 4) enables relaxation (point 5). (b) Number of chain fragments in a 120×120 simulation for quenching temperatures between $1/6$ and full initial annealing temperature.

plane in a temperature region where thermally activated movement is frozen. At low temperatures, it is reasonable that the equilibrium state is more ordered than the frozen-in state from the high temperature configuration. However, the Raman decay shows a temperature dependence with the most efficient bleaching occurring at intermediate temperatures, indicating a non-monotonic, more complex dynamical dependence. These conditions determine the details of the simulation of chain fragments in a two dimensional grid, which we set up for comparison in Chap. 3.

The experimental procedure has the following steps: Samples are equilibrated at room temperature in the dark and then quenched to a low temperature, where the bleaching experiment is conducted. The photo-induced change is stable after illumination. Afterwards, the sample is warmed back to room temperature where the photo-induced change relaxes. A simulation cycle must emulate the procedure accordingly, as is illustrated in Figs. 5.21 and 5.22. A matrix containing a fixed number of oxygen atoms is equilibrated, with an energy barrier enabled, at a temperature above the freezing point. It is then set to the lower temperature of choice. The energy barrier is disabled, and the following relaxation towards the new equilibrium is monitored in order to compare to Raman bleaching. The matrix is then set back to the initial temperature and the energy barrier raised. It evolves back towards the equilibrium state which corresponds to

this temperature. In Fig. 5.21, the stages of the matrix are displayed. (a), (b), and (c) show the real space positions of oxygen atoms in a Cu grid, (d), (e), and (f) show their corresponding 2d-Fourier transforms. At high temperature in (a) and (d), the matrix is at equilibrium, but the regular superstructure pattern shows up only weakly due to thermal disorder. After setting the matrix to low temperatures, a more regular OII pattern (full chain, full chain, empty chain) has developed after the chosen number of simulation steps in (b) and (e). At the end, the initial state is nearly recovered at the initial temperature in (c) and (f).

The same simulation cycle is displayed in terms of chain-fragment numbers in a matrix with fixed oxygen content in Fig. 5.22. Raman bleaching experiments at different temperatures are simulated by cycling the simulation matrix from steps one to five in Fig. 5.22(a). The final states reached for zero and finite energy barrier are reproduced from Chap. 3 for comparison (grey open symbols). We chose a value of $0.32 V_1$, matching the interaction parameters, to ensure that temperatures for which equilibrium is reached overlap with temperatures of superstructure-pattern development. Between stages two and three, the number of chain fragments of any length or direction is plotted versus simulation steps in Fig. 5.22(b).

Note that with the interaction values V_i of the literature there is no one-to-one match of the actual temperatures in the experiment. Moving the simulation cycle down to the appropriate temperatures is hindered by the critical slowing-down effect of the algorithm and would require much longer calculations. Similarly, we used only $0.32 V_1$ instead of a barrier of about 1 eV. The static model we adapted was calibrated using the phase diagram, providing a set of correctly related parameters for the structural anisotropy which is the driving force of chain development. The energy barrier deduced from the transport experiments is, however, an order of magnitude larger than the interaction energies and would freeze the simulation above the superstructure temperature range. Also, we do not impose a calibration of the time scale in the dynamical simulations, because this would require some independent information about the excitation rate and hopping cross section. However, we obtain a reasonable order of magnitude assuming an absorption rate in the experiment (laser power of 3 mW in a volume of 100 nm penetration depth times $(100\mu\text{m})^2$ spot size, 0.66 oxygen atoms on the OI sites per unit cell volume, time scale of the experiment of 1 h) and comparing it to the Monte-Carlo sampling (3×10^7 total simulation steps in a matrix of size 120, occupation 1/3). For the time scales to match one in every 10^2 photons would have to move an oxygen atom. However, we merely attempt a qualitative description of the effect of light and activation energies on the number of chain-fragments and relate it to the behavior of Raman signal decay. Even with this qualitative character our extension of the ASYNINI model provides an understanding of the experimental cooling-illumination-reannealing cycle and explains the form and temperature dependence of chain building, and therefore, Raman bleaching.

Figure 5.22(b) shows a good qualitative agreement between experiment and simulations at low temperatures. The curves display stretched exponential behavior and the most efficient bleaching is at intermediate temperatures. The functional form of the time dependence is a consequence of

the type of ordering process. In a situation with many short fragments and single atoms, the probability of reaching an energetically favorable place at a chain-end is high, so the initial decrease in fragment number is steep. Beyond the declining number of possibilities for a single atom to join a chain, the growing chains provide stable barriers which are not likely to be crossed, nor to be moved. In the ordering dynamics above room temperature these two different ranges of the type of ordering, building of chains at first and later growth of domains, were identified and described in terms of scaling laws. [32,36,118,119] The actual relaxation times are thus sensitive to the specific local distribution, and they are likely to increase along with the pattern being built, leading to an over-exponential slow-down of reordering. This characteristic corresponds to a deeply disordered system with a broad range of relaxation times, resulting in the typical stretched exponential decay as a function of time. [117] The observed freeze out then resembles a critical slowing down of the dynamics rather than a well-defined energy barrier for individual oxygen site hopping, which would be simply exponential ($\beta=1$). Thus, the form of the decay shows stretched exponential character resulting from the ordering characteristics without any further assumptions.

For a more detailed comparison, parameters from fits analogous to the experimental data have been included in Fig. 5.20. In (e) the decay times decrease rapidly with temperature, reflecting the exponential change of hopping probability for a single atom. The low-temperature slow-down prevents the development of equilibrium within the calculation length chosen, with an effect on the system similar to that of an effective energy barrier. The simulations resemble the results for the $\text{YBa}_2\text{Cu}_3\text{O}_{7-\delta}$ material in that there is a dependence of β on temperature [Fig. 5.20(b),(f)]. The agreement is expected to be better than for $R = \text{Pr}$, as the parameter set with the in-built anisotropy was chosen to match $R = \text{Y}$. The change of β could be shifted in temperature by including a second energy barrier against hopping of light-excited oxygen in the model, or by extending the length of the simulations. However, the constraints from the critical slowing down prevented us from further pursuing this aspect. An explanation for the end values [Fig. 5.20(d),(h)] also follows naturally: at high temperature the pattern changes faster, but the system is aiming for a less ordered equilibrium state. All end states remain far from the ideal schematic pattern (no fragmentation), so that a further reduction of fragments remains possible. The initial intensity and the background are remarkably similar to the Raman data.

One feature is not contained in the model: The observed bleaching at room temperature. We assumed light excitation to enhance the oxygen hopping rate at low temperatures. At room temperature, where we are already in equilibrium, switching off an energy barrier does not cause any further relaxation. In the simulations, illumination will therefore not change the order in the system. Room-temperature photoexcitation effects are, however, observed in Raman spectroscopy as well as transport experiments. [7] This could be taken into account by assuming that light excitation alters the equilibrium state of the entire system or enhances the probability of switching to a chain-site for individual oxygen atoms. The latter idea has been realized for comparison with transport experiments by Federici *et al.*, who have shown that the stretched exponential decay of

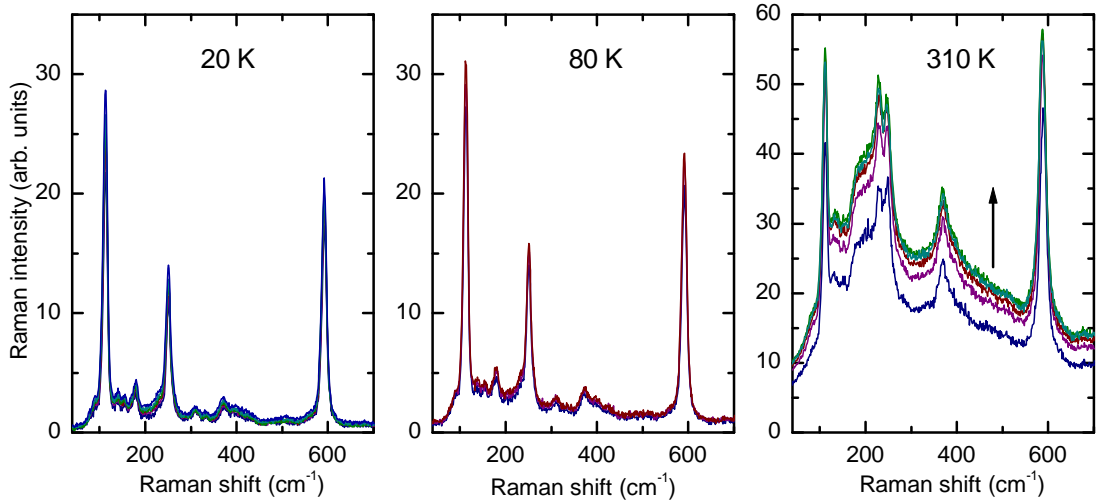


Figure 5.23: Sequential Raman spectra taken with 4.1 eV at 20, 80 and 310 K with 20 times 30 s accumulation time each. The arrow in the rightmost panel indicates the chronological direction. While the spectra overlay well at low temperatures, there is a strong growth with illumination at high temperatures.

illumination-induced change in transport experiments can be obtained using a cellular automata model. [120]

Summarizing, we have used the numerical model described in Chap. 3 to follow the dynamics of oxygen hopping to neighboring sites in a chain plane of $\text{YBa}_2\text{Cu}_3\text{O}_{7-\delta}$. The interaction energies are defined anisotropically, such that the lattice develops superstructure patterns of chains. For each temperature an equilibrium state exists, where pattern-building and thermally induced disorder are balanced. An energy barrier E_B causes the system to remain in non-equilibrium within the simulation time at sufficiently low temperatures. Light eliminates the barrier, reactivating oxygen hopping under illumination at low temperatures. At very low temperatures ($T < 40 \cdot 10^{-3} V_1/k_B$) critical slowing down sets in. A simulation cycle emulates the experimental cooling-illuminating-warming cycle, yielding a qualitative agreement with the functional form and temperature dependence. Thus, the assumption that light triggers reordering into superstructures in a system of frozen-in disorder is sufficient for a qualitative understanding of the observations. The simulations illustrate the changes induced in the material during low-temperature illumination and subsequent thermal annealing. The model and Raman results deviate for room temperature bleaching, which is not included in the description, but the general agreement between the model and experiment confirms the ability of oxygen-vacancy reordering to account for photo-induced effects in Raman spectroscopy on $\text{YBa}_2\text{Cu}_3\text{O}_{7-\delta}$.

5.5.4 Photoinduced change under UV Raman excitation

The strong resonance of oxygen-vacancy activated modes found at 4.1 eV is different from the Raman bleaching in several ways: First and most obvious, the signal is growing under illumination instead of decreasing. This is, however, in good agreement with the prediction from the reflectance anisotropy, which is also decreasing under illumination around 2.2 eV, but increasing at 4.15 eV. Second, the temperature dependence is different. As was discussed in the context of spectra taken at various temperatures in Fig. 5.15, photo-induced change is observed above 250 K only, while for visible excitation the most efficient temperature for the bleaching is at 190 K. Third, different peaks (Ba, 590 cm^{-1}) increase with different velocities, which was not observed for visible excitation. And fourth, the peak positions are affected by illumination.

Figure 5.23 shows sequentially taken Raman spectra at 20, 80 and 310 K. As was discussed before, the low temperature spectra are less intense than those at room temperature. The absence of illumination-induced growth at low temperatures is partly responsible, but the main reason is presumably a shift and narrowing of the sharp electronic resonance. Not all peaks decrease alike (see also Fig. 5.15), indicating independent coupling. In particular, the broad background is declining quickly towards low temperatures. While the spectra within the 20 K and the 80 K sequence are almost identical, there is a sharp rise during the sequence at 310 K.

The associated shift in frequency is illustrated in more detail in Fig. 5.24, where the first and last spectrum in of a 30 min sequence are shown along with the subtraction and the quotient of

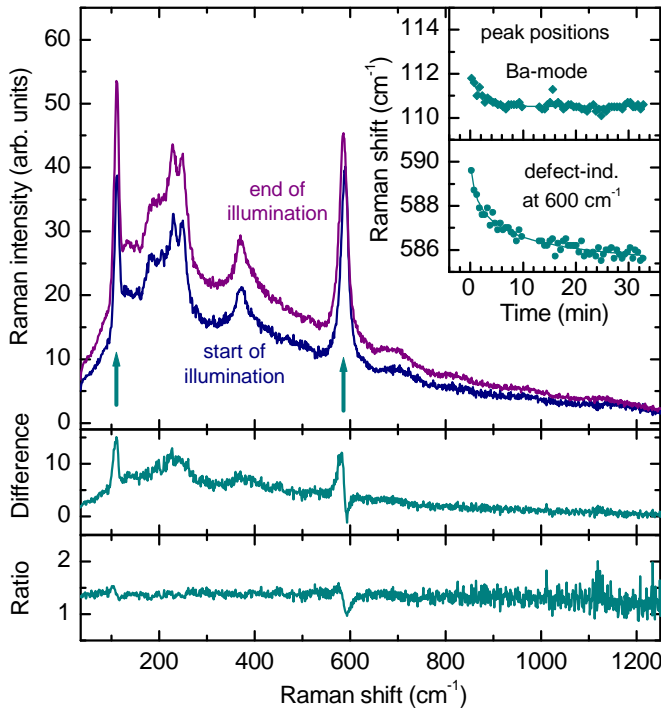


Figure 5.24: Raman spectra at the beginning and after 30 min illumination time taken at 4.1 eV and 290 K. The two lower panels show the difference and the ratio between the two. The inset shows the change of position For the Ba mode and the 590 cm^{-1} -mode.

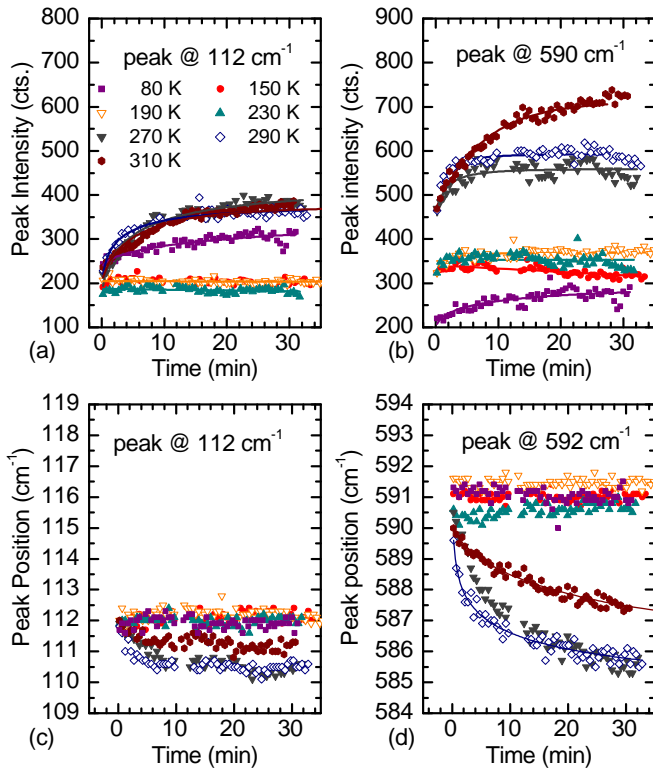


Figure 5.25: Time and temperature dependence of the peak-intensity and the peak position at 112 cm^{-1} and 590 cm^{-1} in sequential spectra taken with 4.1 eV excitation. The integrated spectra are shown in Fig. 5.15, and selected sequential spectra in Figs. 5.24 and 5.23. Different from the visible case, the modes grow under illumination, the position is affected, and the photo-induced change slows to a halt at low temperatures.

each other. The increase is essentially the same for all parts of the spectrum, but around the most pronounced peaks, the resonant Ba mode at 112 cm^{-1} and the mode at 590 cm^{-1} a shift leads to variations. Extracting these two peak positions from the sequence using Lorentzian line shapes gives the curves shown in the inset to Fig. 5.24. The peaks soften by 1.5 cm^{-1} for the Ba mode, and 4 cm^{-1} for the 590 cm^{-1} . It is impossible that this result reflects the change of the underlying phonon, since that should be detected under any excitation, even non-resonant cases for the Ba mode. Therefore, we assume that it is a renormalization effect and a Lorentzian fit does not give the bare phonon frequency. We also conclude that illumination then increases the doping via enhanced chain-fragment length, and the larger carrier concentration adds to the renormalization of the resonant phonons, possibly opening a way to the observation of the carrier density changes.

Alternatively, the activation mechanism combining a resonance with a defect could cause a similar effect. If the mode is activated by a double resonant process of the type found in graphite [121, 122] a slightly different k -vector is selected by each excitation energy. In our case, the excitation is constant. However, illumination can affect the energy difference of the electronic bands involved in the resonance, so that the resonant transition is tuned. This then results in phonons with slightly different k vectors singled out for activation.

Figure 5.25 shows the intensity growth during illumination for the Ba and the 590 cm^{-1} mode in panels (a) and (b), and the softening in panels (c) and (d). The curves confirm the general trend seen in the spectra. Those at 270 K and above show the change, while those at temperatures

of 230 K and below remain largely constant. An exception occurs at very low temperatures, the 20 K intensity curve again displays a slow increase. The position, however, does not shift at 20 K. Although the intensity and the frequency behave similar in general, there are deviations in some cases. For example, the most efficient change in frequency occurs at 290 K, while for intensity it is at 310 K. Considering the sensitivity of the resonant condition to temperature, we assume that the strongest illumination-induced changes alter the Raman cross section, which interferes with the analysis of the mode intensity versus time.

The fact that the temperature dependence is so different from the visible case is puzzling at first sight, because the oxygen-vacancy reordering model does predict changes down to very low temperatures, which are in a first approximation independent of the excitation wavelength. However, recalling the reflectance anisotropy data at 170 K (see Figs. 4.10 and 4.11 in Chap. 4) changes in the electronic anisotropy both around 2.2 eV and at the a polarized part of the anisotropic feature in the UV range, at 4.3 eV, do occur. Only the rising slope of the b polarized UV resonance at 4.1 eV is unaffected at this temperature, making 4.1 eV an unsuitable excitation energy for the detection of the change at low temperatures.

In conclusion, the Raman cross section, the temperature dependence of the peak intensity, the growth under illumination at this excitation energy, and the temperature dependence of the illumination-induced change are all in excellent agreement with the expectations from reflectance anisotropy spectroscopy. Thus, they match the oxygen-reordering picture. Of special interest for further detailed analysis are the frequency shifts observed exclusively at this excitation energy and their connection to the carrier concentration.

5.6 Summary

In this chapter we summarize the basic principles of the Raman effect and reviewed the dynamic analysis, the results for phonon-eigenvectors and dispersions, symmetry and Raman selection rules for the case of $\text{YBa}_2\text{Cu}_3\text{O}_{7-\delta}$. On this basis we analyze the properties of resonant defect-induced peaks occurring in the oxygen-deficient compounds. The fact that these oxygen-vacancy activated modes change under illumination is utilized to study the persistent photo-induced change in $R\text{Ba}_2\text{Cu}_3\text{O}_{7-\delta}$ and discuss its properties within the framework of the oxygen-vacancy reordering model.

The modes are found in all compounds of the $R\text{Ba}_2\text{Cu}_3\text{O}_{7-\delta}$ -family investigated, including the non-superconducting $R=\text{Pr}$. Their dependence on oxygen-concentration is confirmed, with the maximum intensity in the oxygen phase diagram range displaying the complex superstructures around 6.7. The drop towards lower oxygen concentrations is less steep in our data than previously reported. It can be due to the vanishing of the Cu-O chains hosting the corresponding vibrations, but more evidence points to the idea that their visibility changes because of the shifting and vanishing of the electronic resonance around 2.2 eV. Studies on the Raman resonance profile

are suggested to finally resolve this issue.

In addition to the known resonance in the visible, we found an exceptionally strong Raman resonance in the UV range at 4.1 eV. Its existence was predicted by the corresponding peak in the electronic in-plane anisotropy in underdoped compounds, which is assigned to an intraionic transfer in the Cu atoms of the chain-plane with some contribution of a transfer from Cu to Ba. [79] Indeed, the Raman-allowed Ba mode is among the peaks with resonant behavior. We suggest a coupling to defect-induced electronic states as a possible mechanism for the *ab*-anisotropy of the phonon dispersion in underdoped compounds. [106] The fact that the oxygen-vacancy activated modes decrease under visible Raman excitation, but increase when viewed with UV excitation, is in excellent agreement with the change of the electronic in-plane anisotropy observed.

The selection rules are also sharply anisotropic in the plane. The modes appear exclusively for polarization along the chain direction *b* around 2 eV and at 4.1 eV, but reverse sign deeper in the UV range at 4.82 eV. Thus, they follow the sign of the electronic anisotropy in the entire spectral range. Raman tensors of this form are not contained in the Γ -point group of the material, nor can the numerous peak positions be matched to the normally weak B_{2g} or infrared active odd Γ -point phonons.

The assignment of the modes has recently re-entered a debate: Much evidence, such as site-selective isotope Raman data, speaks for the assignment of the mode at 600 cm^{-1} to the chain-oxygen vibration along the bond. In this case it is reasonable to assume that the modes are chain-related, become active because of broken symmetry in the chains, and represent a phonon density of states, which is anisotropic and sharp-featured due to the one-dimensional nature of the chains. However, recent *ab-initio* calculations find the phonon in question at much lower energies around 500 cm^{-1} , leaving only vibrations of oxygen atoms in the superconducting planes for a mode assignment at 600 cm^{-1} . [67] If this mode proves to be no chain-vibration, support for the assignment of the other defect-induced modes to the chains is reduced. The symmetry of the resonance then interferes with the determination of Raman tensor components. A Raman resonance profile of the UV excitation in the insulating parent compound can resolve this issue, since $\text{YBa}_2\text{Cu}_3\text{O}_6$ does not, by definition, contain Cu-O chain vibrations.

The persistent photo-induced change observed in Raman spectroscopy is in good agreement with the oxygen-vacancy reordering picture of the process. Again, it follows the electronic anisotropy in that the modes decrease ("bleach") in the visible, but grow under UV excitation. As explained in connection with the RAS results, this indicates less short chain fragments hosting the 2 eV resonance, but more single CuI atoms hosting the 4 eV transition. The bleaching quickens in compounds with larger unit cells in an experiment on a set of $R\text{Ba}_2\text{Cu}_3\text{O}_{7-\delta}$ -ceramic samples, indicating that the site change is easier in larger cells with smaller interaction energy.

The Raman-signal decay of resonant defect-induced modes in oxygen-deficient $\text{YBa}_2\text{Cu}_3\text{O}_{6.7}$ and $\text{PrBa}_2\text{Cu}_3\text{O}_{6.7}$ was investigated in the temperature range between 40 and 300 K. The temperature dependence of the bleaching shows a slow decay for low temperatures and an initially steep

and fast decay at high temperatures, which is well described by a stretched exponential function. In contrast to the more tetragonal $\text{PrBa}_2\text{Cu}_3\text{O}_{6.7}$, $\text{YBa}_2\text{Cu}_3\text{O}_{6.7}$ shows a pronounced change in curve shape between 160 and 190 K. We set up Monte Carlo simulations to follow the dynamics of chain-fragment development of oxygen superstructures in the chain plane of $(\text{Y,Pr})\text{Ba}_2\text{Cu}_3\text{O}_{6.7}$. There is good qualitative agreement between simulation and experimental dynamics at low temperatures. At room temperature, the description deviates from the Raman results, as ground-state annealing was not incorporated.

The time- and temperature-dependence under UV excitation is in some respects different from the visible case, which is mainly due to the nature of the UV resonance. At low temperatures, no growth under illumination is observed at excitation energy 4.1 eV, though changes occur at 2 eV and at 4.3 eV. The spectra also quickly lose intensity upon cooling. An interesting aspect is the fact that illumination changes the position of the modes.

In terms of the oxygen-vacancy reordering picture, there is generally good agreement with the aspects of persistent photo-induced change observed in Raman. The current understanding is that disordered patterns of oxygen are frozen in at low temperatures and illumination enables a limited relaxation towards the equilibrium state, which would be a more perfect superstructure pattern of full and empty chains with reduced fragment numbers. This assumption naturally yields an optimum temperature for efficient relaxation. However, room temperature bleaching is not contained in this description.

Electrical transport and Raman bleaching

Prior to the discovery of the impact of illumination on the optical properties, persistent photo-induced effects were found in the transport properties of $\text{YBa}_2\text{Cu}_3\text{O}_{7-\delta}$ as persistent photoconductivity or persistent superconductivity. [6, 7] As we have reviewed in Chap. 2 and confirmed in the optical studies in Chaps. 4 and 5, the optical and the transport effects share many common properties.

Both have been traced over time scales of minutes and hours of illumination, in case of transport even to many hours. Both are persistent at low temperatures (below 250 K), but relax back to equilibrium at room temperature. This among other arguments points to thermal relaxation analog to the oxygen reordering observed during room temperature annealing of quenched samples, and rules out a corrosive or destructive process. Persistent photo-conductivity occurs in all oxygen-deficient samples including the insulating specimens, but is absent or very weak in the fully oxygenated compound. [51] Likewise, visible Raman bleaching is restricted to underdoped samples. The choice of rare earth atom in the $\text{RBA}_2\text{Cu}_3\text{O}_{7-\delta}$ -family is not crucial to both effects. They also occur in the normal and superconducting state alike, as was verified by measuring the critical temperature before and after illumination at low temperatures. [123]

The illumination-induced decrease of resistivity is similar to the decrease during room-temperature annealing. For the latter, X-ray and neutron studies verified the superstructure-development in the Cu-O chain plane as origin of the change. [5, 17, 24] All three effects - thermal annealing, persistent optical change in Raman and RAS and persistent photoconductivity - share the typical stretched exponential type of dynamics in the onset as well as the relaxation, where they are accessible to observation. Thus, there is a wealth of information indicating that the phenomena base on the same microscopic origin.

Despite the evidence and the long standing assumption, the connection has not been explicitly studied up to now. Direct comparison of published data from different optical and electrical experiments is difficult because of the many parameters involved. The effects depend on sample details such as precise oxygen content and rare earth, as well as on experimental choices such as the light source, wavelength, power density on the surface and temperature. For this reason, we have performed a study where Raman spectra and transport data were acquired simultaneously in a combined setup from one sample, using the same illumination for optical analysis and persistent photoconductivity excitation. We find a difference of two orders of magnitude between the time constants of Raman bleaching and resistivity change. Within the oxygen reordering model, a Monte-Carlo model calculation of chain fragment evolution is used to discuss the relation between

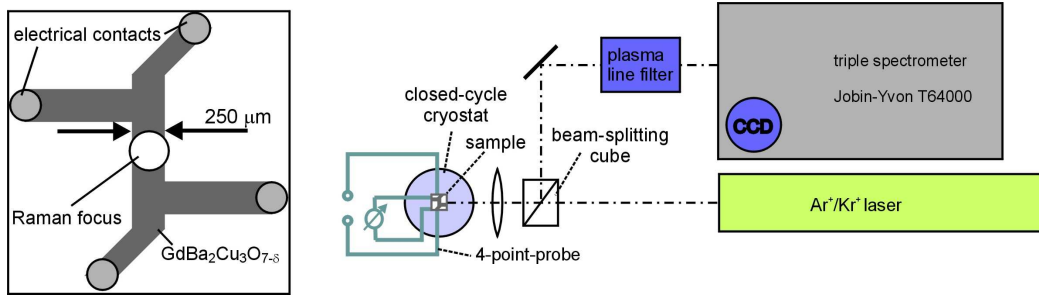


Figure 6.1: Schematic view of the sample geometry and the experimental setup for simultaneous acquisition of Raman and resistivity data.

different time constants and the development of Cu-O chains.

6.1 Combined Raman and electrical transport setup

In our collaboration, Prof. Dr. A. Fainstein and Prof. Dr. J. Guimpel at Centro Atómico Bariloche, Argentina, provided the combined setup for Raman and electrical measurements in their laboratories.

In order to confine the electrical current through the sample to a cross section penetrated by the light of the Raman focus, we used a thin film of $\text{GdBa}_2\text{Cu}_3\text{O}_{6.5}$ instead of a bulk sample. The film was approximately 1500 \AA thick. It was patterned lithographically to provide a narrow bridge of sample material ($250 \mu\text{m}$), which was covered by the Raman focus (diameter $250 \pm 10 \mu\text{m}$), as well as contacts for a four point probe (see left panel of Fig. 6.1). The sample was oxygen-reduced using the corresponding temperature and oxygen pressure values for bulk samples. From the curve of resistivity versus temperature in Fig. 6.2(a) can be seen that the film is superconducting with an onset temperature of 30 K. By comparison to the critical temperatures of a set of other $\text{GdBa}_2\text{Cu}_3\text{O}_{7-\delta}$ films we determine the oxygen concentration to be 6.5 ± 0.1 , close to the superconducting/insulating transition and in the ortho-II region of the phase diagram. [54]

A closed-cycle He-cryostat with an optical window provided the cooling. The Raman spectra were recorded using a triple Jobin-Yvon T64000 spectrometer equipped with a liquid- N_2 -cooled charge-coupled-device camera, as shown schematically in the right panel of Fig. 6.1. Spectra were collected in backscattering geometry, accumulating two times 15 s for each spectrum.

As a light source, both for illumination of the transport experiment as well as for excitation of the Raman spectra, we used the 568 nm line of an Ar-Kr-ion laser. The focus was placed on the conducting bridge of the sample with special care taken to cover the entire strip width (see Fig. 6.1). Due to this, there is some background signal from beyond the edges of the sample bridge in the spectra. The power applied in all series was 7.8 mW, leading to a power density of $(15.9 \pm 1.3) \text{ W/cm}^2$ on the sample surface.

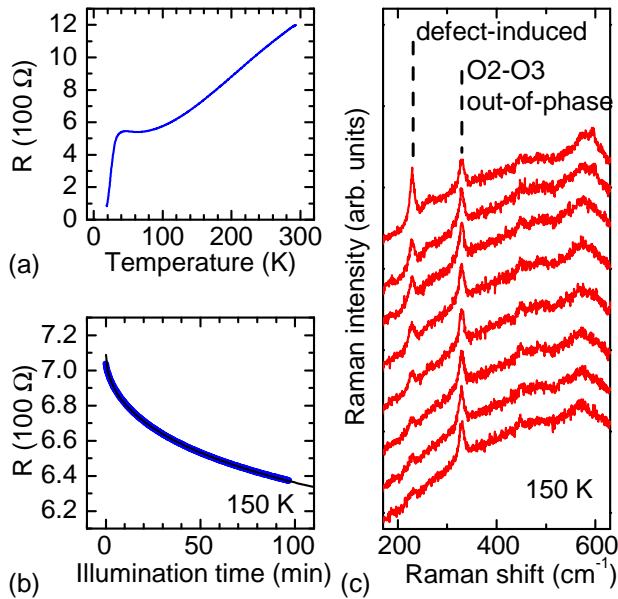


Figure 6.2: (a) Resistivity versus temperature in the non-illuminated film of $\text{GdBa}_2\text{Cu}_3\text{O}_{6.5}$ and (b) resistivity under illumination with laser light at 150 K (blue). The fit is a stretched exponential function (black). (c) Raman spectra taken sequentially with the same laser excitation, starting at the top (off-set). Each curve displayed represents an average over five spectra, with 150 s total accumulation time. While the Raman-allowed mode at 329 cm^{-1} is stable, the defect-induced mode at 229 cm^{-1} is quenched.

After each run, the sample was warmed to 300 K and kept there for at least one hour to ensure sufficient relaxation between different temperature measurements.

6.2 Results on simultaneous bleaching

Experimental data from the simultaneous Raman and transport setup is displayed in Fig. 6.2. Panel (a) shows the resistivity versus temperature curve of the unilluminated film. The curve indicates metallic behavior with a low T_c onset of 30 K, which is expected for an oxygen-reduced, superconducting sample near the transition to the insulating regime of the phase diagram. Estimates of the specific resistivity from the sample and contact geometry yield about $500 \mu\Omega\text{cm}$ at 150 K, which is a typical value for oxygen-reduced films with $\delta \approx 0.5$. [44, 46]

Figure 6.2(b) and (c) show an example of the effect of illumination on the sample at a temperature of 150 K. The resistivity curve (b) starts at the 150 K value of the unilluminated curve in (a) and decreases during the 90 min laser illumination period by 9%. In the same period of time, sequential Raman spectra were collected using the laser illumination for excitation. Figure 6.2(c) has the first spectra offset to the top of the picture, with illumination time increasing towards the bottom. As in the visible Raman bleaching experiments in Chap. 5, the Raman-allowed B_{1g} at 329 cm^{-1} does not change in intensity or position throughout the experiment. In contrast, the resonant oxygen-vacancy activated peak at 229 cm^{-1} loses intensity and almost vanishes in the background towards the end of the sequence. Several related peaks are seen around 260 cm^{-1} and just below 600 cm^{-1} . Like before, we follow the intensity decrease of the strongest peak at 229 cm^{-1} , fitting it with a Lorentzian line-shape and plotting the result in Fig. 6.3.

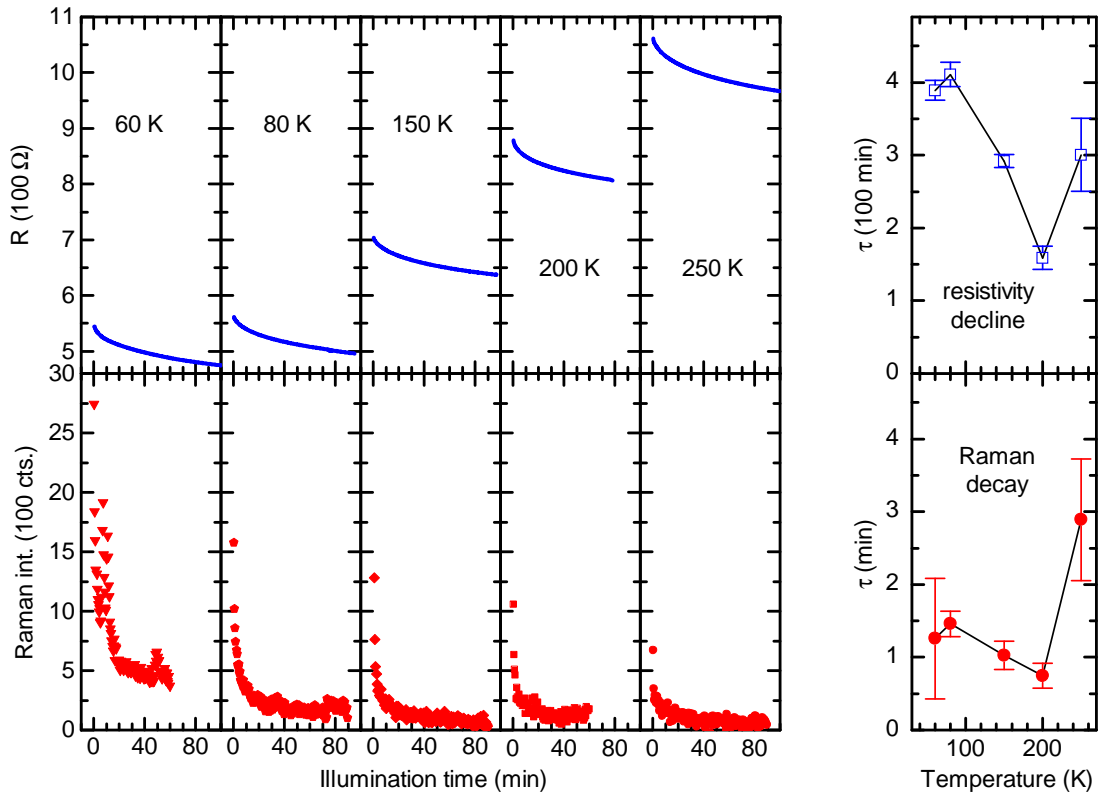


Figure 6.3: Simultaneous decrease of resistivity (upper panels, blue) and Raman intensity of the peak at 229 cm^{-1} (lower panels, red) at various temperatures in an illuminated thin film of $\text{GdBa}_2\text{Cu}_3\text{O}_{7-\delta}$. The rightmost panels show the corresponding time constants according to Eq. (5.14) with the exponent β fixed to 0.5.

The solid line in Fig. 6.2(b) represents a fit with a stretched exponential function also used in our previous Raman studies (see Eq. 5.14 in Chap. 5) and in persistent photoconductivity results in the literature. We here extract from it the time constants τ . For unambiguity and simplicity of comparison, we fixed β to 0.5 in all experimental curves, the value of β which gave us the best fit to Raman bleaching and transport curves with a single exponent.

The full set of time-dependent experimental data is shown in Fig. 6.3, with the resistivity decrease in the upper panels and the Raman intensity loss in the lower panels for illumination series at different temperatures. Time constants τ from stretched-exponential fits to the curves are plotted versus temperature in the rightmost panels.

The resistivity decrease starts at higher values for higher temperatures, as expected from the resistivity of the unilluminated curve [Fig. 6.2(a)]. In accordance with previous findings, the photo-induced change becomes faster with increasing temperature. [123] At 250 K, the highest temperature investigated, τ increases somewhat. This can be due to relaxation effects known to set in in this temperature range. [10, 49] The Raman intensity decrease shows a similar behavior

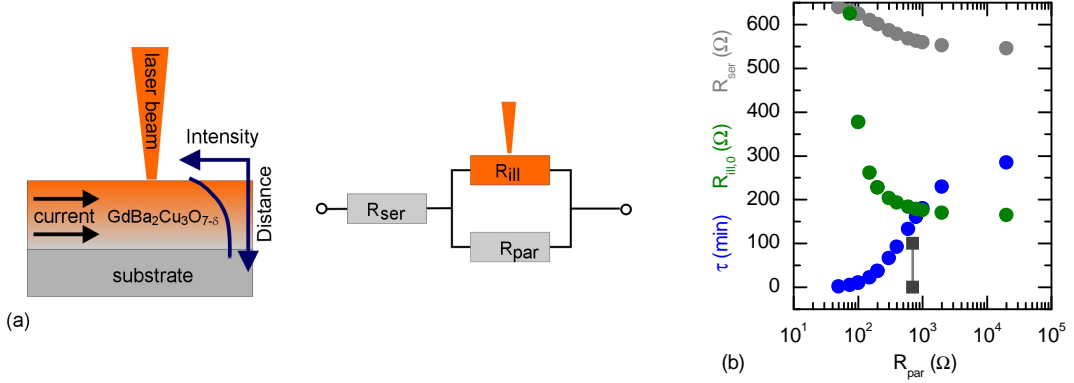


Figure 6.4: (a) Sketch of the cross section of the superconducting film on the substrate. The incident intensity decreases beneath the surface. The simplest assumption modelling the situation is a light-affected resistor in parallel with a constant one. (b) Parameters of a fit of the combined resistivity curve (Eq. 6.2) to the resistivity data taken at 150 K. $R_{ill,0}$ initial illumination-dependent resistivity, R_{ser} and R_{par} the unaltered resistivity in series and in parallel with the sampling volume, τ time constant of the decrease.

for τ versus T , with a minimum at 200 K and subsequently a pronounced increase. This is in agreement with previous studies on temperature-dependent Raman bleaching, where the most efficient decrease occurred around 190 K. [59, 124] However, the error of the fit at 250 K is large because of the limited time resolution of the spectra. At 60 K, we observed fluctuations in the Raman intensity caused by very small shifts of the Raman-focus position, resulting in another large error for this fit. Except at 60 K, Raman intensity decreases to background levels within the duration of the experiment.

The most striking result of our experiment is the large difference in absolute time constants in Raman and transport: The Raman-intensity decrease is faster than the reduction of the resistivity by roughly two orders of magnitude. This raises the question whether the assumption of a common microscopic origin based on the previous evidence is actually justified.

We discuss first a technical aspect of the two measurements and its influence on the time constants. There is a technical difference between Raman spectroscopy, which probes the illuminated volume, and electrical current, which can also access unilluminated areas of the sample. The width of $250 \mu\text{m}$ of the conducting bridge was covered by the Raman focus on the surface sample (see Fig. 6.1). However, the film was 150 nm thick and though it was still transparent to the eye, the power density decreases exponentially between the surface and the lower layers due to absorption. This situation is illustrated in the left panel of Fig. 6.4. Thus, while lower lying layers receive lower power density and contribute less to the Raman signal, all layers contribute to the resistivity regardless of illumination and the according time-dependent change. If the resistivity decreases according to a stretched exponential function in the illuminated volume, but has also constant, parallel contributions, the time constant extracted from a fit to the overall resistivity will be perturbed. We model the influence of any unperturbed contribution by a constant resistor in parallel

with the time dependent one as shown in the middle panel of Fig. 6.4. The latter is described with a stretched exponential (Eq. 5.14, $\beta=0.5$), and the combined resistivity function is thus:

$$R_{ill}(t) = R_{ill,0} \exp \left[- \left(\frac{t}{\tau} \right)^\beta \right] \quad (6.1)$$

$$R(t) = R_{ser} + \frac{R_{par} \cdot R_{ill}(t)}{R_{par} + R_{ill}(t)}, \quad (6.2)$$

where t is illumination time, $R(t)$ the observed resistivity, R_{ser} and R_{par} the unaltered resistivity in series and in parallel with the sampling volume, $R_{ill,0}$ and $R_{ill}(t)$ the initial and illumination-dependent resistivity in the sampling volume, and τ and β the time constant and exponent from the stretched exponential decay. Figure 6.4 shows the $R_{ill,0}$, R_{ser} and τ obtained from fits to the data from an illumination experiment at 150 K for different values of R_{par} . As expected, the time constants remain unaltered when the parallel resistivity is high and start to deviate when the values approach the same order of magnitude as $R_{ill,0} + R_{ser}$. For an estimate of the upper bound of this effect we simply take the film to be half-illuminated. This assumption is based on a penetration depth of 85 nm at $\lambda=568$ nm derived from an ellipsometric study on YBCO with $T_c=66$ K in Ref. [77]. A fit of $R(t)$ to the resistivity data taken under illumination at 150 K then yields a reduction in τ by a factor of four. From the best fit to the data with the parallel resistor, we obtain a slightly constant resistivity with τ diminished by a factor of eight. Thus, part of the difference in the time constants may be due to the reduced illumination closer to the sample-substrate interface. However, even the upper estimate of this technical aspect cannot account for the observed two orders of magnitude difference alone.

6.3 Discussion within oxygen reordering picture

We will now discuss the remaining difference of over one order of magnitude in terms of the microscopic origin of photoinduced effects in underdoped $R\text{Ba}_2\text{Cu}_3\text{O}_{7-\delta}$. We model the oxygen vacancy reordering by a Monte Carlo simulation of oxygen rearrangement in a layer of Cu-O chains that was set up in Chap. 3. This ‘‘Asymmetric next nearest neighbor model’’, describing the oxygen ordering phase diagram, was combined with next-nearest neighbor hopping rules (Kawasaki dynamics) for oxygen atoms in the plane. The interaction parameters V_1 to V_4 are as defined in Chaps. 3 and 5 and in Ref. [24]. Likewise, we define temperature throughout this work by the relation of $100 \cdot 10^{-3} V_1 / k_B = 543$ K. In the two simulation runs presented, we equilibrated a 1200 by 1200 site matrix at 1000 K, well into the tetragonal region of the structural phase diagram, with oxygen filling factors of 0.50 and 0.66, respectively. Then we quenched the matrix to 350 K, where we monitored the development of chain fragments of different length. At lower temperatures, a more ordered chain pattern with longer fragments is expected. In the case of low oxygen filling (0.5), which corresponds to our sample, a superstructure cell emerges with a pattern of alternating full and empty chains perpendicular to the chain direction (ortho-II), while the higher oxygen

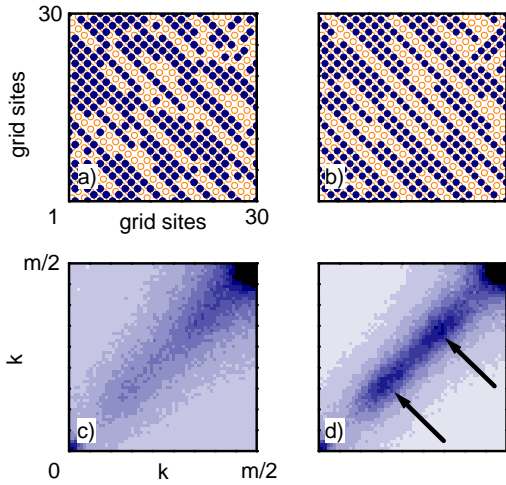


Figure 6.5: (a,b) Monte Carlo simulation of oxygen diffusion in a chain plane with concentration 0.66 in real space, with the crystallographic axes running along the diagonals (open symbols represent Cu atoms, full symbols O), (c,d) and after two dimensional discrete Fast Fourier Transform ($m=1200$) (a) and (c) correspond to the state after annealing at 1000 K, (b) and (d) after subsequent quenching and annealing at 350 K. Note the appearance of the two superstructure peaks corresponding to the ortho-III phase (arrows).

filling (0.66) develops a more complicated pattern with two full and one empty chain (ortho-III).

Figure 6.5 illustrates a part of the matrix with 0.66 before and after chain fragment development at 350 K. The a and b axes of the unit cell run at 45° to the picture boundaries. During annealing at 350 K, the disorder with a high number of short chain fragments in (a) vanishes in favor of longer fragments (b). A pattern has developed in which two oxygen-filled chains alternate with one empty chain. In Fig. 6.5(c) and (d) the Fourier transform is displayed, illustrating the corresponding increase of ortho-III signal at one third and two thirds of the diagonal (arrows).

The reordering of chains into longer fragments and regular patterns is known experimentally from thermal annealing of oxygen-deficient $\text{YBa}_2\text{Cu}_3\text{O}_{7-\delta}$. [5] Its effect on conductivity comes from the ability of the chain-Cu atoms to dope the superconducting planes depending on their oxygen coordination number. [40] In this picture, an average of two-fold (no chain) and four-fold (within chain) coordinated Cu atoms provides higher hole doping to the planes than the same ensemble of three-fold (chain-end) coordinated Cu atoms, though the total number of oxygen atoms in the plane remains unaltered. Resistivity is thus sensitive to a change of the average Cu coordination number, or average fragment length, correspondingly. The forbidden Raman scattering signal, on the other hand, from the results of a cluster calculation is attributed to a resonant electronic excitation at a short chain fragment (see Chap. 4). [83] The Raman intensity should therefore be high for a large number of short fragments and decrease as annealing into longer chains occurs. It is assumed to be proportional to the density of resonance excitation centers in the chain plane, as nonlinear effects can be excluded from previous results.

Microscopically, the observed annealing of shorter fragments into longer Cu-O chains has different effects on the Raman scattering signal and on the transport measurements: Raman is more sensitive to the quickly vanishing shorter fragments, while the increase in carrier concentration is driven by the slower change of average Cu coordination. Figure 6.6 illustrates the idea. The left panel shows the number of fragments in an oxygen matrix versus simulation time with the

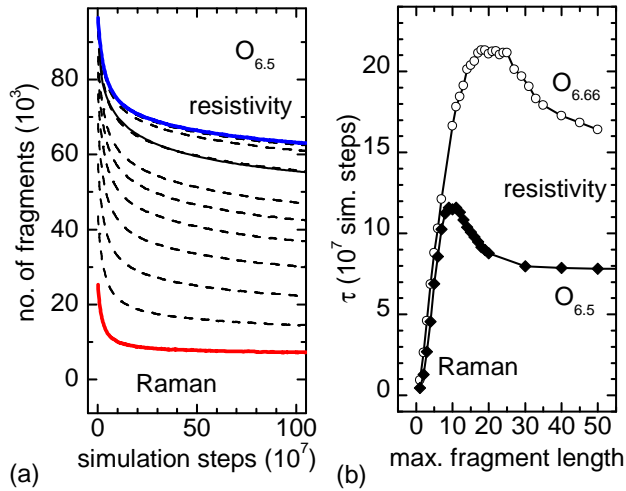


Figure 6.6: (a) Number of chain fragments versus simulation steps by length, taken from the matrix with oxygen content 0.5. The lowest curve represents single oxygen atoms and corresponds closest to the Raman signal (red), the uppermost line represents all fragments regardless of length and is related to the resistivity in our model (blue). In between are length 1+2, 1 to 3, 1 to 4 etc. A fit example to the fourth curve from the top is also shown. (b) Extracted time constants, full symbols correspond to oxygen content 0.5, open symbols to 0.66.

fragment length as a parameter. The lowest curve represents single oxygens only, the highest the total fragment number of any length. Intermediate curves are also shown (dashed lines). Time constants extracted from both matrices using a stretched exponential fit are displayed in the right panel of Fig. 6.6. The best fit to all curves with the same β was obtained with $\beta=0.28$. The parameter depends on the temperature difference of the simulated quench and in this case is slightly different from the experimental result, however, no quantitative comparison between experimental and model time constants is intended. Generally, the time constants are shorter for the matrix with lower oxygen content. Comparison within the time constants for each matrix shows that the short chain fragments responsible for the Raman signal decrease about 15 to 20 times faster than the total number of chain fragments related to the decrease in resistivity for both oxygen contents tested. We can thus ascribe the two seemingly different experimental time constants to two aspects of the same microscopic chain ordering process. We note that this difference is not critically dependent on the oxygen content between 6.5 and 6.66, or on the type of superstructure pattern.

Remarkably, the slowest decrease occurs for intermediate chain length. This is related to the fact that short fragments simply disappear and long fragments continuously grow. Intermediate curves, however, result from a balance between creation and destruction, which gives them longer life time.

Another similarity we note is that of fast Raman bleaching and the fast response of the carrier mobility under illumination. Hall measurements in Ref. [44] have shown that both carrier concentration and mobility increase under illumination. We estimate from the data that mobility reacts faster than carrier concentration by about two orders of magnitude, putting it into the same range of time constants as Raman bleaching. It is plausible that short chain fragments act as scattering centers for the carriers, so that a rapid decrease of their number under illumination could explain the mobility increase observed. Systematic Hall measurements during thermal annealing, under illumination and during relaxation after illumination have shown that photoexcitation

has a stronger effect on carrier mobility than annealing, and also that its relaxation is thermally driven. [54] The latter finding supports the idea that oxygens have been displaced by illumination. The fast response of mobility to light indicates that the situation is more complex than in thermal annealing only. Illumination is not only pushing the system towards a new equilibrium point, it is also altering its character. As was already discussed in the context of temperature-dependent visible Raman bleaching in Chap. 5, it would therefore be interesting to extend model calculations to a form where the final state is not identical to a different state of thermal equilibrium, but instead a state in which the number of very short chain fragments should be even more reduced. Raman bleaching and Hall measurements are the corresponding tools for observing these fast and slow elements of the structural change in experiment.

6.4 Summary

Summarizing the results from the simultaneous study of persistent photo-induced effects in underdoped $\text{GdBa}_2\text{Cu}_3\text{O}_{7-\delta}$, we found that the characteristic time constant of Raman bleaching is two orders of magnitude faster than the response in electrical resistivity, in spite of the similar properties and temperature dependences they show. Similar time-scale differences between carrier concentration and mobility provide evidence that Raman response is connected more closely to the mobility than to the overall electrical conductivity.

Within the model of oxygen-vacancy reordering, using a Monte-Carlo simulation of chain-fragment development after a temperature quench, this apparent contradiction can be reconciled. In this picture, Raman response is connected to the number of short fragments, which react quickly to the new equilibrium conditions. Electrical conductivity, on the other hand, senses the slower change of average Cu coordination numbers. We are thus able to show that Raman bleaching and persistent photoconductivity are connected to the same microscopical origin of oxygen reordering and yet display different characteristic time constants.

The results presented here show that the observed properties are consistently explained within an oxygen reordering model. A single parameter charge transfer process, on the other hand, cannot account for the large difference in time constants observed, though we do not exclude an additional contribution to the effect by trapped carriers. The long-standing assumption that Raman bleaching and persistent photoconductivity are two sides of the same light-induced change in the underdoped $\text{RBa}_2\text{Cu}_3\text{O}_{7-\delta}$ material family must be altered: The optical and electrical response are connected, but not identical. Their comparison can yield distinct information on the microscopic properties governing the Raman response, the conductivity, and the carrier mobility.

X-ray data on oxygen superstructures under laser illumination

The oxygen content as well as the superstructure ordering affect the axes length of the unit cell of $\text{YBa}_2\text{Cu}_3\text{O}_{7-\delta}$. Samples with higher, or more ordered oxygen content in the chain plane are more orthorhombic with a longer b axis and a shorter a axis, and they have a shorter c axis compared to the tetragonal structure. [5, 33, 45, 125, 126] A direct observation of diffraction peaks from the superstructure periodicity is a challenging experimental task, because oxygen atoms are weak X-ray scatterers and their diffuse scattering peaks are several orders of magnitude smaller than the Bragg peaks of the ideal structure. After early evidence from other methods like electron diffraction, neutron diffraction and NMR, this was achieved in the X-ray diffraction on bulk samples in synchrotron radiation experiments, and a number of studies have appeared since (see for example Refs. [17, 24–26, 31, 32]). Schleger *et al.* [32], in particular, monitored the change of the ortho-II superstructure peak during thermal annealing, showing that the pattern development advances in the process.

Illumination with visible light was also shown to alter the c axis length, providing some direct evidence of the structural side of persistent photoinduced effect. [52, 53] Within the oxygen-vacancy reordering model under investigation here, we considered it a logical consequence to search for the oxygen superstructure diffraction peaks and their change. Considering the short penetration depth of visible light of between 30 and 140 nm (see Fig. 4.2 in Chap. 4), we confined the volume detected by the X-rays to the same scale by a grazing-incidence scattering geometry. We successfully detect with X-rays diffuse oxygen superstructure in our samples. However, we could not establish a change of the superstructure under illumination and conclude that the induced change is either too weak, or of too short a range to show up in X-ray diffraction.

7.1 Surface sensitive X-ray diffraction on beam line ID32

The X-ray diffraction experiments were performed in collaboration with Dr. I. Joumard, Dr. T. L. Lin and Dr. J. Zegenhagen from the beam-line ID32 for surface and interface studies at the European Synchrotron Radiation Facility ESRF, Grenoble. Four samples of single crystalline, untwinned oxygen-deficient $\text{YBa}_2\text{Cu}_3\text{O}_{7-\delta}$ were investigated, two of which were supplied by G. Nieva ($\text{YBa}_2\text{Cu}_3\text{O}_{6.7}$, referred to as YBCO2, $\text{YBa}_2\text{Cu}_3\text{O}_{6.65}$, referred to as YBCO2b), while the other two were supplied by V. Hinkov (YBCO3 and YBCO4), see the appendix for details.

The diffraction chamber of the beam-line has a six-circle HUBER diffractometer with a “Cyberstar” NaI(Tl) detector, configured with a HUBER tower as a mount for the cryostat and sample.

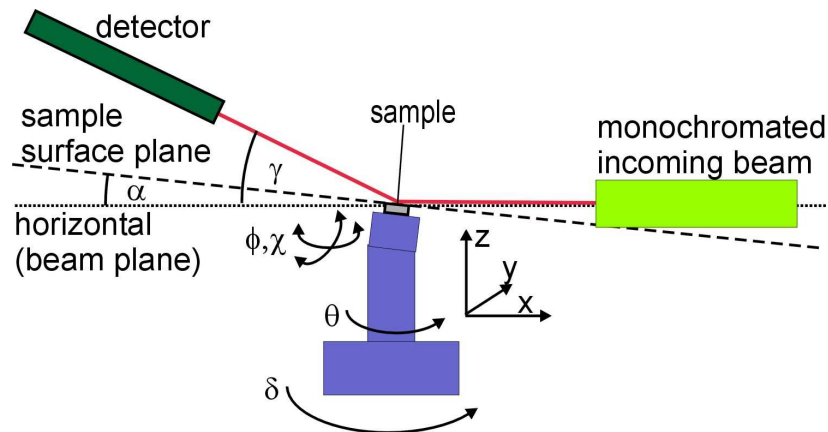


Figure 7.1: Schematic picture of the grazing incidence ($\alpha < 0.4^\circ$) X-ray scattering set-up with the sample mounted on the tower of a Huber diffractometer. The sample can be displaced in x , y and z direction, tilted by ϕ and χ and turned by θ . The detector can be moved by the angles γ and δ . The cryostat encasing the sample and the additional laser illumination are not shown (see picture in Fig. 7.2).

A scheme and a picture of the experiment are shown in Figs. 7.1 and 7.2. The cryostat has a kapton foil window and was cooled to about 100 K with LN_2 . A monochromator in an up-beam chamber selected 17 keV for the incoming beam in the experiment. The angle of incidence used was between 0.5 and 0.2° to the surface.

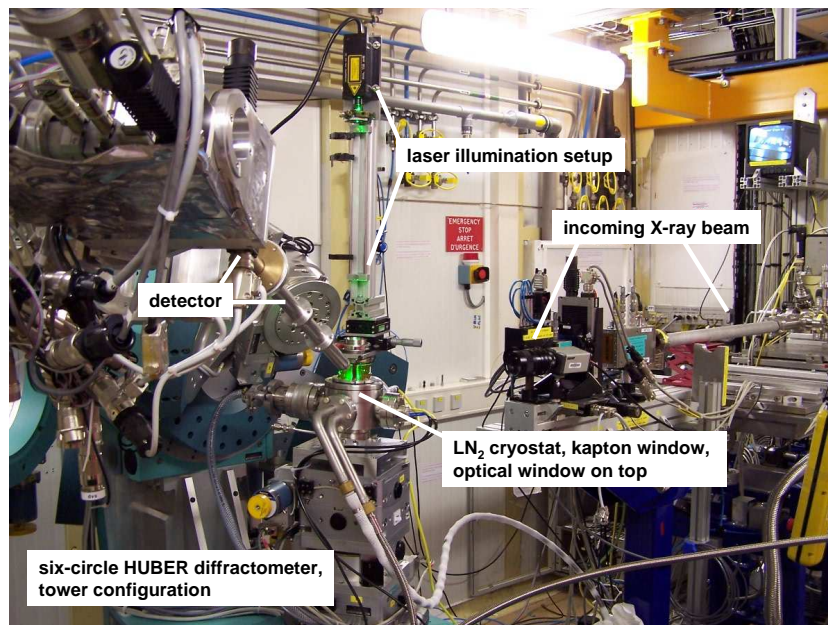


Figure 7.2: Picture of the experimental diffractometer setup at the beam-line ID32, ESRF, Grenoble.

In addition to the X-ray equipment, a compact frequency-doubled Nd-YAG laser giving 120 mW of 532 nm light was mounted on top of the cryostat, which had an additional optical window for this purpose. The polarization and focus size were manipulated with a half-wave plate and an adjustable lens, respectively.

7.2 X-ray scattering from oxygen vacancy superstructures in $\text{YBa}_2\text{Cu}_3\text{O}_{7-\delta}$

X-ray scans on the four samples are shown in Fig. 7.3. The Miller index h corresponds to a scan in real space in a direction, which is the direction perpendicular to the Cu-O chains. In the scans along h we indeed find reflections from the oxygen superstructures with a periodicity larger than that of the underlying cell in all samples as expected. The Bragg peaks situated at integer values of h are two to three orders of magnitude stronger than the superstructure peaks. Although the oxygen content and treatment is similar, all samples display different periodicity, reflecting the rich oxygen phase diagram in the range of the 60 K plateau. YBCO2 in (a) has $\delta=0.3$, and peak positions at broken h -values $\text{int}(h).36$ and $\text{int}(h).64$ ($\text{int}(h)= \dots-1, 0, 1, 2\dots$ denotes the integer part of h), consistent with ortho-III ordering (full-full-empty chain), or possibly with a more complex ortho-VIII pattern as suggested in Ref. [17]. YBCO2b in (b) has a strong peak at $\text{int}(h).50$ corresponding to the ortho-II phase (full-empty chain), which would be expected at slightly higher δ than its $\delta=0.35$ nominal oxygen content. YBCO3 with $T_c \approx 60$ K in (e) shows a mixed phase, with a contribution from ortho-II ($\text{int}(h).50$) and peaks at $\text{int}(h).43$ and $\text{int}(h).59$, which are consistent with an ortho-V phase. YBCO4 with $T_c \approx 60$ K in (f) with peak positions $\text{int}(h).39$ and $\text{int}(h).61$ is consistent with a pure ortho-V. The positions were obtained from fits with a Voigt line shape, with an error of the order of ± 0.01 . Among the superstructures, ortho-II is stronger than the others by an order of magnitude, confirming earlier reports. [17] We note that the diffraction signal from oxygen superstructures in the near-surface volume probed here are generally in good agreement with studies on the bulk material. [17]

Figure 7.3(c),(d),(g) also shows scans in k -direction, which were only recorded for three out of four samples. In the scanning direction along the chains, superstructure peaks are absent, except

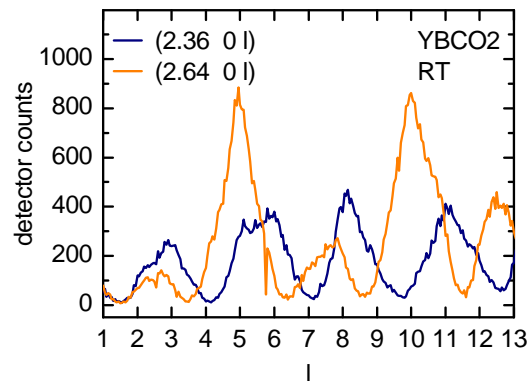


Figure 7.4: Modulation of the superstructure signal in scans along l in sample YBCO2 (see Fig. 7.3(a) for scan along h, k).

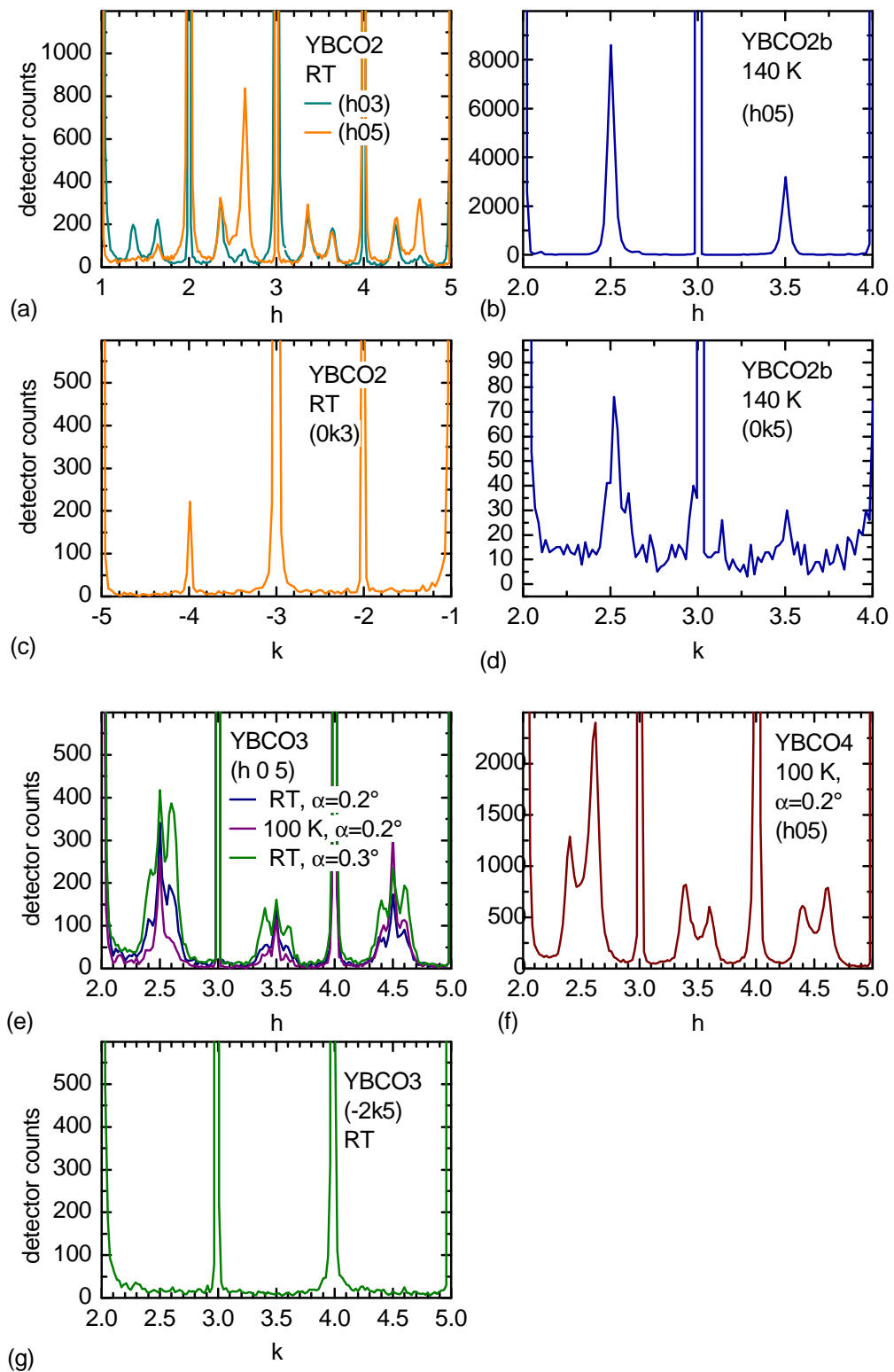


Figure 7.3: X-ray scattering peaks showing Cu-O chain superstructure ordering in four different samples of $\text{YBa}_2\text{Cu}_3\text{O}_{7-\delta}$. The peaks are visible in scans perpendicular to the chain direction (along h), but are absent along k in (a), (b) and (c) ((d) was not checked), which is evidence of the excellent detwinning of the samples. Though all samples have T_c around 60 K and consequently similar oxygen content around 6.6 or 6.7, they display different superstructures.

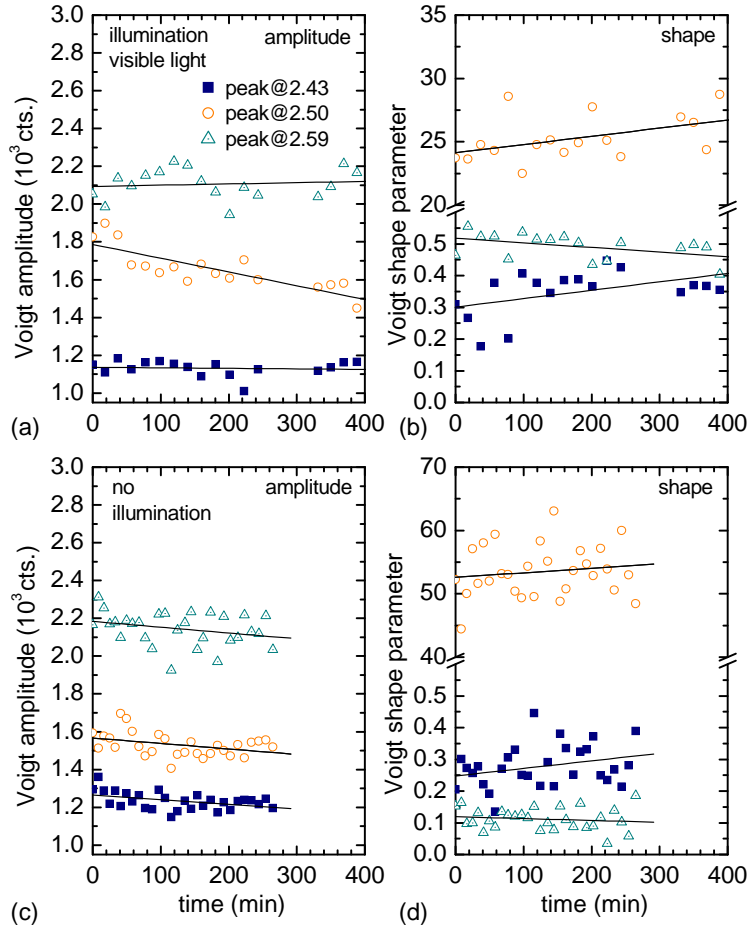


Figure 7.5: Amplitude and shape from fits to the three superstructure peaks in sample YBCO3 (see Fig. 7.3(c)) in sequential X-ray scans at 150 K using a Voigt line-shape. The upper panels shows a sequence in which the sample was illuminated with 120 mW, 532 nm. The lower panels show a sequence without additional illumination. The change under illumination is small, and cannot be reliably distinguished from the very small drift of the experiment on a time scale of hours.

for some traces of the ortho-II peak, which are two orders of magnitude weaker than in the h -scan. The spectra thus show excellently detwinned samples.

The two scans in Fig. 7.3(a) show that the superstructure peak intensity depends on the l index of the scan. This effect is further explored in Fig. 7.4, where l was varied. The scans cross the maximum of the superstructure peaks in Fig. 7.3(a) and keep their center h -values constant, but show an intensity modulation along l . This effect was studied by Plakhty *et al.* [26], who applied it to a refinement procedure of the unit cell, showing that the oxygen superstructures displace other atoms in the unit cell to some extent. [17, 25, 26]

7.3 Superstructure peaks under additional illumination in the visible

Figure 7.5 shows parameters extracted from sequential h -scans on the YBCO3 sample using Voigt linehapes. Three peaks were used to fit the scans of the type shown in Fig. 7.3(c). The change of background is negligible compared to the amplitudes, and the width of the peaks was kept constant to prevent interference with the additional parameter steering the Gauß/Lorentz ratio in

a Voigt lineshape. The amplitudes and the shapes are plotted versus time in the figure. The sample was cooled to 150 K to exclude any thermally activated reordering. In the sequence in the upper panels, the sample was irradiated with additional visible light. In the lower panels we show a sequence taken in the dark for comparison. Although the amplitude and shape parameters change somewhat under illumination, their magnitude is so small that a reliable distinction from the very small amount of drift in the system over the long period of measuring time is difficult. So unfortunately, we are unable to show the direct link of persistent photo-induced effects to the structural change of vacancy reordering this way.

Although this result certainly puts some constraints on the oxygen reordering model under illumination in terms of amplitude and range, it is not completely at odds with the experiences in thermal reordering. Our results confirmed that the diffuse peak intensity of ortho-II is an order of magnitude stronger than the ortho-II/orthoV mixture presented in Fig. 7.5. We mentioned the study by Schleger *et al.* [32] on the ortho-II peak, which is the candidate with the longest range ordering capabilities among the superstructure phases. In their thermal reordering study, the sample was quenched from a temperature of 200°C by 50° or more. Such treatment can account for ΔT_c as high as 20 K according to the results by Jorgensen *et al.* [5]. By comparison, the maximum change in T_c observed at low oxygen content around the phase transition (see Chap. 2) was only about 10 K, so it is reasonable to assume that the magnitude of the change in superstructure in our experiment is much smaller than Schleger *et al.*'s. There is also some uncertainty concerning the overlap of the sampled and illuminated area, which could differ by a factor of two to three, while in thermal reordering the entire bulk change contributes to the peak.

The absence of a change in the superstructure peaks can thus be due to a sensitivity problem. While Raman scattering is defect-activated, sensing directly the disordered character of the system, X-ray diffraction is probing the degree of regularity. A small change in short fragment numbers may thus mean a relatively large change in disorder, but a small change in overall periodicity. From this point of view, our result supports the picture of photoexcitation promoting the reduction of short fragments compared to their number in thermal equilibrium or frozen disorder. It remains an open task, however, to estimate the upper limit of structural change within the sensitivity of the X-ray experiment. This would put a constraint on the structural effect of photoexcitation. As an alternative to the direct detection of change in the superstructure reflections, one could do a study of the easier accessible change of axes-length under illumination, which was reported earlier. [52,53]

Summary and outlook

In this work we have studied the persistent photo-induced effects in oxygen-deficient $RBa_2Cu_3O_{7-\delta}$, applying Raman scattering under visible and ultraviolet excitation, reflectance anisotropy spectroscopy, electrical transport measurements, and diffuse X-ray diffraction. We discuss our data within an oxygen-vacancy reordering model with the help of a numerical simulation. Our results show that structural reordering consistently explains the observed effects, developing further our understanding of the process. Although some of the evidence is at odds with a purely electronic explanation of photo-induced effects, an additional contribution cannot be excluded.

Irradiation with visible and UV light is known to enhance the conductivity and the critical temperature in oxygen-deficient $RBa_2Cu_3O_{7-\delta}$ persistently, if only to a limited extent. In the current understanding of the electronic phase diagram of the cuprates this is due to a change of the hole doping level in the superconducting planes. Illumination thus opens a way to continuous and reversible tuning of doping, without the need to resort to a set of different samples, or to permanent altering of one sample. All persistent photo-induced effects share a number of characteristic properties. Photo-sensitive features have a time dependence on the scale of minutes to hours, which can be described by a stretched exponential function. The change can be invoked at room temperature as well as below room temperature, with a distinctive temperature dependence of the dynamics upon cooling. After illumination, it is stable at temperatures below approximately 250 K, but relaxes at room temperature and above. The effect exclusively occurs in oxygen-deficient compounds of the $RBa_2Cu_3O_{7-\delta}$ -family, so that a connection to its specific structural feature of fragmented Cu-O chains must be presumed.

Detailed information on the persistent photoconductivity is available in the literature, and a smaller number of studies concerning visible resonant Raman bleaching were also reported. We extract from this work two possibilities for the interpretation as our starting point: Either the change is explained in terms of an electronic mechanism of photoexcited carrier pairs, where the electron is trapped in an oxygen vacancy site, or photo-assisted structural reordering of oxygen vacancies is the underlying process. The fact that the carrier mobility versus critical temperature shows a hysteretic behavior in an illumination-relaxation cycle is a strong argument against a purely electronic explanation. This among other issues, like the direct connection between illumination and c -axis length, prompted us to choose the oxygen vacancy reordering model as a framework for an in-depth discussion of our experimental results.

Within the vacancy reordering picture, the doping mechanism of persistent photo-induced effects is identical to that identified in thermal annealing of underdoped $RBa_2Cu_3O_{7-\delta}$. The com-

pounds show a rich structural phase diagram with superstructure patterns in the Cu-O chain plane constituted by vacancy sites. They are a doping reservoir for the CuO₂ superconducting planes. An ordered superstructure has long Cu-O chains opposed to empty Cu chains, and transfers carriers more efficiently than a disordered distribution of chain fragments with a large number of chain-end Cu atoms. The thermally activated reordering into these superstructure patterns are slow at room temperature, leading to an ageing effect evident in the axes length and T_c , and freeze out soon below. Since the phases are crucial to a reproducible sample preparation, they were extensively studied experimentally, for example by diffraction techniques, and theoretically, by LDA calculations or parameter-based models like the Monte-Carlo based ASYNNNI approach.

We adapted such an ASYNNNI model taken from the phase diagram description, regarding the development of chain fragments analogous to the case of thermal reordering in a first approximation. Having reproduced the basic phase diagram for validation of our simulation, we monitor the number of chain fragments in a simulation matrix. With the dynamics of Kawasaki-type chosen for the in-plane diffusion, their dynamics satisfactorily describes the non-exponential decrease observed: While at first the short fragments quickly merge, the ordering process slows down once longer chains are built. Due to their stability, they are a barrier against further oxygen movement, restricting further ordering to some sort of domain growth, where whole chains are displaced or compete at boundaries of similar pattern.

In Raman spectroscopy under visible excitation, we confirmed that the bleaching effect is specific to defect-induced modes in oxygen-reduced samples, though not to the concentration range of superconducting compounds, as reported by other groups. It was found for all R tested in a systematic study, where in accordance with expectations from the reordering model, the bleaching is faster in compounds with a larger, more tetragonal unit cell. The time constants of visible Raman bleaching also shorten with increasing temperature. The process displays a distinct change in dynamics around 190 K where it is most efficient. Under the assumption that photoexcitation re-enables local oxygen site changes below the thermal freeze out, the temperature-dependent simulations are in good qualitative agreement. They reproduce the non-exponential decay observed in all Raman experiments, as well as the maximum efficiency at intermediately low temperatures. However, they do not account for the observed room-temperature bleaching, since no deviation from thermal equilibrium at room temperature is incorporated in the model. Room temperature bleaching indicates a clear difference between the equilibrium order under thermal and under illumination conditions.

Further insight on the nature of this difference is gained from a simultaneous Raman and transport experiment. As mentioned above, the photo-induced effects in the two methods share characteristic properties, and were assumed to have identical microscopical origin as consequence. The simultaneous experiment, however, revealed that their time constants differ by two orders of magnitude. An analysis of the setup estimating the error due to inhomogeneous illumination concluded that the observed difference clearly exceeds the maximum possible deviation. This

observation is difficult to reconcile with a single parameter model like trapped photo-carriers. If electronic defects states filling up with trapped carriers are the only process, the consequences for different physical properties need not have the same amplitude, but they must have identical time dependence. In oxygen reordering, on the other hand, extremely different time constants easily occur when the dynamics of the fragments are regarded with respect to their length. Short fragments are quickly appended to another chain, but the average chain length grows much slower. Thus, we interpret the result as an indication that Raman defect-induced modes sense the short-fragmented disorder, while the conductivity is controlled by the overall change in doping due to the growing chain length. Support comes also from Hall measurements, which distinguish mobility and carrier concentration. Under illumination, the mobility also rises two orders of magnitude faster than the conductivity, and it reacts much stronger to photoexcitation than to thermal reordering. This can be understood if the mobility is subdued by scattering on defects like short chain fragments, the number of which is over-proportionally reduced by illumination.

Another result in favor of local short fragment reduction are the X-ray spectra. While superstructure periodicity was successfully detected in the surface of $\text{YBa}_2\text{Cu}_3\text{O}_{7-\delta}$ by X-ray diffraction in grazing incidence, we could not establish a change under illumination. The change generally might have been too small for a detection with this method, or the locally appended short fragments make little difference to the long range periodicity.

A promising new approach to persistent photo-induced effects in $\text{RBa}_2\text{Cu}_3\text{O}_{7-\delta}$ is the application of reflectance anisotropy spectroscopy to the ab plane in the energy range of the visible to the UV. We find a rich anisotropy spectrum that displays characteristic persistent photo-induced effects in three resonances, b -polarized at 2.2 eV and 4.15 eV, and a -polarized at 4.4 eV. Evidently, there is a direct link between illumination and the electronic anisotropy. From a comparison with the dielectric function we show that they correspond to a peak existing exclusively in one crystal direction, and that they are particular to the oxygen-deficient compounds. We ascribe the UV peaks intra-ionic transitions in the two-fold coordinated Cu atoms. With the help of a cluster calculation, the 2.2 eV resonance is assigned to a b -polarized excitation in a short fragment. The fact that the 2.2 eV resonance decreases under illumination, while the 4 eV peaks increase, matches excellently the prediction from oxygen reordering. Short fragments hosting the former vanish, while two-fold coordinated Cu atoms hosting the latter increase along with their – non-resonant – four-fold coordinated counterparts. We confirmed the typical properties for the photo-induced change in RAS. The change is slow, on the order of hours, it is stable at 200 K, but relaxes at room temperature. It is also clearly polarization-dependent, triggered only for polarization along the chains in the visible. RAS is an interesting tool for further studies, for example to gain more overview about the temperature dependence or the spectral efficiency of the effect.

We have shown that the Raman response matches the in-plane anisotropic resonances excellently. It is known that the defect-induced modes resonant around 2.18 eV have sharply anisotropic in-plane selection rules. The resonance profile matches the 2.2 eV RAS-peak in position, polar-

ization orientation and in the decrease in strength under illumination. In fact, we find another, exceptionally strong resonance matching the 4 eV RAS-peaks, and again the Raman response follows the electronic peak in polarization and amplitude under illumination - it grows. Interestingly, photoexcitation affects the Raman peak positions at this resonant excitation, a hint towards renormalization or double resonant effects, which encourages further investigation.

Raman modes are found above 230 cm^{-1} and around 600 cm^{-1} under visible excitation. In the UV the mode at 600 cm^{-1} is very prominent, among many features covering the range from 100 to 1300 cm^{-1} on top of a broad background. The discussion on the activation mechanism and assignment has been reopened recently. Since the modes are related to defects in the chains, it is reasonable to ascribe them to chain-related modes activated by broken symmetry. Site-selective isotope experiments and early shell model calculations strongly support this perspective, but recent ab-initio calculations are at odds, ascribing all modes above 70 meV to the superconducting planes. In any case, the number and position of modes both in the visible and UV does not match any selection of non-Raman active or normally weak Γ -point modes, so they must either stem from other parts of the Brillouin zone, or they are strongly renormalized. For a definite progress on the mode assignment, we suggest 4 eV resonant scattering in $\text{YBa}_2\text{Cu}_3\text{O}_6$, where oxygen-chain modes do not exist by definition, and/or resonant scattering on site-selectively substituted isotopes compounds.

In conclusion, our investigations of the reflectance anisotropy, the newly discovered UV resonance, and the combination of Raman and electrical transport enable both a broader and a much more detailed perspective on persistent photo-induced effects. We find oxygen vacancy reordering in good agreement with all effects observed in Raman scattering and in reflectance anisotropy spectroscopy. The model consistently explains the time-constant difference between Raman response and electrical conductivity, if both are related to different aspects of reordering in terms of fragment length. The same effect is difficult to explain in a purely electronic model. The fast change of Raman intensity is similar to the properties of the mobility, indicating that both are connected to the comparatively mobile short fragments. Together with the fact that the photoexcited state deviates from room temperature equilibrium, the results point to an over-proportional reduction of short fragments by photoexcitation compared to thermal equilibrium. The absence of change in X-ray diffraction superstructure peaks puts a constraint on the maximum structural change achieved, or on its range. A purely electronic model does not account for the Raman and transport results, although no decisive evidence is found in our data which excludes an additional contribution to the effect.

Sample preparation

The samples of $RBa_2Cu_3O_{7-\delta}$ used in the Raman, RAS, Raman-and transport, and X-ray experiments were grown, detwinned and deoxygenated by our collaboration partners Prof. Dr. G. Nieva, Prof. Dr. J. Guimpel and Dr. B. Maiorov from Centro Atómico Bariloche, Argentina.

In the X-ray experiment, we also used untwinned and deoxygenated single crystals of $YBa_2Cu_3O_{7-\delta}$ (termed YBCO3 and YBCO4) provided by Dr. V. Hinkov, Max-Planck Institut für Festkörperforschung, Stuttgart, Germany. They have $T_c \approx 60$ K. For the details on their preparation and detwinning, see Ref. [127] and references therein.

Single crystals

The single crystals of $YBa_2Cu_3O_{6.7}$ and $YBa_2Cu_3O_{6.65}$ used in the Raman, RAS and the X-ray experiments were prepared using the flux-growth technique with yttria stabilized ZrO_2 trays. Details of method and proportions can be found in Ref. [128]. The same procedure was used to grow the $PrBa_2Cu_3O_{7-\delta}$ sample, with special care to choose single crystals with no Y contamination from the trays.

The oxygen content reduction for the Y and Pr samples were performed at 507°C in an oxygen atmosphere of 14.5 mbar followed by a controlled cooling down process. [129]

The chosen crystals were approximately $1.0 \times 0.5 \times 0.1 \text{ mm}^3$ ($a \times b \times c$) in size. In the case of Y, there were detwinned under uniaxial stress. X-ray diffraction showed excellent crystal quality and detwinning.

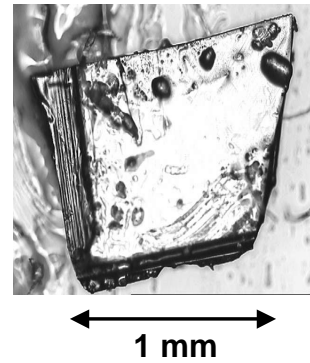


Figure A.1: Topview of an $YBa_2Cu_3O_{7-\delta}$ single crystal.

Polycrystalline samples

The samples of ceramic $RBa_2Cu_3O_{7-x}$ were prepared by a solid state reaction of stoichiometrically mixed powders, as described in Ref. [130]. The final sintering temperatures varied from 950°C to 970°C in flowing oxygen for all R with the exception of $R=\text{La}$, which was sintered at 970°C

in N₂, followed by annealing in oxygen. The oxygen content reduction was performed at 507°C in an oxygen atmosphere of 14.5 mbar followed by a controlled cooling down process which corresponds to $x = 0.3$ for $R=Y$. [129] The same procedure was followed for all ceramics of the R123 series, since the O₂ pressure-temperature diagrams are very similar for $R=Gd$ and $R=Y, Pr, Nd, La$ [131] except for La near maximum oxygen stoichiometry. Nevertheless, for our La sample we have measured a T_c value of 94(1) K and 10(3) K before and after oxygen reduction, respectively. The latter is in good agreement with literature data for an oxygen deficiency of $x = 0.3$. [132]

Thin films

The film of GdBa₂Cu₃O_{6.5} used in the Raman-and-transport setup was approximately 1500 Å thick. It was patterned lithographically to provide a narrow bridge of sample material (250 μm), as well as contacts for a four point probe (see Fig. 6.1 in Chap. 6). The sample was oxygen-reduced using the corresponding temperature and oxygen pressure values for bulk samples. From the curve of resistivity versus temperature we conclude that the film is superconducting with an onset temperature of 30 K. By comparison to the critical temperatures of a set of other GdBa₂Cu₃O_{7-δ} films we determine the oxygen concentration to be 6.5 ± 0.1 , close to the superconducting/insulating transition and in the ortho-II region of the phase diagram. [54]

The set of thin films of GdBa₂Cu₃O_{7-δ} with different oxygen contents studied with Raman spectroscopy had MgO-substrates. They were *c*-axis oriented and partially epitaxial in the *ab*-plane.

Bibliography

- [1] J. G. Bednorz and K. A. Müller. *Possible high $-T_c$ superconductivity in the Ba-La-Cu-O system*. Z. f. Phys. B, **64**, 189 (1986)
- [2] M. K. Wu, J. R. Ashburn, C. J. Torng, P. H. Hor, R. L. Meng, L. Gao, Z. J. Huang, Y. Q. Wang, and C. W. Chu. *Superconductivity at 93 K in a new mixed-phase Yb-Ba-Cu-O compound system at ambient pressure*. Phys. Rev. Lett., **58**, 908 (1987)
- [3] A. Schilling, M. Cantoni, J. D. Gou, and H. R. Ott. *Superconductivity above 130 K in the Hg-Ba-Ca-Cu-O system*. Nature, **363**, 56 (1993)
- [4] P. Dai, B. C. Chakaumakos, G. F. Sun, K. W. Wong, Y. Xin, and D. F. Lu. *Synthesis and neutron powder diffraction study of the superconductor $HgBa_2Ca_2Cu_3O_{8+\delta}$ by Tl substitution*. Physica C, **243**, 201 (1995)
- [5] J. D. Jorgensen, S. Pei, P. Lightfoot, H. Shi, A. P. Paulikas, and B. W. Veal. *Time-dependent structural phenomena at room temperature in quenched $YBa_2Cu_3O_{6.41}$ - Local oxygen ordering and superconductivity*. Physica C, **167**, 571 (1990)
- [6] A. I. Kirilyuk, N. M. Kreines, and V. I. Kudinov. *Frozen photoconductivity in $YBa_2Cu_3O_{7-x}$ films*. JETP Lett., **52**, 49 (1990)
- [7] G. Nieva, E. Osquiguil, J. Guimpel, M. Maenhoudt, B. Wuyts, Y. Bruynseraede, M. B. Maple, and I. K. Schuller. *Photoinduced enhancement of superconductivity*. App. Phys. Lett., **60**, 2159 (1992)
- [8] J. F. Federici, D. Chew, B. Welker, W. Savin, J. Gutierrez-Solana, T. Fink, and W. Wilber. *Defect mechanism of photoinduced superconductivity in $YBa_2Cu_3O_{6+x}$* . Phys. Rev. B, **52**, 15 592 (1995)
- [9] E. Osquiguil, M. Maenhoudt, B. Wuyts, Y. Bruynseraede, D. Lederman, and I. K. Schuller. *Photoexcitation and oxygen ordering in $YBa_2Cu_3O_x$ films*. Phys. Rev. B, **49**, 3675 (1994)
- [10] C. Stockinger, W. Markowitsch, W. Lang, W. Kula, and R. Sobolewski. *Mechanisms of photodoping in oxygen-deficient $YBa_2Cu_3O_{7-x}$ films studied by in situ transport measurements*. Phys. Rev. B, **57**, 8702 (1998)
- [11] D. R. Wake, F. Slakey, M. V. Klein, J. P. Rice, and D. M. Ginsberg. *Optically induced metastability in untwinned single-domain $YBa_2Cu_3O_7$* . Phys. Rev. Lett., **67**, 3728 (1991)
- [12] J. Orenstein and A. J. Millis. *Advances in the Physics of High-Temperature Superconductivity*. Science, **288**, 468 (2000)

- [13] W. Buckel and R. Kleiner. *Supraleitung - Grundlagen und Anwendungen*. Wiley VCH, 6 edn. (2004)
- [14] I. K. Schuller *et al.* *A snapshot view of High Temperature Superconductivity 2002* (2002)
- [15] K. Conder. *Oxygen diffusion in the superconductors of the YBaCuO family: isotope exchange measurements and models*. *Mat. Sci. and Eng.*, **R32**, 41–102 (2001)
- [16] M. Guillaume, P. Allenspach, W. Henggeler, J. Mesot, B. Roessli, U. Staub, P. Fischer, A. Furrer, and V. Trounov. *A systematic low-temperature neutron diffraction study of the $R\text{Ba}_2\text{Cu}_3\text{O}_x$ ($R=\text{Yttrium and rare earths}; x=6 \text{ and } 7$) compounds*. *J. Phys.: Condens. Matter*, **6**, 7963 (1994)
- [17] M. von Zimmermann, J. R. Schneider, T. Frello, N. H. Andersen, J. Madsen, M. Käll, H. F. Poulsen, R. Liang, P. Dosanjh, and W. N. Hardy. *Oxygen ordering superstructures in underdoped YBCO studied by hard X-ray diffraction*. *Phys. Rev. B*, **68**, 104 515 (2003)
- [18] R. Beyers, B. T. Ahn, G. Gorman, V. Y. Lee, S. S. P. Parkin, M. L. Ramirez, K. P. Roche, J. E. Vazquez, T. M. Gür, and R. A. Huggins. *Oxygen ordering, phase separation and the 60-K and 90 K plateaus in $\text{YBa}_2\text{Cu}_3\text{O}_{7-x}$* . *Nature*, **340**, 619 (1989)
- [19] D. de Fontaine, G. Ceder, and M. Asta. *Oxygen ordering in $\text{YBa}_2\text{Cu}_3\text{O}_{7-x}$* . *Nature*, **343**, 544 (1990)
- [20] P. Sterne and L. T. Wille. *Phase diagram and critical properties of oxygen ordering in $\text{YBa}_2\text{Cu}_3\text{O}_z$* . *Physica C*, **162**, 223 (1989)
- [21] G. Ceder, M. Asta, W. C. Carter, M. Kraitchman, D. de Fontaine, M. E. Mann, and M. Sluiter. *Phase diagram and low-temperature behaviour of oxygen ordering in $\text{YBa}_2\text{Cu}_3\text{O}_z$ using *ab initio* interactions*. *Phys. Rev. B*, **41**, 8698 (1990)
- [22] N. H. Andersen, B. Lebech, and H. F. Poulsen. *Structural phase diagram and equilibrium oxygen partial pressure of $\text{YBa}_2\text{Cu}_3\text{O}_6$* . *J. Less-Common Met.*, **164**, 124 (1990)
- [23] D. de Fontaine, V. Ozolins, Z. Islam, and S. C. Moss. *Origin of modulated structures in $\text{YBa}_2\text{Cu}_3\text{O}_{6.63}$: A first-principles approach*. *Phys. Rev. B*, **71**, 212 504 (2005)
- [24] N. H. Andersen, M. von Zimmermann, T. Frello, M. Käll, D. Mønster, P. A. Lindgård, J. Madsen, T. Niemöller, H. F. Poulsen, O. Schmidt, J. R. Schneider, T. Wolf, P. Dosanjh, R. Liang, and W. N. Hardy. *Superstructure formation and the structural phase diagram of $\text{YBa}_2\text{Cu}_3\text{O}_{6+x}$* . *Physica C*, **317-318**, 259 (1999)
- [25] J. Stremper, I. Zegkinoglou, U. Ruett, M. von Zimmermann, C. Bernhard, C. T. Lin, T. Wolf, and B. Keimer. *Oxygen superstructures throughout the phase diagram of $(\text{Y,Ca})\text{Ba}_2\text{Cu}_3\text{O}_{6+x}$* . *Phys. Rev. Lett.*, **93**, 157 007 (2004)

- [26] V. Plakhty, P. Burlet, and J. Y. Henry. *Atomic displacements in the ortho-II and ortho-III phases of $YBa_2Cu_3O_{6+x}$ as determined by X-ray and neutron scattering*. Phys. Lett. A, **198**, 256 (1995)
- [27] Z. Islam, S. K. Sinha, D. Haskel, J. C. Lang, G. Srajer, B. W. Veal, D. R. Haeffner, and H. A. Mook. *X-ray diffraction study of lattice modulations in an underdoped $YBa_2Cu_3O_{6+x}$ superconductor*. Phys. Rev. B, **66**, 092 501 (2002)
- [28] D. Mønster, P.-A. Lindgård, and N. H. Andersen. *Simple solution to problems concerning oxygen ordering in $YBa_2Cu_3O_{6+x}$* . Phys. Rev. B, **60**, 110 (1999)
- [29] D. Mønster, P. A. Lindgård, and N. H. Andersen. *Oxygen ordering in $YBa_2Cu_3O_{7-x}$ using Monte Carlo simulation and analytic theory*. Phys. Rev. B, **64**, 224 520–1 (2001)
- [30] P. Manca and S. Sanna. *Orthorhombic low-temperature superstructures in $YBa_2Cu_3O_{7-x}$* . Phys. Rev. B, **63**, 134 512–1 (2001)
- [31] P. Schleger, H. Casalta, R. Hadfield, H. F. Poulsen, M. von Zimmermann, N. H. Andersen, J. R. Schneider, R. Liang, P. Dosanjh, and W. N. Hardy. *Observation of Ortho-III correlations by neutron and hard x-ray scattering in an untwinned $YBa_2Cu_3O_{6.77}$ single crystal*. Physica C, **241**, 103 (1995)
- [32] P. Schleger, R. A. Hadfield, H. Casalta, N. H. Andersen, H. F. Poulsen, M. von Zimmermann, J. R. Schneider, R. Liang, P. Dosanjh, and W. N. Hardy. *Random-Field Structural Transition in $YBa_2Cu_3O_{6.5}$?* Phys. Rev. Lett., **74**, 1446 (1995)
- [33] R. J. Cava, A. W. Hewat, E. S. Hewat, B. Batlogg, M. Marezio, K. M. Rabe, J. J. Krajewski, W. F. Peck, and L. W. Rupp. *Structural anomalies, oxygen ordering and superconductivity in oxygen deficient $YBa_2Cu_3O_{7-x}$* . Physica C, **165**, 419 (1990)
- [34] H. F. Poulsen, N. H. Andersen, J. V. Andersen, H. Bohr, and O. G. Mouritsen. *Relation between superconducting transition temperature and oxygen ordering in YBCO*. Nature, **349**, 594 (1991)
- [35] G. Ceder, M. Asta, and D. de Fontaine. *Computation of the OI-OII-OIII phase diagram and local oxygen configurations for $YBa_2Cu_3O_z$ with z between 6.5 and 7*. Physica C, **177**, 106 (1991)
- [36] P. J. Kundrotas, E. E. Tornau, and A. Rosengren. *Dynamics of oxygen ordering in the cell-doubled phase of $YBa_2Cu_3O_{6+x}$* . Phys. Rev. B, **54**, 4357 (1996)
- [37] A. A. Maksimov, D. A. Pronin, S. V. Zaitsev, I. I. Tartakovskii, G. Blumberg, M. V. Klein, M. Karlow, S. L. Cooper, A. P. Paulikas, and B. W. Veal. *Influence of oxygen-ordering kinetics on Raman and optical response in $YBa_2Cu_3O_{6.4}$* . Phys. Rev. B, **54**, R6901 (1996)

- [38] P. Nagel, V. Pasler, C. Meingast, A. I. Rykov, and S. Tajima. *Anomalously large oxygen-ordering contribution to the thermal expansion of untwinned $YBa_2Cu_3O_{6.95}$ single crystals: a glasslike transition near room temperature.* Phys. Rev. Lett., **85**, 2376 (2000)
- [39] A. Latgé, E. V. Anda, and J. L. Morán-López. *Oxygen-disorder and correlation effects on the hole concentration and metal-nonmetal transition in $YBa_2Cu_3O_{7-x}$.* Phys. Rev. B, **42**, 4288 (1990)
- [40] A. A. Aligia and J. Garcés. *Charge transfer and oxygen ordering in $YBa_2Cu_3O_{6+x}$.* Phys. Rev. B, **49**, 524 (1994)
- [41] G. Uimin. *Order and disorder in the ensemble of Cu-O chain fragments in oxygen-deficient planes of $YBa_2Cu_3O_{6+x}$.* Phys. Rev. B, **50**, 9531 (1994)
- [42] P. Manca, S. Sanna, G. Calestani, A. Migliori, R. D. Renzi, and G. Allodi. *Critical chain length and superconductivity in oxygen-equalized pairs of $YBa_2Cu_3O_{6.30}$.* Phys. Rev. B, **61**, 15 450 (2000)
- [43] Y. S. Lee, K. Segawa, Y. Ando, and D. N. Basov. *Coherence and Superconductivity in Coupled One-Dimensional Chains: A Case Study of $YBa_2Cu_3O_y$.* Phys. Rev Lett., **94**, 137 004 (2005)
- [44] G. Nieva, E. Osquiguil, J. Guimpel, M. Maenhoudt, B. Wuyts, Y. Bruynseraede, M. B. Maple, and I. K. Schuller. *Photoinduced changes in the transport properties of oxygen-deficient $YBa_2Cu_3O_x$.* Phys. Rev. B, **46**, 14 249 (1992)
- [45] B. W. Veal, A. P. Paulikas, H. You, H. Shi, Y. Fang, and J. W. Downey. *Observation of temperature-dependent site disorder in $YBa_2Cu_3O_{7-\delta}$ below 150 C.* Phys. Rev. B, **42**, 6305 (1990)
- [46] J. Guimpel, B. Maiorov, E. Osquiguil, G. Nieva, and F. Pardo. *Interrelation between persistent photoconductivity and oxygen order in $GdBa_2Cu_3O_{7-x}$ thin films.* Phys. Rev. B, **56**, 3552 (1997)
- [47] V. I. Kudinov, A. I. Kirilyuk, N. M. Kreines, R. Laiho, and E. Läderanta. *Photoinduced superconductivity in $YBa_2Cu_3O_{7-x}$ films.* Phys. Lett. A, **151**, 358 (1990)
- [48] W. Markowitsch, A. Altenburger, W. Lang, M. Peruzzi, J. D. Pedarnig, and D. Bäuerle. *Persistent photoconductivity in $YBa_2Cu_3O_x$ by visible and UV excitation below T_c .* Physica C, **405**, 173 (2004)
- [49] V. I. Kudinov, I. L. Chaplygin, A. I. Kirilyuk, N. M. Kreines, R. Laiho, E. Läderanta, and C. Ayache. *Persistent photoconductivity in $YBa_2Cu_3O_{7-x}$ films as a method of photodoping towards metallic and superconducting phases.* Phys. Rev. B, **47**, 9017 (1993)

- [50] W. Markowitsch, C. Stockinger, W. Göb, W. Lang, W. Kula, and R. Sobolewski. *Dynamics of photodoping and photoconductivity relaxation in oxygen-deficient $YBa_2Cu_3O_{7-x}$* . Physica C, **265**, 187 (1996)
- [51] J. Hasen, D. Lederman, I. K. Schuller, V. Kudinov, M. Maenhoudt, and Y. Bruynseraede. *Enhancement of persistent photoconductivity in insulating high- T_c thin films*. Phys. Rev. B, **51**, 1342 (1995)
- [52] K. Kawamoto and I. Hirabayashi. *Reversible photostructural change in oxygen-deficient $YBa_2Cu_3O_{7-x}$* . Phys. Rev. B, **49**, 3655 (1994)
- [53] D. Lederman, J. Hasen, I. K. Schuller, E. Osquiguil, and Y. Bruynseraede. *Photoinduced superconductivity and structural changes in high temperature superconducting films*. Appl. Phys. Lett., **64**, 652 (1994)
- [54] B. Maiorov. *Efectos de fotoexcitación en películas delgadas de $GdBa_2Cu_3O_x$* . Master's thesis, Instituto Balseiro, Comisión Nacional de Energía Atómica, 8400 San Carlos de Bariloche, Río Negro, Argentina (1997)
- [55] T. Endo, A. Hoffmann, J. Santamaria, and I. K. Schuller. *Enhancement of persistent photoconductivity by UV excitation in $GdBa_2Cu_3O_{6.3}$* . Phys. Rev. B, **54**, R3750 (1996)
- [56] C. Ayache, I. L. Chaplygin, A. I. Kirilyuk, N. M. Kreines, and V. I. Kudinov. *Spectrum of persistent photoconductivity in $YBa_2Cu_3O_{7-x}$ films*. Solid State Commun., **81**, 41 (1992)
- [57] D. M. Bubb, J. F. Federici, S. C. Tidrow, W. Wilber, J. Kim, and A. Piqué. *Wavelength and photon dose dependence of infrared quenched persistent photoconductivity in $YBa_2Cu_3O_{6-x}$* . Phys. Rev. B, **60**, 6827 (1999)
- [58] A. G. Panfilov, M. F. Limonov, A. I. Rykov, S. Tajima, and A. Yamanaka. *Superconductivity-induced effect on "Raman-forbidden" modes in underdoped $YBa_2Cu_3O_{7-x}$ single crystals*. Phys. Rev. B, **57**, R5634 (1998)
- [59] A. G. Panfilov, A. I. Rykov, S. Tajima, and A. Yamanaka. *Photoinduced oxygen reordering in $YBa_2Cu_3O_{7-x}$ single crystals*. Phys. Rev. B, **58**, 12 459 (1998)
- [60] A. Fainstein, P. Etchegoin, and J. Guimpel. *Raman study of photoinduced chain-fragment ordering in $GdBa_2Cu_3O_x$ thin films*. Phys. Rev. B, **58**, 9433 (1998)
- [61] M. Käll, M. Osada, M. Kakihana, L. Börjesson, T. Frello, J. Madsen, N. H. Andersen, R. Liang, P. Dosanjh, and W. N. Hardy. *CuO-chain Raman scattering and photoinduced metastability in $YBa_2Cu_3O_x$* . Phys. Rev. B, **57**, R14 072 (1998)

- [62] R. Liu, C. Thomsen, W. Kress, M. Cardona, B. Gegenheimer, F. W. de Wette, J. Prade, A. D. Kulkarni, and U. Schröder. *Frequencies, eigenvectors, and single-crystal selection rules of $K=0$ phonons in $YBa_2Cu_3O_8$ - theory and experiment*. Phys. Rev. B, **37**, R7971 (1988)
- [63] A. Fainstein, B. Maiorov, J. Guimpel, G. Nieva, and E. Osquiguil. *Annealing disorder and photoinduced order of oxygen chains in detwinned $YBa_2Cu_3O_{6.65}$ single crystals probed by Raman scattering*. Phys. Rev. B, **61**, 4298 (2000)
- [64] M. Käll, M. Osada, J. Bäckström, M. Kakihana, L. Börjesson, T. Frello, J. Madsen, N. H. Andersen, R. Liang, P. Dosanjh, and W. N. Hardy. *Resonance Raman scattering as a probe of oxygen dynamics in YBCO*. J. Phys. Chem. Solids, **59**, 1988 (1998)
- [65] W. Kress, U. Schröder, J. Prade, A. D. Kulkarni, and F. W. de Wette. *Lattice dynamics of the high- T_c superconductor $YBa_2Cu_3O_{7-x}$* . Phys. Rev. B, **38**, R2906 (1988)
- [66] V. G. Ivanov, M. N. Iliev, and C. Thomsen. *Micro-Raman study of isotope substitution in $YBa_2Cu_3^{18}O_{6.2}$ during local laser annealing*. Phys. Rev. B, **52**, 13 652 (1995)
- [67] K. P. Bohnen, R. Heid, and M. Krauss. *Phonon dispersion and electron-phonon interaction for $YBa_2Cu_3O_7$ from first-principles calculations*. Euro. Phys. Lett., **64**, 104 (2003)
- [68] D. N. Basov and T. Timusk. *Electrodynamics of high- T_c superconductors*. Rev. Mod. Phys., **77**, 721 (2005)
- [69] J. Kircher, M. K. Kelly, S. Rashkeev, M. Alouani, D. Fuchs, and M. Cardona. *Anisotropy and oxygen-stoichiometry dependence of the dielectric tensor of $YBa_2Cu_3O_{7-\delta}$ ($0 \leq \delta \leq 1$)*. Phys. Rev. B, **44**, 217 (1991)
- [70] M. K. Kelly, P. Barboux, J. M. Tarascon, D. E. Aspnes, W. A. Bonner, and P. A. Morris. *Oxygen-deficiency-induced localized optical excitations in $YBa_2Cu_3O_x$* . Phys. Rev. B, **38**, R870 (1988)
- [71] J. Kircher, M. Cardona, A. Zibold, K. Widder, and H. P. Geserich. *Optical investigation of room-temperature chain ordering in $YBa_2Cu_3O_{7-\delta}$* . Phys. Rev. B, **48**, 9684 (1993)
- [72] S. L. Cooper, A. L. Kotz, M. A. Karlow, M. V. Klein, W. C. Lee, J. Giapintzakis, and D. M. Ginsberg. *Development of the optical conductivity with doping in single-domain $YBa_2Cu_3O_{6+x}$* . Phys. Rev. B, **45**, 2549 (1992)
- [73] M. E. Bijlsma, H. Wormeester, D. H. A. Blank, E. Span, A. van Silfhout, and H. Rogalla. *Temperature dependence of the 4-eV optical transition in $YBa_2Cu_3O_6$* . Phys. Rev. B, **57**, 13 418 (1998)

- [74] A. V. Boris, N. N. Kovaleva, O. V. Dolgov, T. Holden, C. T. Lin, B. Keimer, and C. Bernhard. *In-Plane Spectral Weight Shift of Charge Carriers in $YBa_2Cu_3O_{6.9}$* . *Science*, **304**, 708 (2004)
- [75] J. Bäckström, D. Budelmann, R. Rauer, M. Rübhausen, H. Rodriguez, and H. Adrian. *Optical properties of $YBa_2Cu_3O_{7-\delta}$ and $PrBa_2Cu_3O_{7-\delta}$ films: High-energy correlations and metallicity*. *Phys. Rev. B*, **70**, 174 502 (2004)
- [76] T. Timusk and B. Statt. *The pseudogap in high-temperature superconductors: an experimental survey*. *Rep. Prog. Phys.*, **62**, 61 (1999)
- [77] A. L. Kotz, M. V. Klein, W. C. Lee, J. Giapintzakis, D. M. Ginsberg, and B. W. Veal. *Anisotropy of the optical dielectric function in the ab plane for $YBa_2Cu_3O_{7-\delta}$* . *Phys. Rev. B*, **45**, R2577 (1992)
- [78] K. Widder, A. Zibold, M. Merz, H. P. Geserich, A. Erb, and G. Mullervogt. *Ordering of chain oxygen in $YBa_2Cu_3O_x$ - optical investigations on single-domain crystals*. *Physica C*, **232**, 82 (1994)
- [79] J. Kircher, M. Alouani, M. Garriga, P. Murugaraj, J. Maier, C. Thomsen, M. Cardona, O. K. Anderson, and O. Jepsen. *Anisotropy of the dielectric function in $YBa_2Cu_3O_6$* . *Phys. Rev. B*, **40**, 7368 (1989)
- [80] D. E. Aspnes, J. P. Harbison, A. A. Studna, and L. T. Florez. *Oscillations in the optical response of (001)GaAs and AlGaAs surfaces during crystal growth by molecular beam epitaxy*. *Appl. Phys. Lett.*, **52**, 957 (1988)
- [81] D. E. Aspnes, J. P. Harbison, A. A. Studna, and L. T. Florez. *Application of reflectance difference spectroscopy to molecular-beam epitaxy growth of GaAs and AlAs*. *J. Vac. Sci. A*, **6** (3), 1327 (1988)
- [82] G. Bauer and W. Richter. *Optical Characterization of Epitaxial Semiconductor Layers*. Springer (1996)
- [83] A. Bruchhausen, S. Bahrs, K. Fleischer, A. R. Goñi, A. Fainstein, G. Nieva, A. A. Ali-gia, W. Richter, and C. Thomsen. *Photoinduced chain-oxygen ordering in detwinned $YBa_2Cu_3O_{6.7}$ single crystals*. *Phys. Rev. B*, **69**, 224 508 (2004)
- [84] S. Bahrs, A. Bruchhausen, A. R. Goñi, G. Nieva, A. Fainstein, K. Fleischer, W. Richter, and C. Thomsen. *Effect of light on the reflectance anisotropy and chain-oxygen related Raman signal in untwinned, underdoped crystals of $YBa_2Cu_3O_7$* . to be published in *J. Phys. Chem. Sol.* (2005)
- [85] C. V. Raman. *A change of wavelength in light scattering*. *Nature*, **121**, 619 (1928)

- [86] M. Cardona. *Resonance Phenomena*. In M. Cardona and G. Güntherodt (Eds.), *Light Scattering in Solids II*, vol. 50 of *Topics in Applied Physics*, chap. 2, 19. Springer, Berlin (1989)
- [87] P. Y. Yu and M. Cardona. *Fundamentals of Semiconductors*. Springer, 2 edn. (1999)
- [88] R. M. Martin and L. M. Falikov. *Resonant Raman scattering*. In M. Cardona and G. Güntherodt (Eds.), *Light scattering in Solids I*, vol. 8 of *Topics in Applied physics*, chap. 3, 79. Springer, Berlin (1983)
- [89] C. Thomsen. *Light Scattering in high- T_c Superconductors*. In M. Cardona and G. Güntherodt (Eds.), *Light Scattering in Solids VI*, vol. 68 of *Topics in Applied Physics*, 285. Springer, Berlin (1991)
- [90] J. Humlíček, A. P. Litvinchuk, W. Kress, B. Lederle, C. Thomsen, M. Cardona, H. U. Habermeier, I. E. Trofimov, and W. König. *Lattice vibrations of $Y_{1-x}Pr_xBa_2Cu_3O_7$: theory and experiment*. *Physica C*, **206**, 345 (1993)
- [91] A. P. Litvinchuk, C. Thomsen, and M. Cardona. *Infrared-active vibrations of high-temperature superconductors: Experiment and theory*. In D. M. Ginsberg (Ed.), *Physical properties of high-temperature superconductors IV*, chap. 6, 402. World Scientific (1994)
- [92] K. F. McCarty, J. Z. Liu, R. N. Shelton, and H. B. Radousky. *Raman-active phonons of a twin-free $YBa_2Cu_3O_7$ crystal: A complete polarization analysis*. *Phys. Rev. B*, **41**, 8792 (1990)
- [93] E. T. Heyen, J. Kircher, and M. Cardona. *Resonant Raman scattering in insulating $YBa_2Cu_3O_6$ as a probe of its electronic structure*. *Phys. Rev. B*, **45**, 3037 (1992)
- [94] E. T. Heyen, R. Liu, C. Thomsen, R. Kremer, M. Cardona, J. Karpinski, E. Kaldis, and S. Rusiecki. *Optical phonons in $YBa_2Cu_4O_8$ and $Y_2Ba_4Cu_7O_{15-\delta}$* . *Phys. Rev. B*, **41**, 11 058 (1990)
- [95] V. Pankoke, K. P. Bohnen, and R. Heid. *Lattice dynamics and electron-phonon coupling in $YBa_2Cu_4O_8$ compared with $YBa_2Cu_3O_7$* (2005). Poster presented on DPG spring meeting
- [96] M. Cardona, R. Liu, C. Thomsen, M. Bauer, L. Genzel, W. König, A. Wittlin, U. Amador, M. Barahona, F. Fernandez, C. Otero, and R. Saez. *Infrared and Raman spectra of the new superconducting cuprate perovskites $MBa_2Cu_3O_7$* . *Solid State Commun.*, **65**, 71 (1988)
- [97] S. Bahrs, A. R. Goñi, C. Thomsen, B. Maiorov, G. Nieva, and A. Fainstein. *Rare-earth dependence of photoinduced chain-oxygen ordering in $RBa_2Cu_3O_{7-x}$ ($x \approx 0.3$) investigated by Raman scattering*. *Phys. Rev. B*, **65**, 024 522 (2002)

- [98] C. Thomsen, R. Liu, M. Bauer, A. Wittlin, L. Genzel, M. Cardona, E. Schönherr, W. Bauhofer, and W. König. *Systematic Raman and Infrared Studies of the Superconductor $YBa_2Cu_3O_{7-x}$ as a Function of Oxygen Concentration ($0 < x < 1$)*. Solid State Comm., **65**, 55 (1988)
- [99] M. Cardona, R. Liu, C. Thomsen, W. Kress, E. Schönherr, M. Bauer, L. Genzel, and W. König. *Effect of isotopic substitution of oxygen on T_c and the phonon frequencies of high- T_c superconductors*. Solid State Commun., **67**, 789 (1988)
- [100] K. Conder, E. Kaldis, M. Maciejewski, K. A. Müller, and E. F. Steigemeier. *Oxygen isotope exchange kinetics and site-selective oxygen substitution in $YBa_2Cu_3O_{7-x}$* . Physica C, **210**, 282 (1993)
- [101] D. Palles, N. Poulakis, E. Liarokapis, K. Conder, E. Kaldis, and K. A. Müller. *Raman study of the oxygen anharmonicity in $YBa_2Cu_3O_x$ ($6.4 < x < 7.0$) superconductors*. Phys. Rev. B, **54**, 6721 (1996)
- [102] H. J. Rosen, R. M. Macfarlane, E. M. Engler, V. Y. Lee, and R. D. Jacowitz. *Systematic study of rare-earth substitution on the lattice modes of high- T_c superconductors*. Phys. Rev. B, **38**, 2460 (1988)
- [103] C. Thomsen and G. Kaczmarczyk. *Vibrational spectroscopy in high-temperature superconductors*. In J. M. Chalmer and P. R. Griffiths (Eds.), *Handbook of Vibrational Spectroscopy*. Wiley, Chichester (2002)
- [104] L. Pintschovius and W. Reichardt. *Inelastic neutron scattering studies of the lattice vibrations of high- T_c compounds*. In D. E. Ginsberg (Ed.), *Physical properties of high-temperature superconductors IV*, chap. 5, 375. World Scientific (1994)
- [105] L. Pintschovius. *Electron-phonon coupling effects explored by inelastic neutron scattering*. phys. stat. sol. (b), **242**, 30 (2005)
- [106] L. Pintschovius, W. Reichardt, M. Klaser, T. Wolf, and H. v Lohneysen. *Pronounced in-plane anisotropy of phonon anomalies in $YBa_2Cu_3O_{6.6}$* . Phys. Rev. Lett., **89**, 037 001 (2002)
- [107] L. Pintschovius, D. Reznik, W. Reichardt, Y. Endoh, H. Hiraka, J. M. Tranquada, H. Uchiyama, T. Masui, and S. Tajima. *Oxygen phonon branches in $YBa_2Cu_3O_7$* . Phys. Rev. B, **69**, 214 506 (2004)
- [108] E. T. Heyen, S. N. Rashkeev, I. I. Mazin, O. K. Andersen, R. Liu, M. Cardona, and O. Jepsen. *Resonant Raman scattering in $YBa_2Cu_3O_7$: Band theory and experiment*. Phys. Rev. Lett., **65**, 3048 (1990)

- [109] C. Ambrosch-Draxl, H. Auer, R. Kouba, E. Y. Sherman, P. Knoll, and M. Mayer. *Raman scattering in $YBa_2Cu_3O_7$: A comprehensive theoretical study in comparison with experiments*. Phys. Rev. B, **65**, 064 501 (2002)
- [110] E. Kroumova, M. I. Aroyo, J. M. Perez Mato, A. Kirov, C. Capillas, S. Ivantchev, and H. Wondratschek. *Bilbao Crystallographic Server: useful databases and tools for phase transitions studies*, <http://www.cryst.ehu.es/>. Phase Transitions, **76 (1-2)**, 155–170 (2003)
- [111] B. Schulz, J. Bäckstrom, D. Budelmann, R. Maeser, M. Rübhausen, M. V. Klein, E. Schoeffel, A. Mihill, and S. Yoon. *Fully reflective deep ultraviolet to near infrared spectrometer and entrance optics for resonance Raman spectroscopy*. Rev. Sci. Inst., **76**, 073 107 (2005)
- [112] S. Bahrs, S. Reich, A. Zwick, A. R. Goñi, W. Bacsa, G. Nieva, and C. Thomsen. *Raman spectroscopy with UV excitation on untwinned single crystals of $YBa_2Cu_3O_{7-\delta}$* . phys. stat. sol. (b), **241**, R63 (2004)
- [113] S. Bahrs, S. Müller, M. Rübhausen, B. Schulz, A. R. Goñi, G. Nieva, and C. Thomsen. *Anisotropic UV-Raman resonance in underdoped $YBa_2Cu_3O_{6.7}$* . submitted to Phys. Rev. B (2005)
- [114] S. Müller *et al.* *Resonant Raman study of optimally and fully doped $YBa_2Cu_3O_x$* (2005). Private communication
- [115] C. Thomsen, A. P. Litvinchuk, E. Schönherr, and M. Cardona. *Chain-oxygen vibrations in $YBa_2Cu_3O_{7-\delta}$ and $YBa_2Cu_4O_8$* . Phys. Rev. B, **45**, 8154 (1992)
- [116] S. Bahrs, A. R. Goñi, B. Maiorov, G. N. Nieva, A. Fainstein, and C. Thomsen. *Raman-Study of Photoinduced Chain-Oxygen Ordering in $RBa_2Cu_3O_{(7-\delta)}$* . IEEE Trans. Appl. Supercond., **13**, 3192 (2003)
- [117] H. Scher, M. F. Shlesinger, and J. T. Bandler. *Time-scale invariance in transport and relaxation*. Physics Today, **44 (1)**, 26 (1991)
- [118] H. F. Poulsen, N. H. Andersen, J. V. Andersen, H. Bohr, and O. G. Mouritsen. *Dynamical Scaling of Oxygen Ordering in $YBa_2Cu_3O_{7-x}$* . Phys. Rev. Lett., **66**, 465 (1991)
- [119] M. Käll, M. von Zimmermann, N. H. Andersen, J. Madsen, T. Frello, H. F. Poulsen, J. R. Schneider, and T. Wolf. *Anisotropic dynamical scaling in a weakly 3D system: The case of oxygen ordering in YBCO*. Euro. Phys. Lett., **51**, 447 (2000)
- [120] J. F. Federici and D. M. Bubb. *The role of defects in persistens photoconductivity*. J. Supercond., **14**, 331 (2001)

- [121] C. Thomsen and S. Reich. *Double resonant Raman scattering in graphite*. Phys. Rev. Lett., **85**, 5214 (2000)
- [122] J. Maultzsch, S. Reich, and C. Thomsen. *Double-resonant Raman scattering in graphite: interference effects, selection rules and phonon dispersion*. Phys. Rev. B, **70**, 155 403 (2004)
- [123] W. Markowitsch, A. Altenburger, W. Lang, M. Peruzzi, J. D. Pedarnig, and D. Bäuerle. *Persistent photoconductivity in $YBa_2Cu_3O_x$ by visible and UV excitation below T_c* . Physica C, **405**, 173 (2004)
- [124] S. Bahrs, A. R. Goñi, C. Thomsen, B. Maiorov, G. Nieva, and A. Fainstein. *Light-induced oxygen-ordering dynamics in $(Y,Pr)Ba_2Cu_3O_{6,7}$: A Raman spectroscopy and Monte Carlo study*. Phys. Rev. B, **70**, 014 512 (2004)
- [125] J. D. Jorgensen, B. W. Veal, A. P. Paulikas, L. J. Novicki, G. W. Crabtree, H. Claus, and W. K. Kwok. *Structural properties of oxygen-deficient $YBa_2Cu_3O_{7-\delta}$* . Phys. Rev. B, **41**, 1863 (1990)
- [126] B. W. Veal, H. You, A. P. Paulikas, H. Shi, Y. Fang, and J. W. Downey. *Time-dependent superconducting behaviour of oxygen-deficient $YBa_2Cu_3O_{7-x}$: Possible annealing of oxygen vacancies at 300 K*. Phys. Rev. B, **42**, 4770 (1990)
- [127] V. Hinkov, S. Pailhes, P. Bourges, Y. Sidis, A. Ivanov, A. Kulakov, C. T. Lin, D. P. Chen, C. Bernhard, and B. Keimer. *Two-dimensional geometry of spin excitations in the high-transition-temperature superconductor $YBa_2Cu_3O_{6+x}$* . Nature, **430**, 650 (2004)
- [128] E. F. Righi, S. A. Grigera, G. Nieva, and F. de la Cruz. *Vortex phase coherence along the c axis in $YBa_2Cu_3O_{7-\delta}$* . Sup. Rev., **2**, 205 (1998)
- [129] E. Osquiguil, M. Maenhoudt, B. Wuyts, and Y. Bruynseraede. *Controlled preparation of oxygen deficient $YBa_2Cu_3O_{7-x}$ films*. Appl. Phys. Lett., **60**, 1627 (1992)
- [130] G. Nieva, S. Ghamaty, B. W. Lee, M. G. Maple, and I. K. Schuller. *Superconductivity and magnetism in $Eu_{1-x}Pr_xBa_2Cu_3O_{7-\delta}$* . Phys. Rev. B, **44**, 6999 (1991)
- [131] T. B. Lindemer and E. D. Specht. *Nonstoichiometry and decomposition of $Pr_{1+z}Ba_{2-z}Cu_3O_y$ and comparison with YBCO, LaBCO and NdBCO*. Physica C, **268**, 271 (1996)
- [132] T. B. Lindemer, B. C. Chakoumakos, E. D. Specht, R. K. Williams, and Y. J. Chen. *Effects of composition and processing on the superconductivity of $La_{1+z}Ba_{2-z}Cu_3O_y$* . Physica C, **231**, 80 (1994)

Acknowledgement

Over the last four years, many people have contributed to this work. It became possible with their ideas, guidance, help, and encouragement.

I would like to thank

Christian Thomsen, for giving me the opportunity to study the high- T_c superconductors, for his support for this work, his encouragement and the discussions on the topic. Many thanks for sharing the knowledge on Raman in the cuprates, and for teaching me the craft of publishing scientific work. I also particularly benefitted from the existing contacts to other groups, and the support of further collaborations, when a method available elsewhere seemed promising. The insight into a range of groups, methods and laboratories at TU Berlin and elsewhere is something I enjoyed very much.

Alejandro Goñi, for gaining my interest for the cuprates with his enthusiasm for physics, and for introducing me to the secrets of Raman laboratory work. Thanks for explaining any solid-state effect I wanted to learn about, and for the flow of ideas on interpretations and models, which has been a constant inspiration. Many thanks also for showing me round Argentina, journeying was great fun.

Andreas Knorr, for being the chairman in the defense of my thesis.

The optical and the low-temperature groups at Bariloche. Alex Fainstein's ideas were vital input for this work, and encouragement and constructive discussion always only an email away. Special thanks to Axel Bruchhausen for working with me in Berlin in Summer 2003, we made excellent progress on the RAS experiments. Thanks also for taking me to the first day of skiing in Bariloche in my life. Special thanks to Gladys Nieva, Julio Guimpel, Boris Maiorov and many others for their knowledge and ideas on the physics of the persistent effects, and for the help and hospitality I encountered during my visits to Bariloche.

Stephanie Reich, for the idea and the first attempt on Raman with ultraviolet excitation, and for all those short corridor breaks.

Wolfgang Bacsa, for his hospitality during my stay in Toulouse. I enjoyed it very much.

Karsten Fleischer, for introducing me to the secrets of the RAS setup, and for lending support any time.

Isabelle Joumard, Tien-Lin Lee and Jörg Zegenhagen, for their expertise on X-ray diffraction at the ID32 beamline in Grenoble, and for their hospitality during my stay. Thanks to Isabelle for

taking care of me when my suitcase had travelled the other way.

Michael Rübhausen, Sonja Müller, Ben Schulz and the Hamburg group for a very fruitful joint laboratory session.

Christian Kristukat for his expertise on SuSE Linux and computers in general, I have greatly benefitted from that. Special thanks for the invention of peak-o-mat, a very useful tool. And of course, for coaxing the group into everything from a cart via a choir concert to a sailing boat from time to time.

Janina Maultzsch, for explaining group theory and for letting me glimpse real chocolate expertise. Thanks for wondering and writing emails if I do not turn up at university without notice.

María Machón, for trying to teach me SIESTA, and, with a little more success, Spanish, and, with no success at all, a reasonable work-life balance.

Hagen Telg, for his unquenchable (kinetic) energy, and for getting entangled in a chair in the control room at ESRF in a way that left a local scientist deeply worried about user safety.

Bernd Schöler, Marianne Heinold, Heiner Perls, Sabine Morgner, and Michaela Sofsky for all their help and support, be it an item on my laboratory shopping list, a broken optical window, a strange encounter with bureaucracy, or just a little more Helium I urgently need till tomorrow morning. Special thanks to Bernd Schöler for his construction of the laser holder for Grenoble.

Harald Scheel, for lending his incredible skill with laboratory work. Paula Giudici, for introducing me to the world of Hubbard. Peter Rafailov, for awarding me my first coauthorship, and for being a reassuring presence at any time of the day. Uwe Kuhlmann, for spirited discussions on molecular vibrations in organic compounds and other things. Marcel Mohr, for a crash course on correlation table interpretation, and for his ability to hover on a whisp of coffee smell. Carola Nisse, for taking interest in the field of superconductivity. Djula Garasevic, for her little treats, which have raised the standard of the store considerably. And to all members of the group at TU Berlin, who will hopefully top the local table-tennis world-rang list for years to come.

Matthias, for everything, and for taking me into writing-custody in the final stages of the making of this thesis.

My family, for “Ach Kind, Du musst doch selber wissen, was Du tust!”. (Well, see for yourself.)

I also acknowledge the “Berliner Programm für Chancengleichheit von Frauen in Forschung und Lehre”, which has provided financial support during two years.